A new scanning optical dipole trap and towards optical potentials for erbium using q-plates

– MASTER THESIS –

by

Sarah Embacher, BSc

submitted to the Faculty of Mathematics, Computer Science, and Physics of the University of Innsbruck

in partial fulfillment of the requirements for the degree of Master of science (MSc)

advisor:

Univ.-Prof. Dr. Francesca Ferlaino,
Institute for Experimental Physics, University of Innsbruck

Innsbruck, November 2024

Abstract

This thesis studies optical setups to shape laser light in order to optically trap ultracold atoms. In particular, we will report on two different techniques. The first one is based on the periodic displacement of a laser beam in order to create a time-averaged potentials, whereas the second focuses on the spatial modulation of the polarization of the light.
For the time-averaged potential, we develop a new scanning optical dipole trap to replace the old one which has been implemented in the early stages of the ERBIUM experiment [Bai12]. The scanning optical dipole trap realizes a tunable aspect ratio which improves the loading efficiency from the magneto-optical trap and allows to control the trap geometry, which is crucial for observing many-body effects such as supersolidity in a dipolar quantum gas. The tunable aspect ratio is achieved by periodically displacing the 1st diffraction order of an acousto-optical modulator. Because the scanning of the beam happens at a frequency much faster than the frequency of the harmonic trap, the atoms experience a time-averaged potential shaped by the elliptical beam profile. The optical setup is first tested offline, where we find that the waist in the scanning direction can be tuned from 22.38(2) μm to 169.3(2) μm. The setup was then implemented into the experiment. Relying on the excitation of the dipole mode, we measure a trap frequency of $2\pi \times 203.3(6)$ Hz without scanning and $2\pi \times 64(3)$ Hz at the maximum scanning amplitude.
The second part of this thesis investigates the possibility of using q-plates to generate optical trapping potentials for ultracold erbium. Q-plates are optical elements that contain a liquid crystal layer where a specific pattern is imprinted to generate a helical phase front as light passes through. This creates an optical vortex, meaning that the intensity is zero in the beam's center. In addition, the polarization profile of the beam varies around the radial direction. The idea is now to use such a spatially non-uniform polarization for erbium, which has a polarization-dependent atom-light interaction. As a lanthiande atom, it features both a strong vectorial and tensorial part of the polarizability in addition to the isotropic scalar part. To enter regimes where the vectorial and tensorial parts become comparable the isotropic part, we aim to use light which is detuned by a few GHz from the narrow 841 nm transition. Indeed, we calculate that q-plate beams can generate a ring lattice potential for erbium atoms. We identify and discuss several challenges for the experimental implementation, for example regarding the heating due to photon scattering or aberrations and imperfections in the optical system that could introduce unwanted effects on the trapping potential.

Contents

Chapter 1

Introduction

After James Clerk Maxwell combined electric and magnetic fields in his equations in 1865 [Max65], it seemed that the basic laws of nature were fully understood through the classical theories of mechanics, electromagnetism and thermodynamics. In the late 19th century, the photo-electric effect and the Rayleigh-Jeans ultraviolet catastrophe challenged this view on physics, and eventually lead to the revolutionary theory of quantum mechanics [Zub16]. The concept of quantization was first introduced by Max Planck in 1900 to resolve the UV catastrophe for black-body radiation [Pla01]. Satyendra Nath Bose later applied this idea to derive the Bose-Einstein statistics for photons [Bos24] and Albert Einstein extended Bose's theory to matter, predicting the Bose-Einstein condensate in 1925 [Ein05].

A Bose-Einstein condensate (BEC) is a quantum state of matter that can not be understood in terms of classical physics. According to the particle-wave duality that Louis de Broglie formulated in 1924, atoms start to reveal their wave-like nature at ultralow temperatures [DB24]. When Bose-Einstein condensation occurs, identical bosons collectively occupy the ground state and behave as a macroscopic quantum object that can be described by a single wave function. It took decades of development in laser technology and optical trapping and cooling techniques to reach sufficient phase-space densities required for the realization of the first Bose-Einstein condensates in 1995 [Dav95, And95] and the first degenerate Fermi gas in 1999 [DeM99]. In the case of fermions, the particles can not condense into the ground state because of the Pauli exclusion principle. Instead, they fill up the lowest energy levels up to the Fermi energy with at most one particle per quantum state.

Since the first degenerate Bose and Fermi gases were realized experimentally, the field of ultracold atoms has evolved rapidly. To date, there are 14 atomic species that have been Bose-Einstein condensed. The initial experiments focused on alkali metals, chosen for their relatively simple electronic structure with a single valence electron. Lanthanide atoms, in contrast, possess a more complex submerged-shell structure, resulting in a rich energy spectrum, large spin manifolds and permanent magnetic dipole moment in the ground state [Nor21]. The first lanthanide Bose-Einstein condensate

was achieved with dysprosium in 2011 at Stanford [Lu11]. Soon after, in 2012, bosonic erbium was brought to quantum degeneracy in our group [Aik12] and fermionic erbium followed in 2014 [Aik14].

In addition to the short-range, isotropic contact interaction that is also present in alkali atoms, ultracold dipolar atoms interact via the long-range, anisotopic magnetic dipole-dipole interaction. Feshbach resonances allow to tune the relative strength of the two types of interactions which enables the exploration of many-body physics such as the roton instability, the supersolid phase, and the self-bound quantum macrodroplet [Cho22]. Additionally, dipolar condensates can be prepared in different spin states or mixtures of spin states which gives rise to spin-dependent interaction dynamics [Bur16, Cla24]. Because they are well-isolated systems and offer a wide range of tunable parameters, experiments with ultracold dipolar atoms have emerged as promising platforms for quantum simulation, a concept that was first introduced by Richard Feynman in 1982 [Fey82]. He proposed to engineer well-controlled quantum systems for studying complex quantum phenomena that can not be simulated with classical computers. Many different platforms are being developed for this purpose: trapped ions, quantum dots, superconducting circuits, photons in nanostuctures and Rydberg atom arrays, just to name a few [Alt21]. Possible applications range from enhancing high-temperature superconductivity, investigating light-harvesting molecules in quantum chemistry to gaining insights into quantum gravity. Peter Zoller and others proposed to use ultracold atoms confined in optical lattices to realize Hubbard Hamiltonians from condensed-matter physics [Jak98, Jak05]. Experimentally, the quantum phase transition from superfluid to Mott insulator has been observed for the 3D Bose-Hubbard model [Gre02] and its extended version that includes dipolar interactions [Bai16]. Furthermore, the phase transition from superfluid to dipolar quantum solid has been demonstrated for the 2D Bose-Hubbard model [Su23]. Pushing the limits of quantum simulation further will require reducing calibration errors, decoherence and noise as well as cross-platform verification of results that can not be confirmed with classical computers [Dal22].

Optical trapping, cooling, and manipulation of particles for quantum simulation and other purposes requires precise control over light fields. For instance, the creation of the first optical tweezer by Arthur Ashkin and co-workers in 1986 relied on tight focusing of light with a lens that has a high numerical aperture (NA) [Ash86]. More recently, in 2023, a high-NA objective was crucial in achieving single-site resolution in a quantum gas microscope for erbium developed by the Greiner group [Su23]. In addition to high-NA optics, various devices have been designed to shape the intensity profile of light and therefore the trapping potential for the atoms. Acousto-optical modulators (AOMs) and acousto-optical deflectors (AODs) allow for precise displacement of laser beams, for example to create optical tweezer arrays [Coo18, Nor18]. Digital micromirror devices (DMDs) [Gau16] and liquid crystal spatial light modulators (LC SLMs) [Bar16] provide even greater flexibility in manipulate light, but they are more complex to implement. Another significant development in this field is the

invention of q-plates in 2006 by Lorenzo Marrucci's group in Naples, which enables the generation of spatially-dependent polarization profiles in light [Rub19].

The first part of my master thesis focuses on shaping the intensity profile of light; specifically, the implementation of an optical dipole trap with tunable aspect ratio in the ERBIUM experiment. The tunability is achieved by periodically displacing the dipole trap beam with an AOM. This scanning technique creates a flexible time-averaged potential for the atoms, similar to the first scanning optical dipole trap installed in the early stages of the experiment [Bai12]. The second part of my thesis explores the idea to generate light with a spatially-dependent polarization profile using q-plates. Given that erbium atoms interact with light in a polarization-dependent manner, this method offers a novel approach to engineering the potential landscape for the atoms.

The thesis is structured in the following way:

Chapter 2 reviews the properties of erbium and the main parts of the ERBIUM experiment.

Chapter 3 presents the relevant theory for atom-light interaction. First, we discuss the regime where the light is far-detuned from atomic transitions. This is typically the case for optical dipole traps to ensure essentially isotropic atom-light interaction and to minimize losses due to photon scattering. Secondly, we discuss the regime close to atomic resonances where the anisotropic polarizability of lanthanides leads to polarization- and state-dependent atom-light interaction.

Chapter 4 motivates the implementation of a new scanning optical dipole trap into the ERBIUM experiment and explains the basic idea of creating time-averaged optical potentials for the atoms by periodically displacing a beam with an AOM. The next section describes the electronics that create the radio-frequency signal to control the AOM. After presenting the optical setup and the offline testing results, the scanning ODT is implemented into the experiment and characterized by performing trap frequency measurements.

Chapter 5 introduces q-plates by reviewing the basics of representing polarization states of light, explaining the composition and working principle of q-plates and demonstrating how the polarization profile of a q-plate beam can be measured with projections onto the polarization basis states. From the intensity and polarization profile of a q-plate beam, we calculate the optical potential it creates for erbium atoms. Last, we discuss possible challenges for the implementation of q-plates.

Chapter 2

Overview on the properties of erbium and the ERBIUM experiment

Erbium is a rare-earth metal and part of the lanthanide (Ln) series, a family of 15 atoms with atomic numbers 51-71. Except for ytterbium, which possesses only filled electronic shells, all Ln elements exhibit an electron vacancy in a highly anisotropic shell (4f for all Ln excluding lanthanum and lutetium) that is surrounded by a fully occupied isotropic s-shell. This special electronic configuration, often referred to as a *submerged-shell structure*, gives rise to a series of unusual properties that make lanthanides especially interesting for ultracold experiments. In this chapter, which is mainly based on reference [Fri14], I will summarize the basic properties of erbium, describe how its electronic configuration leads to a rich energy spectrum and high magnetic moment compared to most other atomic species, and give a brief overview of the ERBIUM experiment.

2.1. Basic properties

Erbium (Er) is a silvery, soft metal in its solid form and has an atomic number of $Z = 68$. The rare-earth element can be separated from minerals that are contained in the earth's crust. Table 2.1 lists the relative natural abundance of the one fermionic and five bosonic isotopes. The relative atomic mass of erbium which is calculated by taking into account the natural abundance of each isotope is 167.26 u, where u is the atomic mass unit. The bosonic isotopes of erbium have a nucleus comprised of an even number of protons and neutrons. As a consequence, these isotopes possess a nuclear spin of zero ($I = 0$). Conversely, the fermionic isotope has an even number of protons but an odd number of neutrons which results in a nuclear spin of $I = 7/2$.

Table 2.1.: The six stable isotopes of Erbium with their natural abundances and quantum statistics.

Isotope	^{162}Er	^{164}Er	^{166}Er	^{167}Er	^{168}Er	^{170}Er
Natural abundance	0.14 %	1.61 %	33.6 %	23.0 %	26.8 %	15.0 %
Statistics	Boson	Boson	Boson	Fermion	Boson	Boson

2.2. Electronic configuration

As for all lanthanides in the ground state, 54 electrons compose the Xenon-like core of the electronic structure of erbium and the remaining ones distribute among the valence shells according to the Madelung rule. Of the 14 valence electrons in erbium, 12 electrons occupy the $4f$ shell that is surrounded by two electrons in the $6s$ shell:

$$(1s^2 2s^2 2p^6 3s^2 3p^6 3d^{10} 4s^2 4p^6 4d^{10} 5s^2 5p^6) 4f^{12} 6s^2 = [Xe] 4f^{12} 6s^2.$$

Figure 2.1 illustrates this electronic configuration and highlights the submerged-shell structure in the inset. While the surrounding $6s$ shell is completely filled, the $4f$ shell hosts two unpaired electrons in the $m_L = 2$ and $m_L = 3$ states. These electrons can be excited to other shells which gives rise to the rich energy spectrum of erbium. The anisotropy of the electronic wavefunctions of these states leads to the large angular momentum of erbium in its ground state.
For the ground state of erbium, the LS-coupling scheme, also known as Russel-Saunders coupling, applies. In this scheme, the electronic spin with associated quantum number S couples to the orbital angular momentum with quantum number L to result in the total angular momentum described by the quantum number $J = L+S$. The electronic state can be expressed in the usual spectroscopic notation $^{2S+1}L_J$, where L is labeled with $s = 0$, $p = 1$, $d = 2$, $f = 3$, ... For erbium, the ground state is

$$\text{g.s.}: \qquad {}^3H_6 \quad \text{where} \quad S = 1,\ L = 5,\ J = 6.$$

For the excited states, the jj-coupling scheme has to be applied since the strength of the spin-orbit interaction becomes comparable to the Coulomb interaction [Fri14]. In this scheme, the inner electrons in the [Xe]-like core and $4f$-shell couple with LS-coupling. The resulting total angular momentum $\mathbf{J}_1$ then couples to the angular momentum $\mathbf{J}_2$ of the outer electrons: $\mathbf{J} = \mathbf{J}_1 + \mathbf{J}_2$ which is denoted as $(J_1, J_2)_J$. Taking the 841 nm-transition as an example, one electron in the $4f$ shell can be excited to the $5d$ shell which results in a total angular momentum of $J = 7$:

$$841\,\text{nm ex.s.}: \qquad [Xe] 4f^{11} ({}^4I_{15/2}) 5d_{5/2} 6s^2 (15/2, 5/2)_7$$

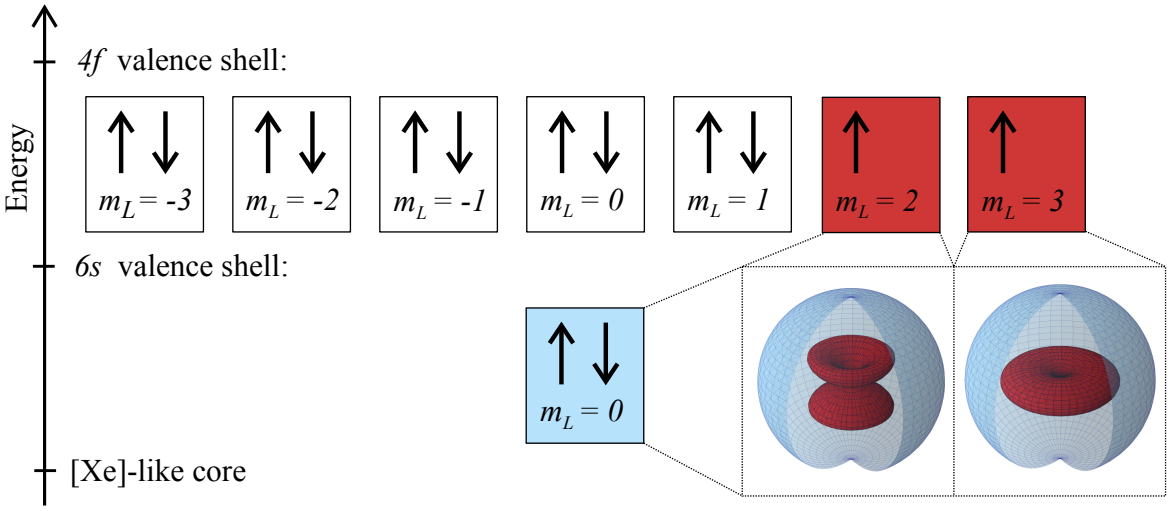

Figure 2.1.: Electronic configuration of erbium in the ground state. The inner 54 electrons can be summarized as a Xenon-like core. The $6s$ ($L = 0$) valence shell is fully occupied with two electrons. The $4f$ ($L = 3$) valence shell has an electron vacancy in each of the $m_L = 2$ and $m_L = 3$ states. The anisotropy of the electronic wavefunction corresponding to these states is shown in the figure inset (red plots). The surrounding symmetric $6s$ shell (blue plots) illustrates the submerged shell structure of erbium. The shape of the electronic wavefunctions is indicated by plotting the corresponding probability distribution, obtained from the absolute square of the spherical harmonics with indices L, m_L.

2.3. Energy spectrum

Lanthanides with a submerged-shell structure such as erbium feature a rich energy level spectrum compared to alkali and alkali-earth elements. The unpaired electrons can be easily excited, leading to more than 670 transitions observed so far [Kra23]. There are five laser-cooling transitions that have been identified for erbium. Table 2.2 lists their wavelengths, decay rates and natural linewidths. Figure 2.2 shows the full energy level scheme for erbium for wavenumbers below $26\,000\,\mathrm{cm}^{-1}$ together with the wavelengths relevant to our experiment. For the scope of this thesis, two wavelengths in the near-infrared regime are important: The far-detuned 1064 nm light is relevant for the new scanning optical dipole trap and the 841 nm transition is used for the simulations with q-plates.

Table 2.2.: The five optical transitions in erbium suitable for laser cooling [Ban05].

Wavelength λ	Decay rate Γ	Natural linewidth $\Delta\nu$
400.91 nm	$1.7 \times 10^8\,\mathrm{s}^{-1}$	29.7 MHz
582.84 nm	$1.0 \times 10^6\,\mathrm{s}^{-1}$	186 kHz
631.04 nm	$1.8 \times 10^5\,\mathrm{s}^{-1}$	28 kHz
841.22 nm	$5.0 \times 10^4\,\mathrm{s}^{-1}$	8.0 kHz
1299.21 nm	$13\,\mathrm{s}^{-1}$	2.1 Hz

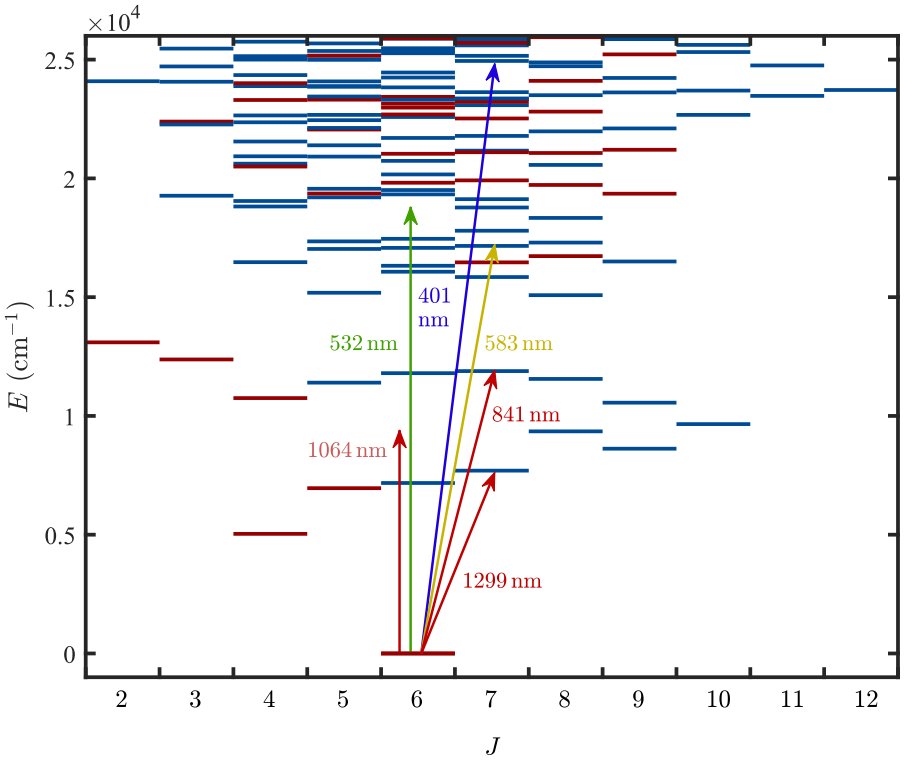

Figure 2.2.: Energy spectrum of erbium. Red and blue lines indicate states with even and odd parity. The arrows show wavelengths relevant to our experiment: The broad 401 nm line is suitable for an efficient operation of the Zeeman slower and transversal cooling. The 583 nm line is narrower, which means that a lower temperature can be reached in the magneto-optical trap. The narrow 1299 nm transition with a linewidth of 1.8 Hz makes coherent spin manipulation possible. The 1064 nm and 532 nm light is suitable for far-detuned optical dipole traps.

2.4. Magnetic moment

Another important property of erbium is its large magnetic moment μ in the ground state. It arises due to the large angular momentum of $J = 6$ from spin-orbit coupling in the submerged-shell structure. For bosonic erbium, the projection of the magnetic moment on the quantization axis set by an external magnetic field is

$$\mu = m_J \, g_J \, \mu_\mathrm{B} \tag{2.1}$$

where $\mu_\mathrm{B} = e\hbar/(2m_e)$ is the Bohr magneton and $m_J = -J, ..., J$ is the projection of the total angular momentum on the quantization axis. The Landé g-factor g_J for the total electronic angular momentum in the good approximation of LS-coupling is

$$g_J = 1 + (g_S - 1)\frac{J(J+1) + S(S+1) - L(L+1)}{2J(J+1)} \tag{2.2}$$

where $g_2 \approx 2.002$ is the Landé g-factor for the electron. In the ground state, $J = 6$ and $m_J = -6$, which results in a Landé g-factor of $g_J = 1.16$ and consequently the magnetic moment of erbium is

$$\mu = -6.98\,\mu_B.$$

Comparing to other atomic species, a magnetic moment of $\mu \gtrsim 5\mu_B$ is generally considered as "large". In fact, laser cooling of atomic species with a larger magnetic moment than erbium has only been achieved for holmium and dysprosium.

2.5. Creating a Bose-Einstein condensate in the ERBIUM experiment

This section gives a short overview of the steps to create a Bose-Einstein condensate in the ERBIUM experiment. Figure 2.3 shows the vacuum section which constitutes the main part of the experiment. Erbium granules are heated in an oven to 1100 °C and the atomic vapour passes through a set of apertures, called the hot lip, that is heated to 1200 °C. The atoms leave the oven section with an average velocity of about 430 m/s and enter the transversal cooling stage. Here, a 2D-optical molasses operating at the broad 401 nm line cools in the radial direction and collimates the atomic beam. Next, the Zeeman slower that also operates on the 401 nm transition, slows the atoms to a mean velocity of 5-10 m/s. Now, the atoms can be captured in the experimental chamber by the magneto-optical trap (MOT) that works on the more narrow 583 nm transition. In the MOT, about 2×10^7 atoms are cooled to a temperature of around 10 μK after 3 s. In the last step to reach quantum degeneracy, the atoms are loaded into a crossed optical dipole trap and are cooled evaporatively. With an optimized loading and cooling sequence that takes 12 s, we produce a BEC with typical atom numbers of 10^4 - 10^5 and condensate fractions of 60 - 70%.

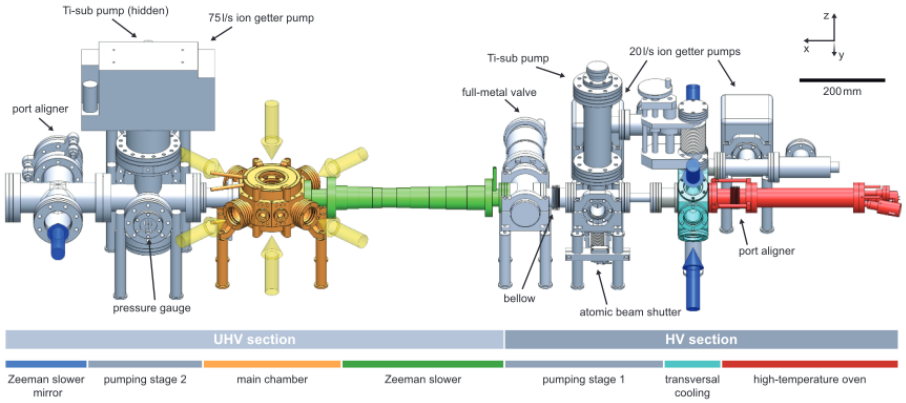

Figure 2.3.: Vacuum section of the ERBIUM experiment. Taken from [Fri14].

Chapter 3

Atom-Light interaction theory

Understanding the interaction of an atomic medium with light is the foundation to optical trapping of ultracold atoms. When atoms interacts with light, they experience an optical dipole potential which can be used for trapping. However, the scattering of photons leads to heating of the atoms. Both mechanisms go hand-in-hand, but their relative strength can be tuned by changing the frequency of the light. For light with a frequency sufficiently far away from atomic resonances (far-detuned regime), the scattering rate is negligible and the potential for the atoms, governed by the intensity profile of the light, becomes essentially conservative. The atoms are attracted to intensity maxima for red-detuned light, and repelled from them for blue-detuned light. For light close to resonance, the atom-light interaction becomes more intricate. Specifically for lanthanides, one has to take into account the anisotropic character of their electronic configuration. This leads to a dependence of the potential and the photon scattering on the angular momentum quantum numbers J and m_J, the direction of the magnetic field, the propagation direction of the light and the light's polarization vector.
In this chapter, the optical dipole potential and scattering rate will be introduced based on reference [Gri00] and we discuss the trapping of atoms in the far-detuned regime by relying on the intensity profile of a Gaussian beam. Furthermore, we consider the anisotropic atom-light interaction for lanthanides which plays an important role close to an atomic resonance.

3.1. Optical dipole potential and scattering rate

When an external electric field $\mathbf{E}$ is applied to matter, it induces a dipole moment $\mathbf{P}$ in the medium. The strength and direction of this induced dipole moment depend on the properties of the particles present in the material. These characteristics are

described by a single parameter, the polarizability α:

$$\mathbf{P} = \alpha\,\mathbf{E}. \tag{3.1}$$

In the framework of atom-light interaction, the electric field of the light

$$\mathbf{E} = \mathbf{u}\,E\,e^{i\omega t} + c.c., \tag{3.2}$$

with complex amplitude E, complex (normalized) polarization vector $\mathbf{u}$ and the frequency ω, causes the induced dipole moment in the atomic medium to oscillate at the same frequency ω as the driving field:

$$\mathbf{P} = \mathbf{p}\,P\,e^{i\omega t} + c.c., \tag{3.3}$$

where P is the complex amplitude and $\mathbf{p}$ the direction of the dipole.
The induced dipoles interact with the external electromagnetic field through an interaction potential U_{dip} and the scattering of photons at a rate Γ_{scat} [Gri00]:

$$U_{\mathrm{dip}}(\mathbf{r},\omega) = -\frac{1}{2}\langle\mathbf{P}\cdot\mathbf{E}\rangle = -\frac{1}{2\epsilon_0 c}\mathfrak{Re}\left[\alpha(\omega)\right] I(\mathbf{r}), \tag{3.4}$$

$$\Gamma_{\mathrm{scat}}(\mathbf{r},\omega) = \frac{\langle\dot{\mathbf{P}}\cdot\mathbf{E}\rangle}{\hbar\omega} = \frac{1}{\hbar\epsilon_0 c}\mathfrak{Im}\left[\alpha(\omega)\right] I(\mathbf{r}). \tag{3.5}$$

Here, $I(\mathbf{r}) = 2\epsilon_0 c|\mathbf{E}(\mathbf{r})|^2$ is the intensity of the light, ϵ_0 is the dielectric constant, c is the speed of light and the $\langle . \rangle$ denotes the time-average over fast-oscillating terms The interaction potential causes the atoms to experience a dipole force if there is a gradient of intensity:

$$\mathbf{F}_{\mathrm{dip}}(\mathbf{r},\omega) = -\nabla U_{\mathrm{dip}}(\mathbf{r},\omega) = \frac{1}{2\epsilon_0 c}\mathfrak{Re}\left[\alpha(\omega)\right]\nabla I(\mathbf{r}). \tag{3.6}$$

Consequently, the atoms are attracted to high intensity regions for $\mathfrak{Re}\left[\alpha(\omega)\right] > 0$, and pushed away from those regions for $\mathfrak{Re}\left[\alpha(\omega)\right] < 0$ (blue-detuned light).
While the real part of the polarizability is connected to the interaction potential and the in-phase oscillation of the induced dipole moment with the light, the imaginary part corresponds to the out-of-phase oscillation. This results in the absorption of light with power $P_{\mathrm{abs}} = \langle\dot{\mathbf{P}}\cdot\mathbf{E}\rangle$ that is re-emitted by spontaneous emission of photons with energy $\hbar\omega$. Due to the recoil from each photon, the atoms experience a scattering force

$$\mathbf{F}_{\mathrm{scat}}(\mathbf{r},\omega) = \hbar\mathbf{k}\Gamma_{\mathrm{scat}}(\mathbf{r},\omega). \tag{3.7}$$

that can lead to heating and atom loss.
To trap atoms, one needs to maximize the trapping potential while minimizing heating caused by photon scattering. From equations 3.4 and 3.5, it is clear that the strength of the two processes is determined by the atomic polarizability. From the simple Lorenz model of the atom as a driven oscillator, one obtains an expression of the polarizability from which it follows that the dipole potential scales as $1/\delta$ while

the scattering rate scales as $1/\delta^2$, where $\delta = \omega - \omega_0$ is the detuning from an atomics resonance at ω_0 [Gri00]. Therefore, atoms in optical dipole traps are illuminated with far-detuned light, meaning that the detuning δ from other transitions has to be much larger than their respective linewidths $\Delta\nu$. Furthermore, the Lorentz model tells us that $\mathfrak{Re}[\alpha(\omega)] > 0$ for red-detuned light ($\delta < 0$) and $\mathfrak{Re}[\alpha(\omega)] < 0$ for blue-detuned light ($\delta > 0$). Therefore, atoms are trapped in the high-intensity regions of optical dipole traps if one uses red-detuned light.
However, while the Lorenz model provides an intuitive picture for isotropic atom-light interaction, it is not sufficient for describing the polarizability of erbium. For this, a fundamental difference between lanthanides and other atomic species such as alkalis comes into play: Due to the anisotropy of the electronic wavefunction of lanthanides in the ground state, the atom-light interaction is anisotropic, i.e. depends on the direction and polarization of the incoming light with respect to the quantization axis. This is in stark contrast to e.g. alkali atoms where the polarizability in the ground state is isotropic and depends only on the wavelength of the light. Mathematically, this means that α in equation 3.14 is a scalar for isotropic polarizability and a tensor for anisotropic polarizability. This tensor can be split up into its diagonal, symmetric off-diagonal and antisymmetric off-diagonal elements that correspond to the so-called scalar, vectorial and tensorial part of the polarizability [Lep14].
Figure 3.1 shows the behavior of the real and imaginary parts of these three components as a function of the illumination wavelength on the atoms. In the far-detuned regime, we can see in figure 3.1(a) that the vectorial and tensorial parts become negligible compared to the scalar part, which means that the dipole potential for the atoms can be treated as isotropic. Specifically for 1064 nm light, we are in the red-detuned regime and for $\theta_p = \theta_k = 90°$ the scalar polarizability of $\alpha_s = 173$ a.u. makes up more than 98% of the total polarizability ($\alpha_{tot} = 176$ a.u.) [Bec18]. From Figure 3.1(b), we can infer that the photon scattering can still be anisotropic, however the scattering rate is very low because of the large detuning from any resonance. In contrast, close to an atomic resonance, e.g. the 841 nm line, we can see in Figure 3.1(a) that the vectorial and tensorial parts become comparable to the scalar part which means that the dipole potential for the atoms is anisotropic.
From this section, we can conclude that

- In the far-detuned regime, the polarizability can be treated as isotropic and losses are negligible. The trapping potential is determined by the intensity of the light. In section 3.2, we discuss optical dipole traps created by a Gaussian intensity profile.

- Close to an atomic resonance, the anisotropic polarizabilty of erbium has to be taken into account in addition to the intensity profile. We discuss the potential for the atoms in this case in section 3.3.

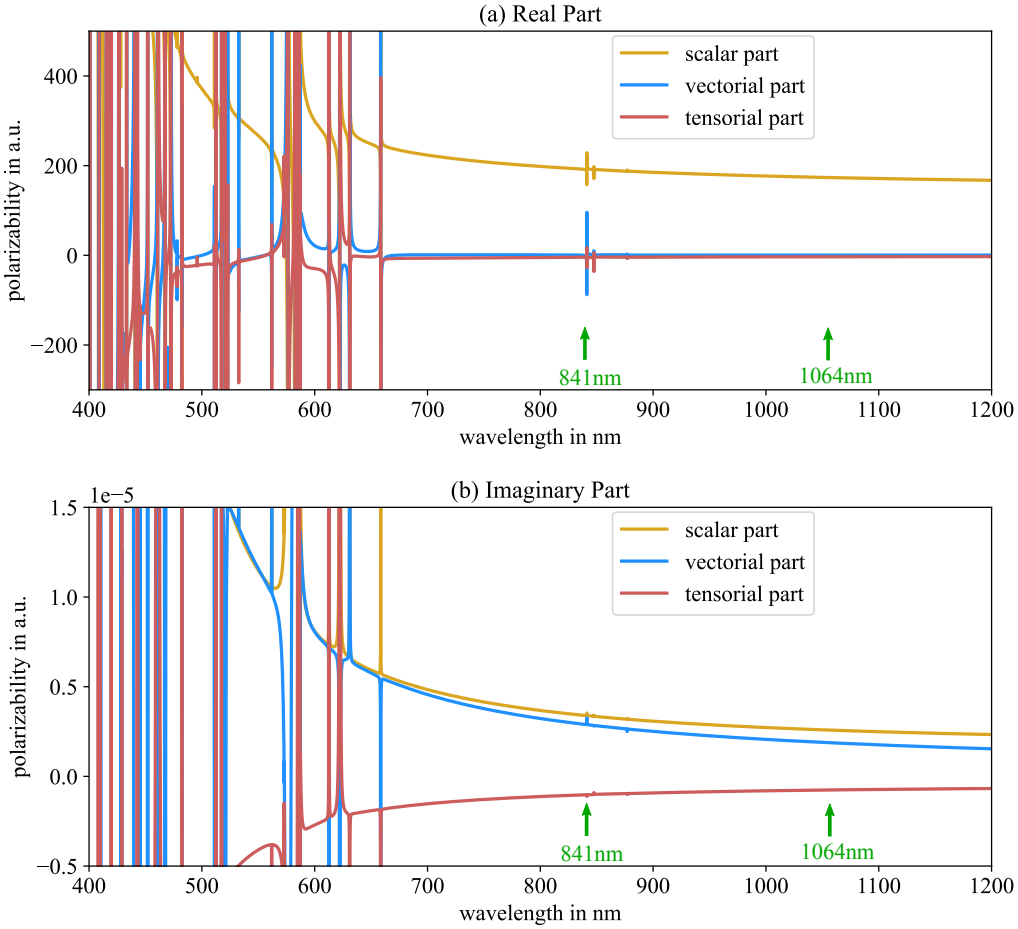

Figure 3.1.: Dynamical polarizability α of erbium in the ground state with the real part $\mathfrak{Re}[\alpha]$ relevant for trapping in (a) and the imaginary part $\mathfrak{Im}[\alpha]$ that determines the scattering rate in (b). A divergence in the polarizability is due to an atomic resonance, the finite peak height of narrow transitions comes from the finite number of calculated data points. For wavelengths far-detuned from atomic resonances, e.g. 1064 nm light, the scalar part of $\mathfrak{Re}[\alpha]$ dominates, making the atom-light interaction isotropic. In contrast, for wavelengths close to a resonance such as 841 nm light, the anisotopic nature of atom-light interaction plays an important role because of the non-vanishing vectorial and tensorial part of $\mathfrak{Re}[\alpha]$. Data taken from [Lep14].

3.2. Far-detuned optical dipole traps with Gaussian beams

In the previous section, we have seen that the atom-light interaction is almost isotropic and losses can be neglected in the far-detuned regime. Furthermore, we discussed that the optical dipole force arises to due to a spatial gradient of the light's intensity and that atoms are trapped in high-intensity regions for red-detuned light. Therefore, the easiest way to trap atoms is to shine a red-detuned focused Gaussian beam on

them. The intensity distribution $I(x, y, z)$ of a Gaussian beam propagating along the z-direction is determined by its total power P and its beam waists $w_{\{x,y\}}$ [Sal91]:

$$I(x, y, z) = \frac{2P}{\pi w_x(z) w_y(z)} \exp\left(-\frac{2x^2}{w_x^2(z)} - \frac{2y^2}{w_y^2(z)}\right). \tag{3.8}$$

The beam waists $w_{\{x,y\}}(z)$ denote the half beam diameter where the intensity drops to $1/e^2$ of its maximum value at the plane z. The waists evolve according to

$$w_{\{x,y\}}(z) = w_{0,\{x,y\}} \sqrt{1 + \left(\frac{z}{z_{\mathrm{R,\{x,y\}}}}\right)^2}, \quad \text{where} \quad z_{\mathrm{R,\{x,y\}}} = \frac{\pi w_{0,\{x,y\}}^2}{\lambda}. \tag{3.9}$$

Here $w_{0,\{x,y\}}$ is the waist at the focus ($z = 0$) and $z_{\mathrm{R,\{x,y\}}}$ is the Rayleigh length. Figure 3.2(a) illustrates the intensity profile of a Gaussian beam.
Now, we can insert the intensity of a Gaussian beam, see equation 3.8, into the formula for the dipole potential, equation 3.4. The potential minimum for the atoms is at the focus, where the intensity takes on its maximum value $I_0 = I(0, 0, 0)$. Consequently, the atoms are be located close to this point and we can derive the trapping potential here by performing a Taylor expansion of the intensity profile in equation 3.8. This results in a harmonic approximation of the energy landscape felt by the atoms around the focus point:

$$U(x, y, z) \approx U_0 \left(1 - \frac{2x^2}{w_{0,x}^2} + \frac{2y^2}{w_{0,y}^2} - \frac{z^2}{2}\left(\frac{1}{z_{R,x}} + \frac{1}{z_{R,y}}\right)^2\right), \tag{3.10}$$

where the trap depth U_0 is defined by:

$$U_0 = \mathfrak{Re}\left[\alpha(\omega)\right] I_0 = \mathfrak{Re}\left[\alpha(\omega)\right] \frac{2P}{\pi w_{0,x} w_{0,y}}. \tag{3.11}$$

Therefore, both in the plane and in the direction of propagation, the laser beam acts like a harmonic trap on the atoms. Comparing each term in equation 3.10 with a harmonic oscillator potential $U_{\mathrm{harm}} = \frac{1}{2} m \omega_r r^2$, we determine the trap frequencies

$$\omega_{\{x,y\}} = \sqrt{\frac{4U_0}{m w_{0,\{x,y\}}^2}} \quad \text{and} \quad \omega_z = \sqrt{\frac{2U_0}{m \tilde{z}_R^2}} \quad \text{with} \quad \left(\frac{1}{\tilde{z}_R}\right)^2 = \left(\frac{1}{z_{R,x}} + \frac{1}{z_{R,y}}\right)^2. \tag{3.12}$$

Here, we have defined the average Rayleigh length $\tilde{z}_R$. Figure 3.2(b) shows an intensity profile in the x-y plane together with the trapping potential defined by the trap depth U_0 and trap frequencies $\omega_{\{x,y\}}$.
One can easily calculate the ratio of the trap frequencies $\omega_z/\omega_r = \lambda/(\sqrt{2}\pi w_{0,r})$ if we assume a symmetric trap in the radial direction ($w_{0,\{x,y\}} = w_{0,r}$) for simplicity. Therefore, in the typical case of $\lambda \ll w_{0,r}$, the confinement in z-direction is much smaller than in the radial direction. If ω_z in an optical dipole trap is not sufficient, another focused beam has to be added at an angle with respect to the first one, creating a crossed optical dipole trap. For a maximum confinement in all directions, the beams have to be crossed at an angle of 90°.

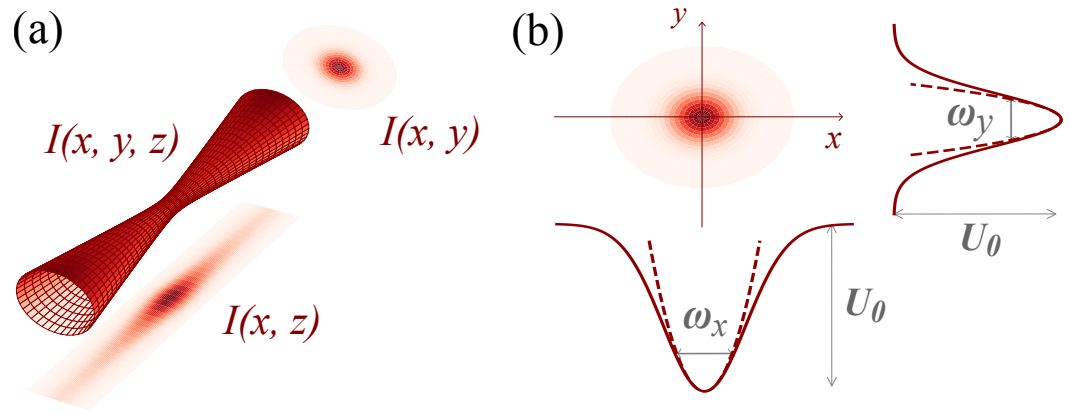

Figure 3.2.: Figure (a) shows the intensity profile $I(x, y, z)$ of a Gaussian beam for a fixed radius $r = \sqrt{x^2 + y^2}$, the intensity profile $I(x, z)$ for $y = 0$ as well as the intensity profile $I(x, y)$ for for $z = 0$. Figure (b) depicts again $I(x, y)$ which is directly proportional to the optical dipole trap potential $U_{\mathrm{dip}}(x, y)$. The red curves show the Gaussian shape of the potential along x with $y = 0$ and vice-versa. The red dotted curves indicate the harmonic approximation close to the trap center. The two trap parameters that define the harmonic trap are the trap depth U_0 and the trap frequency $\omega_{\{x,y\}}$ in each direction.

3.3. Atom-light interaction close to resonance: Anisotropic polarizability

When the frequency of the light is close to an atomic resonance, the internal structure of the atom starts to play a crucial role, making the atom-light interaction more complicated than in the far-detuned case. Specifically in erbium, the highly anisotropic wave functions of the unpaired electrons in the $4f$ shell give rise to an anisotropic polarizability. Useful references regarding this topic are [Bel09, Kie12, Lep14, Li17]. With the 3×3 atomic polarizability tensor split into scalar, vectorial and tensorial contributions of the interaction, the potential for the atoms is [Lep14]

$$\begin{aligned} U(\omega) &= U_{\mathrm{scal}} + U_{\mathrm{vect}} + U_{\mathrm{tens}} \\ &= -\frac{1}{2\epsilon_0 c} I(r) \left[\mathfrak{Re}\left[\alpha_{\mathrm{scal}}(\omega)\right] + \mathcal{A}\cos(\theta_k)\frac{m_J}{2J}\mathfrak{Re}\left[\alpha_{\mathrm{vect}}(\omega)\right] \right. \\ &\quad \left. + \frac{3m_J^2 - J(J+1)}{J(2J-1)} \times \frac{3\cos^2(\theta_p) - 1}{2}\mathfrak{Re}\left[\alpha_{\mathrm{tens}}(\omega)\right] \right] \end{aligned} \tag{3.13}$$

Here, $\mathcal{A} = i(\mathbf{u}^* \times \mathbf{u}) \cdot \mathbf{k}$ is the degree of ellipticity of the polarization with $\mathbf{u}$ the normalized (complex) polarization vector and $\mathbf{k}$ the propagation direction of the light. Hence, $\mathcal{A} = 0$ for linearly polarized light, $\mathcal{A} = \pm 1$ for left/right circularly polarization and $0 < |\mathcal{A}| < 1$ for elliptical polarization. Furthermore, ϵ_0 is the vacuum permittivity, c is the speed of light and λ is the wavelength of the light. The atomic state is characterized by the angular-momentum quantum number J and its projection onto the quantization axis m_J. The quantization axis is typically set by an external magnetic

field **B** that defines the angle θ_k with the propagation direction of the light and the angle θ_p with the polarization vector, as illustrated in figure 3.3. The individual parts

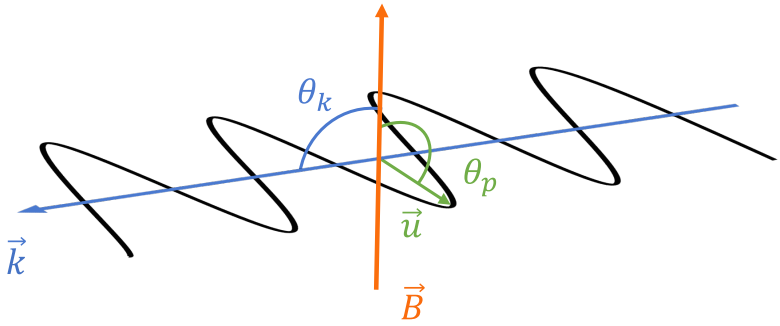

Figure 3.3.: Schematic illustration of the angles and vectors in equation 3.13. The angle θ_k is determined by the propagation direction of light **k** and the magnetic field **B**. The angle θ_p is defined by the orientation of the light's polarization **u** and the magnetic field.

of the polarizability are given by [Li17]

$$\begin{aligned}
\alpha_{\text{scal}}(\omega) &= -\sqrt{\frac{1}{3(2J+1)}}\alpha_J^{(0)}(\omega) \\
\alpha_{\text{vect}}(\omega) &= \sqrt{\frac{2J}{(J+1)(2J+1)}}\alpha_J^{(1)}(\omega) \\
\alpha_{\text{tens}}(\omega) &= \sqrt{\frac{2J(2J-1)}{3(J+1)(2J+1)(2J+3)}}\alpha_J^{(2)}(\omega),
\end{aligned} \tag{3.14}$$

where the coupled polarizability $\alpha_J^{(K)}(\omega)$ with $K = 0, 1, 2$ is given by a sum over all transitions $J \to J'$ that are dipole-allowed $(J' - J = 0, \pm 1)$

$$\begin{aligned}
\alpha_J^{(K)}(\omega) = \sqrt{2K+1} \sum_{J'} (-1)^{J+J'} \\
\times \begin{Bmatrix} 1 & 1 & K \\ J & J & J' \end{Bmatrix} |\langle J||\mathbf{d}||J'\rangle|^2 \\
\times \frac{1}{\hbar}\left(\frac{1}{\omega_{JJ'} + i\gamma_{J'}/2 + \omega} + \frac{(-1)^K}{\omega_{JJ'} + i\gamma_{J'}/2 - \omega}\right).
\end{aligned} \tag{3.15}$$

Here, $\omega_{JJ'}$ is the transition frequency and $\gamma_{J'}$ is the natural linewidth of the excited state. The curly brackets indicate the Wigner-6j symbol and the squared reduced dipole moment $|\langle J||\mathbf{d}||J'\rangle|^2$ is given by [Li17]

$$|\langle J||\mathbf{d}||J'\rangle|^2 = \pi\epsilon_0\hbar c^3 \frac{(2J'+1)\gamma_{J'}}{\omega_{JJ'}^3} \tag{3.16}$$

According to equation 3.5, the scattering rate can found replacing the real parts $\mathfrak{Re}[\alpha_i]$ with the imaginary parts of the polarizability $\mathfrak{Im}[\alpha_i]$ in equation 3.13. The real and

imaginary part of the scalar, vectorial and tensorial parts of the polarizability for the 841 nm transition are shown in figure 3.4. The data is calculated with equations 3.14 and 3.15 where the values for $\omega_{JJ'}$ and $\gamma_{J'}$ are determined via a semi-empirical model described in [Lep14].

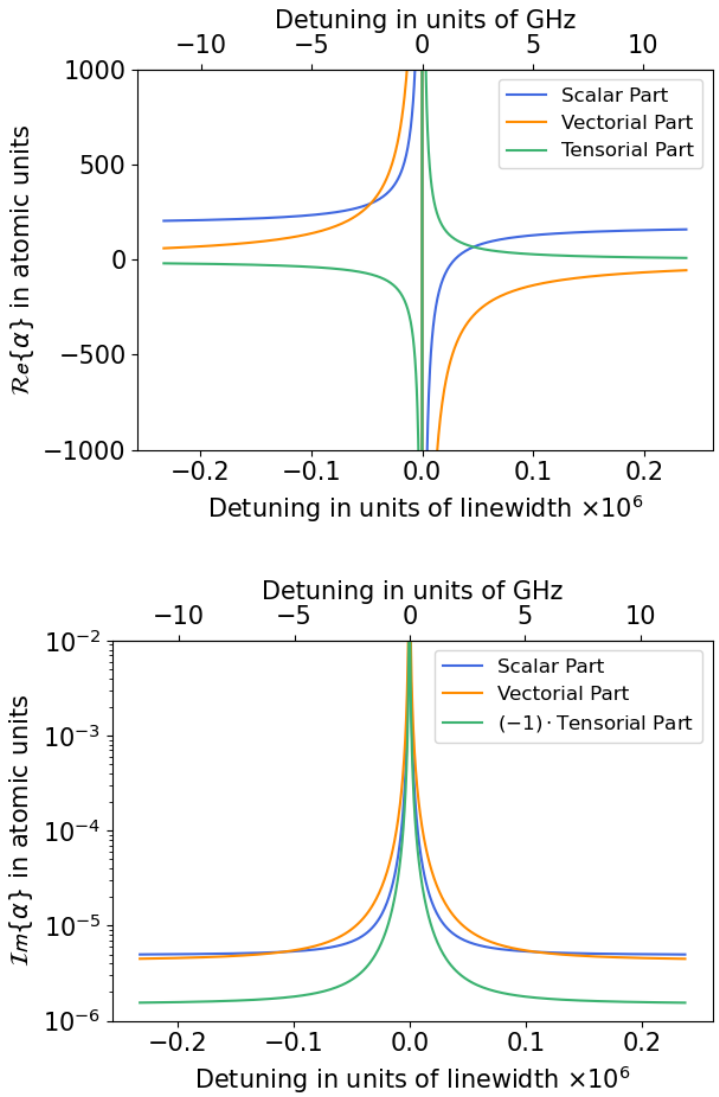

Figure 3.4.: Real and imaginary parts of the polarizability close to the 841 nm transition, calculated as described in [Lep14]. The linewidth of the transition is $\Gamma_{841} = 2\pi \times 8\,\mathrm{kHz}$.

Chapter 4

A new scanning ODT for the ERBIUM experiment

Optical dipole traps are an essential ingredient for ultracold experiments, allowing for cooling and manipulation of neutral atoms. This requires active control of the trap parameters: Specifically, tuning the geometry of the trap has proven to be an important tool. Just to give one example, the implementation of an optical dipole trap with a tunable geometry in the early stages of the ERBIUM experiment tripled the number of atoms in the BEC [Bai12].
This chapter will first explain why an ODT with a tunable geometry is advantageous when creating a BEC and motivate why the old ODT in the ERBIUM experiment had to be replaced. Furthermore, we discuss how a tunable geometry is realized by creating a time-average potential for the atoms with a scanning ODT beam. The next sections go into the technical details of the optical setup and electronics as well as the offline testing. Last, we describe the implementation of the setup into the experiment and perform trap frequency measurements with the atoms.

4.1. Why a (new) scanning ODT?

A scanning optical dipole trap provides the flexibility to change the trap geometry by controlling the ellipticity of the Gaussian beam that creates the trap. This tool can improve the efficiency of loading atoms from the MOT to the ODT and enhance evaporative cooling, as well as giving the possibility to tune trap geometry and therefore the mean-field contribution of the dipole-dipole interaction. While these aspects also apply for the previously installed scanning ODT, we discuss the technical reasons why a new one was needed.

Improving the efficiency of ODT loading and evaporative cooling

To reach quantum degeneracy in the ERBIUM experiment, the atoms are loaded from the MOT into a crossed ODT and cooled evaporatively. The crossed ODT consists of two crossed and tightly focused Gaussian beams - but how tightly do they have to be focused exactly? To explore this question, one has to consider two issues, as illustrated in figure 4.1:

(a) When transferring the atoms into the ODT, a larger spatial overlap with the MOT beam will lead to a higher loading rate.

(b) On the other hand, a tighter trap ensures a larger atomic density and therefore faster thermalization during the evaporative cooling sequence.

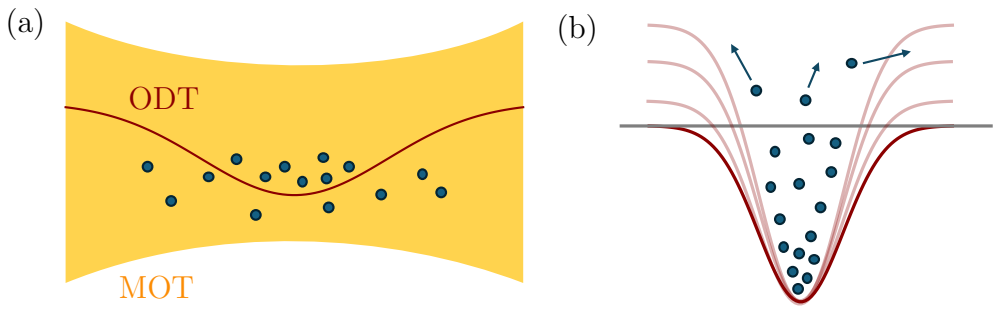

Figure 4.1.: Illustration of two steps in the experimental sequence where the size of the ODT beam is relevant: (a) For loading from the MOT into the ODT, a larger waist corresponds to a higher loading rate. (b) For evaporative cooling, a smaller waist means a higher collision rate and therefore faster thermalization of the atoms that remain in the trap.

In principle, it is possible to reach quantum degeneracy with evaporative cooling if one fixes the beam waist and sequentially lowers the trap depth U_0 by reducing the light power P (since $U_0 \propto P$ according to equation 3.11). During each evaporation step, the temperature decreases because the hottest atoms are lost from the trap which cuts off the high-energy tail of the Maxwell-Boltzmann distribution [Ols13]. Then, the atoms rethermalize via elastic collisions and the high-energy tail can be cut again in the next evaporation step. However, reducing the power also causes the trap frequency to increase (since $\omega \propto \sqrt{P}$, see equation 3.12). This leads to a lower atomic density and therefore a lower thermalization rate.
Therefore, it is advantageous to control the trap depth and trap frequency more independently by having the possibility to dynamically tune the size of the beam waist. To achieve this, the idea is to change the beam waist in one direction for one of the

beams of the crossed ODT, going from a larger beam during ODT loading to a smaller beam during evaporative cooling.

Tuning the dipole-dipole interaction

Due to the large permanent magnetic moment in the ground state (see section 2.4), erbium atoms interact via the magnetic dipole-dipole interaction (DDI). When an external magnetic field is applied to the dipoles, they align along the magnetic field and the interaction potential between two atoms becomes [Fri14]

$$U_{\mathrm{DDI}}(\theta, r) = \frac{\mu^2 \mu_0}{4\pi} \frac{1 - 3\cos^2\theta}{r^3}. \tag{4.1}$$

Here, θ is the angle between the magnetic field $\mathbf{B}$ and the position vector $\mathbf{r}$ connecting the two atoms and $r = |\mathbf{r}|$ is the distance between the atoms, as illustrated in figure 4.2. Since the DDI decays with $1/r^3$ and depends on the orientation of the

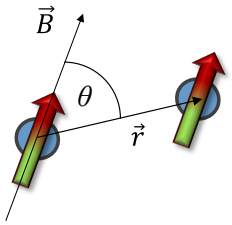

Figure 4.2.: Illustration of the parameters relevant for the magnetic dipole-dipole interaction in erbium. The interaction strength depends on the distance $r = |\mathbf{r}|$ between the atoms and the angle θ which is spanned by the magnetic field $\mathbf{B}$ and the position vector $\mathbf{r}$ connecting the two atoms.

dipoles θ, the interaction is *long-range* and *anisotropic*. This is in stark contrast to the isotropic, short-range contact interaction that is present in ultracold quantum gases of any atomic species.
Notably, the relative strength of the dipole-dipole and contact interaction can be varied. The contact interaction at ultralow temperatures can be fully characterized by the s-wave scattering length a_s that can be tuned by making use of *Feshbach resonances* [Chi10]. This phenomenon occurs when scattering states couple to molecular states of two bound atoms. Since the molecular states posses a different magnetic moment, the relative energy of the collision channels can be tuned due to the Zeeman effect. The scattering length around the resonance depends on the applied magnetic field strength B with

$$a_s = a_{\mathrm{bg}} \frac{\Delta}{B - B_0}, \tag{4.2}$$

where a_{bg} is the background scattering length, Δ is the width of the resonance and B_0 its position. With Feshbach resonances, the relative strength of a_s and the so-called dipolar length $a_{\mathrm{dd}} = \mu_0 \mu^2 m / 12\pi\hbar^2$ that characterize the dipole-dipole interaction can

be controlled.
Extending the dipole-dipole interaction potential for two magnetic atoms in equation 4.1 to the many-body case is not trivial. However, if the condensate is dilute enough so that correlations between the atoms can be neglected (mean-field regime), one can take the average over the magnetic fields produced by the atoms and describe the dipole-dipole interaction potential as a "mean field" with equation 4.1 [Cho22]. In this simple picture, one can understand that the interaction properties of a Bose-Einstein condensate of erbium can be tuned by changing the trap geometry and orientation of the magnetic field. Let's consider a trap that is elongated in one direction ("cigar-shaped trap"): If the magnetic field is oriented along this direction, the dipoles are in a head-to-tail configuration and the DDI is attractive. In contrast, if the magnetic field is oriented orthogonally to this direction, the dipoles in a side-by-side configuration and the DDI is repulsive.
By tuning the dipolarity of the atomic sample, exotic phases of matter were observed in our group with ^{166}Er. When the s-wave scattering length is tuned sufficiently below the dipolar length in a cigar-shaped trap with attractive DDI, the atoms concentrate in a high-density, self-bound state, called a macrodroplet shown in figure 4.3 [Cho16]. The shape of the droplet is preserved by the balance between the attractive dipolar forces and effective repulsive forces that result from quantum fluctuations, an effect which can not be described within mean-field theory.

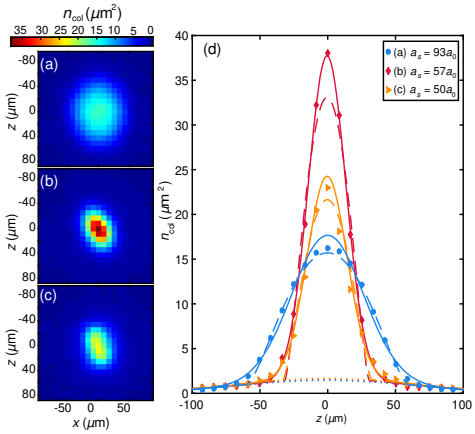

Figure 4.3.: Observation of the transition from BEC to macrodroplet with ^{166}Er ($a_{dd} = 65.6\,a_0$). Figures (a)-(d) show the atomic density distribution obtained from time-of-flight absorption images for three different scattering lengths. In figure (d), the dashed lines corresponds to a mean-field Thomas-Fermi (MF-TF) model on top of a Gaussian profile that accounts for the thermal part, and the solid lines correspond to a two-Gaussian fit. For $a_s = 93\,a_0 > a_{\mathrm{dd}}$, the density profile is well described by the TF-MF model. For $a_s = 57\,a_0 < a_{\mathrm{dd}}$, the system is in the macrodroplet phase and deviates from the TF-MF model. This is also the case for $a_s = 50\,a_0$, but in addition, the droplet core looses atoms due to three-body losses that increase with the atom density. Figure taken from [Cho16].

For a cigar-shaped trap with the magnetic field perpendicular to the long axis, the dipole-dipole interaction is repulsive. When the s-wave scattering length is reduced

below a critical value that depends on the exact trap geometry, a phase transition from the BEC to a supersolid phase takes place [Nat19]. In the supersolid, a density modulation coexists with global phase coherence. However, this phase only appears within a small region of the scattering length. For even lower values of a_s, the global phase coherence disappears and the system enters a phase of insulating droplets.

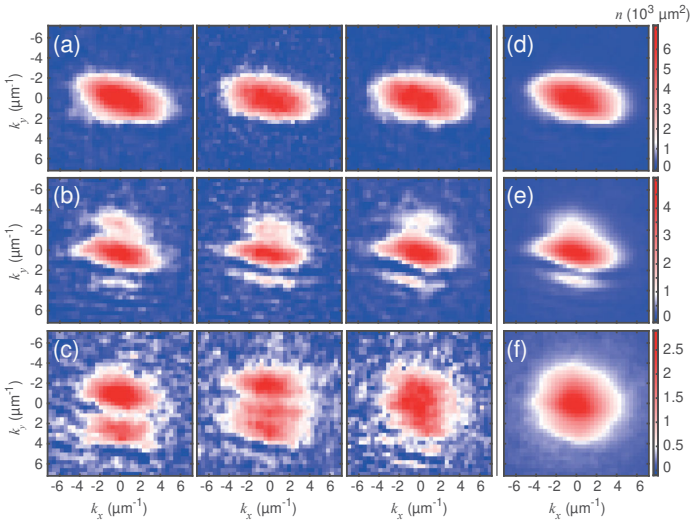

Figure 4.4.: Observation of the transition from BEC to the supersolid phase to the insulating droplet regime with ^{166}Er ($a_{dd} = 65.6\,a_0$). Figures (a)-(c) show examples of time-of-flight absorption images taken in the experiment, figures (d)-(f) show the average over 100 images. The first row with $a_s = 54.7(2)\,a_0$ corresponds to a dilute BEC without density modulations. In the second row with $a_s = 53.8(2)\,a_0$, the consistent interference pattern indicates the supersolid phase for the *in situ* state. In the third row with $a_s = 53.3(2)\,a_0$, more complicated patters appear that vary from shot to shot. This points to the loss of phase coherence in the insulating droplet regime. Figure taken from [Nat19].

Rebuilding the crossed ODT in the ERBIUM experiment

In the original setup of 2012, the old scanning ODT formed a crossed ODT together with a second 1064 nm beam [Bai12]. When I joined the team for my master project, the crossed ODT consisted of the old scanning ODT and a green 532 nm beam, as shown in figure 4.5(a). The 532 nm beam path had been implemented as part of a 3D optical lattice [Bai16]. The configuration of the red and green ODT beams is not ideal, since the two beams are not crossing at an angle of 90 degrees. Therefore, the trap frequencies in the two horizontal directions are coupled, so whenever one changes the power in one beam it affects both frequencies. Furthermore, the green path is needed to reinstall the lattice for the next projects. Therefore, it became clear that a new setup, as shown in Figure 4.5(b), has to be realized. Here, the new scanning ODT is built on the breadboard on the lower right and creates a crossed ODT together with

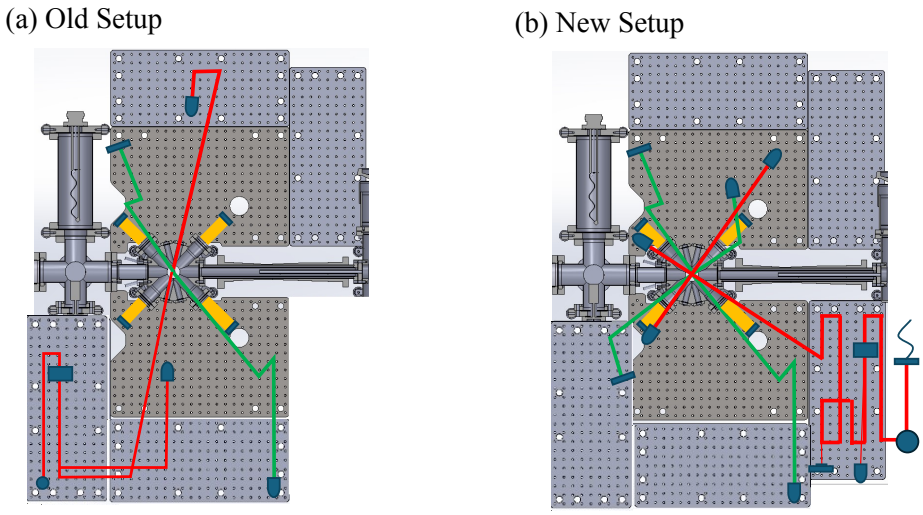

Figure 4.5.: Setup on the experimental table. The atomic beam arrives from the right and is captured in the experimental chamber in the center by the MOT (yellow light). In the old setup (a), the scanning ODT does not cross the green ODT beam at 90 degrees. This problem is resolved in the new setup (b), where the scanning ODT comes from the breadboard on the lower right and crosses the second red ODT perpendicularly. The optical path for the green light can be used to reinstall the green lattice.

a second 1064 nm beam at 90 degrees. After the new crossed ODT is installed, the green lattice can be reimplemented.

4.2. Principle of a scanning ODT

The idea of a scanning ODT is to periodically "scan" the position of a Gaussian beam fast enough along one direction so that the atoms effectively experience a time-averaged potential. The exact shape of this potential is determined by the choice of the modulation function and the scanning is fast enough if the atomic cloud cannot follow the motion of the beam. Since the timescale of the collective movement of the atoms is given by the trap frequency ω_{trap}, the periodic modulation has to happen much faster:

$$\omega_{\text{scan}} \gg \omega_{\text{trap}}. \tag{4.3}$$

A suitable device to implement a scanning ODT is an acousto-optical modulator (AOM). The main parts of an AOM are a piezo-electric transducer attached to a crystal, typically made of tellurium dioxide (TeO_2), crystalline quartz or fused silica. When a radio-frequency (RF) signal is sent to the transducer, it creates an acoustic wave in the crystal that acts as a diffraction grating for light. Consequently, an incident beam gets diffracted into different orders if it enters a certain angle θ_{B} given by

the Bragg condition [AAo13]:

$$\theta_{\mathrm{B}} = \frac{\lambda}{2\lambda_s} = \frac{\lambda \nu_{\mathrm{AOM}}}{2c_{\mathrm{s}}}. \tag{4.4}$$

Here, λ_s is the wavelength of the acoustic wave which can be expressed in terms of the RF-frequency ν_{AOM} and the speed of sound in the crystal c_{s}. Usually, AOMs are manufactured so that up to 85% of the light can be diffracted into the ±1st diffraction order. This is possible only if one sends in the optimal RF power on the order of a few Watts and chooses the specified center frequency of the RF-signal ν_{AOM} which is typically around 80-110 MHz. For most applications of AOMs, such as frequency-shifting or controlling the amount of light going into an optical path, the RF-signal is set to the center frequency. The bandwidth BW of an AOM indicates the deviation from the center frequency at which the diffraction efficiency into the 1st order decreases by 3 dB.
For the scanning ODT, the idea is to send an RF-signal to the AOM that varies periodically around the center frequency. Therefore, the beam in the ±1st order is diffracted into slightly different angles within the bandwidth BW of the AOM. A lens positioned at a distance of its focal length after the AOM translates the deflection into a horizontal displacement of the beam. Figure 4.6 illustrates how this technique can transform a Gaussian beam with a symmetric intensity profile into a beam that is elliptical in the time-average.

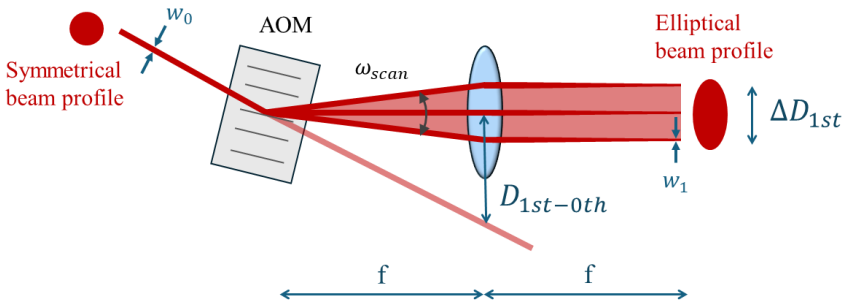

Figure 4.6.: Principle of a scanning optical dipole trap: The symmetric Gaussian intensity profile is transformed into a elliptical shape in the time-average. This is achieved by slightly varying the angle of the first diffraction order of the AOM at the scanning frequency ω_{scan} and making the diffracted beams parallel with a lens.

The aspect ratio AR of the ellipse is given by the effective waist along the scanning direction (y-direction) with respect to the waist in the direction without scanning (x-direction), which corresponds to the inverse of ratio of the trap frequencies according to equation 3.12:

$$AR = \frac{w_y}{w_x} = \frac{\omega_x}{\omega_y}. \tag{4.5}$$

By changing the width of the RF-signal in frequency space, the aspect ratio can be tuned from $AR = 1$ to its maximum value AR_{max}. The next paragraph will focus on

the calculation of $AR_{\max}$, following reference [Koh07]. The maximum aspect ratio is given by $\Delta D_{1\mathrm{st}}$, the distance by which the 1st order beam can be deflected within the bandwidth of the AOM, and w_1, the waist at the focus of the lens (see figure 4.6):

$$AR_{\max} = \frac{\Delta D_{1\mathrm{st}}}{2w_1}. \tag{4.6}$$

To evaluate this expression, we first note that the ratio of bandwidth and center frequency of an AOM can be expressed as

$$\frac{BW}{\nu_{\mathrm{AOM}}} = \frac{\Delta D_{1\mathrm{st}}}{D_{1\mathrm{st}-0\mathrm{th}}}, \quad \text{with} \quad \theta \approx \tan\theta = \frac{D_{1\mathrm{st}-0\mathrm{th}}}{f}. \tag{4.7}$$

Here, $D_{1\mathrm{st}-0\mathrm{th}}$ is the separation of the 0th and 1st order at the lens, which can be calculated from the angle θ between the 0th and 1st order and the focal length f of the lens. Furthermore, we can express w_1 with the formula of focusing a Gaussian beam with initial waist w_0:

$$w_1 = \frac{f\lambda}{\pi w_0}. \tag{4.8}$$

Combining equations 4.6 - 4.8, the maximum aspect ratio is

$$AR_{\max} = \frac{\Delta D_{1\mathrm{st}}}{2w_1} = \frac{\pi w_0\, \theta\, BW}{2\lambda\, \nu_{\mathrm{AOM}}}. \tag{4.9}$$

In the last step, we use that the angle between the 0th and 1st order is twice the Bragg angle: $\theta = 2\theta_{\mathrm{B}}$ and θ_{B} is given by equation 4.4. We arrive at the final result for the maximum aspect ratio:

$$AR_{\max} = \frac{\pi}{2}\frac{BW}{c_{\mathrm{s}}}\, w_0. \tag{4.10}$$

Note that the maximum aspect ratio depends only on two AOM properties and the initial waist of the beam. In our scanning ODT setup, we use the AOM 3080-197 by Gooch&Housego, see table 4.1 for an overview of its technical specifications. The aperture of the AOM limits the initial waist to $w_0 = 0.8\,\mathrm{mm}$, so we expect a maximum aspect ratio of

$$AR_{\max} \approx 9.$$

To estimate the trap parameters we can achieve in this case, we choose a typical value of $20\,\mu\mathrm{m}$ for the waist at the position of the atoms. The values of the trap depth and trap frequency are given by equations 3.11 and 3.12 while the polarizability of 1064 nm light is $\mathfrak{Re}[\alpha_{tot}] = 176\,\mathrm{a\,u}$ according to reference [Bec18]. Figure 4.7 shows the calculated trap depth and frequency of the scanning ODT in a range from $AR = 1$ to $AR_{\max} = 9$ for typical values of the power in the ODT beam.

4.3. Electronics for the RF-signal driving the AOM

The electronic components in this setup play a key role in creating time-averaged potentials for the atoms, since they produce the radio-frequency signal controlling the

Table 4.1.: Technical specifications of the AOM given by the manufacturer. We observed that the beam was cut for a waist above 0.8 mm.

Model	G&H 3080-197
AOM crystal	TO_2
acoustic velocity c_s	4.2×10^3 m/s
Center frequency ν_{AOM}	80 MHz
Bandwidth BW	±15 MHz
RF power	1.5 W
Max. Coupling efficiency at 1 mm beam waist	85%

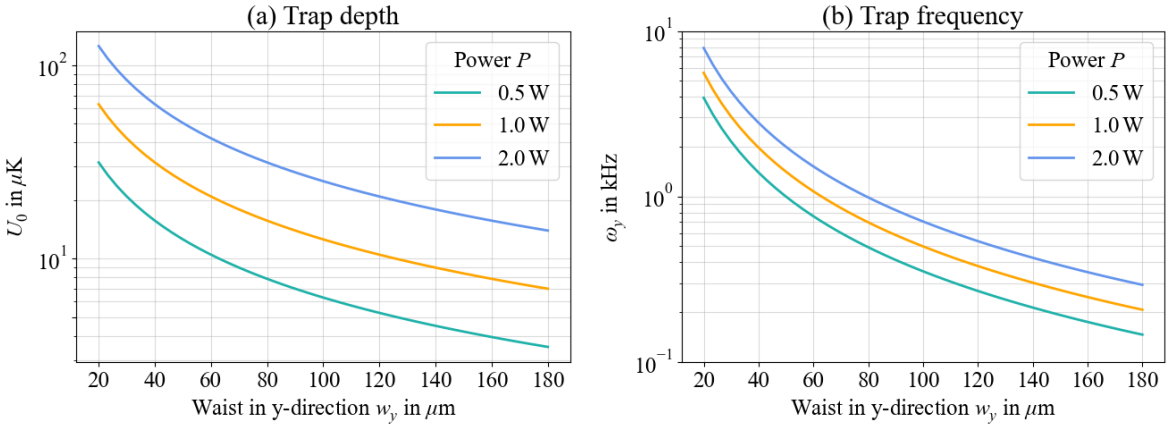

Figure 4.7.: Trap depth U_0 and trap frequency ω_y of the scanning optical dipole trap as a function of the beam waist w_y for a different laser powers P. Here, the waist in the x-direction is constant at $w_x = 20\,\mu$m and the waist in the y-direction changes for different scanning amplitudes, ranging from $w_y = 20\,\mu$m ($AR = 1$) to $w_y = 180\,\mu$m ($AR_{max} = 9$).

AOM. Within the work for my master thesis, I was able to simplify the electronics compared to the scanning ODT installed previously in the experiment [Bai12], making the implementation, control and troubleshooting easier.
The idea of a scanning ODT requires the generation of a frequency-modulated RF-signal ("scanning signal") that is sent to the AOM. The modulation signal is of the form

$$U_{signal}(t) = A \cdot f(\omega_{scan} t) + y_0. \tag{4.11}$$

Here, the offset y_0 determines the center frequency of the scanning signal and the scanning amplitude A sets the bandwidth of the scanning signal in frequency space. The periodic function $f(t)$ with the modulation ("scanning") frequency ω_{scan} gives the shape of the scanning signal. The electronics that create the scanning signal have to fulfil the following requirements:

- The offset y_0 has to be tunable to set the center frequency of the scanning signal

at the center frequency of the AOM.

- The scanning amplitude A has to be controllable to adjust the bandwidth of the scanning signal, ranging from a single-frequency peak (no scanning) to using the full bandwidth of the AOM (maximum scanning).

- There has to be the possibility to arbitrarily choose the function $f(t)$ to find the right one that maintains a Gaussian beam shape of the ODT beam for all scanning amplitudes. To ensure a symmetric beam profile, the scanning signal has to be symmetric around the center frequency for all scanning amplitudes.

- According to equation 4.3, the scanning frequency ω_{scan} has to be much larger than the trap frequency.

- The power of the scanning signal has to be tunable by multiplying it with some gain factor U_{gain}. This changes the diffraction efficiency into the first order of the AOM which allows for adjusting the power in the ODT beam.

In principle, it would be possible to fulfill all those requirements by creating a frequency-modulated (FM) signal with an arbitrary function generator. However, the parameters A, y_0 and G have to be accessible by the control software of the experiment. This requires some additional electronics that make it more convenient to build an electronic circuit where the modulation signal is created with an arbitrary function generator, but the frequency-modulated signal is created with a *voltage-controlled oscillator (VCO)*. We will now have a look at the electronic circuit for offline testing of the scanning ODT. The final electronics box designed for the implementation into the experiment is presented in the appendix A.1.
In the electronic circuit for offline testing shown in figure 4.8, an arbitrary function generator[1] controls the VCO[2] that is powered with a supply voltage of 24 V and can produce output RF-signals with a bandwidth of 50-110 MHz. The VCO output is sent to two RF-amplifiers that are connected in series before the RF-signal reaches the AOM.
To produce the right scanning signal, careful tuning of the VCO control parameters is required. For our VCO, these parameters are:

- $U_{\text{signal}}(t)$ (at "Freq in" input to the VCO, voltage range 0 -10 V) is sent into the VCO from Channel 1 of the arbitrary function generator and controls the shape of the RF-signal at the VCO output. From the previous scanning ODTs built in our group [Bai12, Pol17], we know that an arc-cosine signal works best to maintain the Gaussian beam shape when the scanning is turned on:

$$U_{\text{signal}}(t) = A \cdot \arccos(\omega_{\text{scan}} t) + y_0. \tag{4.12}$$

[1] Function generator RSDG 2122X by RS Pro
[2] VCO DRFA10Y-B-0-50.110 by AA Opto-Electronic

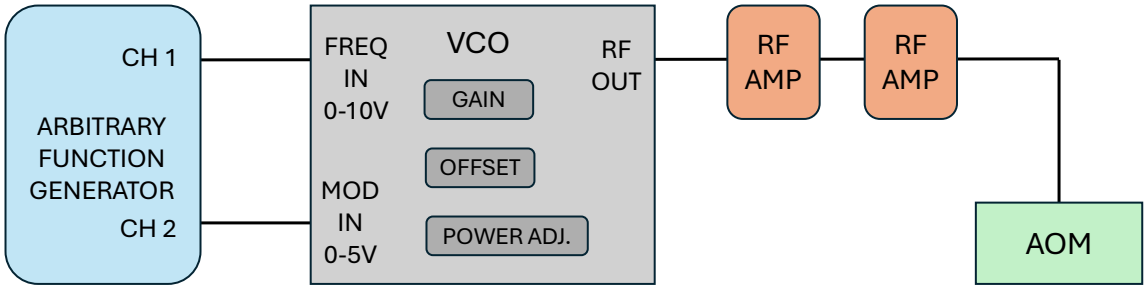

Figure 4.8.: Illustration of the electronic circuit producing the RF-signal for offline testing of the scanning ODT. The arbitrary function generator provides the input signals for the voltage-controlled oscillator (VCO) that allows us to create RF-signals with a tunable bandwidth. After passing two RF-amplifiers the signal is sent to the AOM.

With the knobs of the function generator, the offset y_0 is set to $10\,\mathrm{V}/2 = 5\,\mathrm{V}$ and the the scanning amplitude A can be tuned from $2\,\mathrm{mV}$ (no scanning) to $10\,\mathrm{V}$ (maximum scanning). Regarding the scanning frequency ω_{scan}, we observed with a spectrum analyzer that the VCO cannot follow frequencies above $200\,\mathrm{kHz}$. So, we set ω_{scan} to this value which is much larger than the maximum expected trap frequency on the order of a few hundred Hertz.

- U_{mod} (at "Mod in", voltage range 0 -5 V) changes the power of the VCO output signal. We send in a $5\,\mathrm{V}$ DC signal with Channel 2 of the function generator to maximize the power.

- Three knobs to adjust power, gain and offset of the VCO output signal. The power screw is set to the maximum. The gain changes the width of the RF-signal and the offset its position in frequency space. We optimize these two parameters by observing the VCO output signal with a spectrum analyzer. During this, we noticed that turning the gain screw multiplies the full signal from equation 4.12 with a gain factor: $G' \cdot U_{\mathrm{signal}}(t)$. Clearly, this changes the offset, so one has optimize the gain before the offset knob. We find the right gain by setting the amplitude A to maximum scanning and adjusting the gain knob so that the width of the signal is equal to the maximum bandwidth of the AOM ($30\,\mathrm{MHz}$). Now, we turn the offset knob at no scanning to reach the AOM center frequency of $80\,\mathrm{MHz}$.

Last, we optimize the power of the RF-signal by changing the gain at the amplifiers. For this we make sure that the output power of the first amplifier is just below the maximum input power of the second amplifier. Then, we connect the second amplifier in series and send the RF-signal into the AOM. After optimizing the optical coupling into the first diffraction order by aligning the laser beam as close as possible to the Bragg angle, we can optimize the gain screw of the second amplifier by observing that power in the first order decreases for too low of to high RF powers.

Figure 4.9 shows the RF-signal at the VCO output after the optimization for three different modulation amplitudes $A = 0.002\,\mathrm{V}$, $5\,\mathrm{V}$ and $10\,\mathrm{V}$. We noticed that it is possible to increase the scanning amplitude to $A = 10\,\mathrm{V}$ even though this together with the offset $y_0 = 5\,\mathrm{V}$ makes us go out of the voltage bounds 0 -10 V at VCO's Freq in channel. The scanning amplitude can not be increased even further because the maximum output voltage of the arbitrary function generator is reached. Going out of the voltage bounds at the VCO's Freq in channel causes higher frequencies to appear in the frequency spectrum in Figure 4.9(c). However, this is not a problem because the beam shape at large scanning amplitudes still looks symmetric in the scanning direction. The reason is probably that frequencies outside the bandwidth of the AOM don't have an effect on the beam shape.
Having accomplished the right RF-signal at the AOM input, we can continue looking at the optical setup and offline alignment of the scanning ODT.

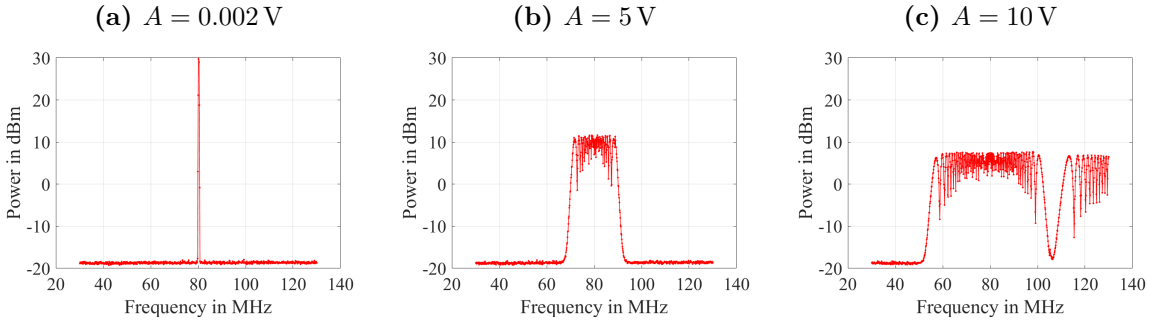

Figure 4.9.: Frequency spectrum of the VCO output for different amplitudes $A = 0.002\,\mathrm{V}$, $5\,\mathrm{V}$ and $10\,\mathrm{V}$ of the modulation signal. The offset of the modulation signal is set to $5\,\mathrm{V}$ to be at the center frequency of the AOM. Note that the RF-signal is attenuated for this measurement.

4.4. Optical Setup

The optical setup for the scanning ODT is shown schematically in Figure 4.10. All optical elements except for the last lens are placed on a $20 \times 60\,\mathrm{cm}$ breadboard which can be directly inserted into the experiment after offline testing. The lenses are made of fused silica to avoid optical aberrations due to thermal lensing. The 1064 nm light leaves the optical fiber[3] with a waist of 1.1 mm. It passes a first telescope to adjust the beam size to 0.73 mm for coupling into the AOM. After the AOM, the 0th order is dumped while the 1st order passes a telescope with $f_1 = 100\,\mathrm{mm}$ and $f_2 = 300\,\mathrm{mm}$ lenses to expand the beam diameter to 2.2 mm. The next telescope with $f_3 = -50\,\mathrm{mm}$ and $f_4 = 200\,\mathrm{mm}$ lenses increases the beam size further to 8.8 mm. Then, the beam

[3] LMA-PM-15 by NKT photonics, polarization maintaining, *MFD*= 12.6 μm at 1064 nm with collimating lens C060TMD-C by Thorlabs, $f = 9.6\,\mathrm{mm}$

leaves the breadboard at an angle of about 60 deg due to restrictions of the positioning of the breadboard with respect to the experimental chamber in the tight space on the experimental table (see figure 4.5). The last lens with $f_5 = 300\,\text{mm}$ focuses the beam onto the atoms, where we expect to reach a diameter of 36 μm (without scanning).

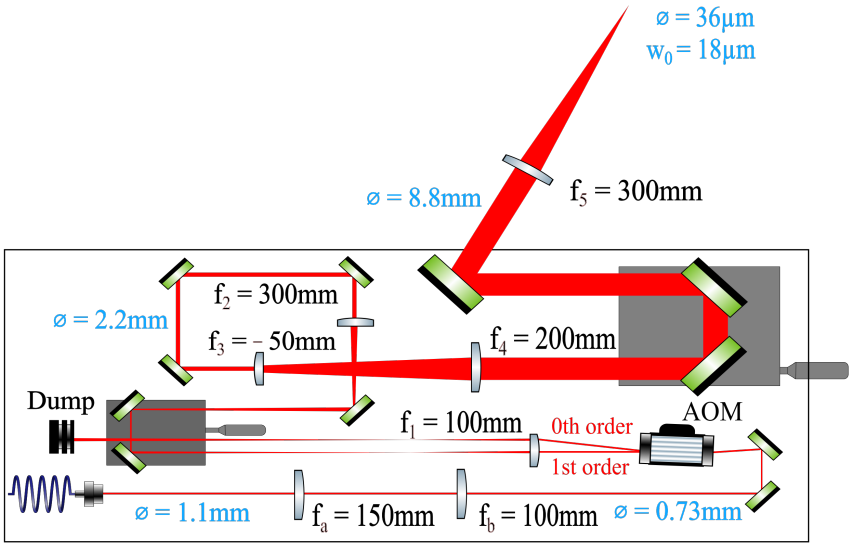

Figure 4.10.: Optical setup of the scanning optical dipole trap. All optical elements except for the last lens are placed on a breadboard (black rectangle) that can be placed directly into the experiment. Two translation stages (grey rectangles) can be used for the final alignment of the focus of the last lens onto the atoms. Where the beam is collimated as well as at the position of the atoms the beam diameter ⌀ is indicated in blue.

For a correct setup of the optical system, it is crucial to obey the right distances between the lenses. The distance between the lenses of a telescopes has to be the sum of their focal lengths:

$$\begin{aligned} d_{a,b} &= f_a + f_b = 250\,\text{mm} \\ d_{1,2} &= f_1 + f_2 = 400\,\text{mm} \\ d_{3,4} &= f_3 + f_4 = 150\,\text{mm}. \end{aligned}$$

Furthermore, the atoms should be in the Fourier plane of the AOM which fixes the distance of the AOM to the next lens and the distances between the telescopes:

$$\begin{aligned} d_{AOM,1} &= f_1 = 100\,\text{mm} \\ d_{2,3} &= f_2 + f_3 = 250\,\text{mm} \\ d_{4,5} &= f_4 + f_5 = 500\,\text{mm}. \end{aligned}$$

The small translation stage was installed to change the position of the focus of the last lens without significantly changing the beam size for final fine-tuning of the alignment onto the atoms. However, we found that the alignment of the setup is too sensitive to move this translation stage, so it was not used in the end. The large translation

stage serves to recover the right distance $d_{4,5}$ of the last lens to the rest of the optical system if the last lens is moved to align its focus onto the atoms.

4.5. Offline alignment and measurements

The alignment procedure poses several challenges, making the alignment of the scanning ODT setup one of the main challenges of the work for my master thesis. First of all, it is important to note that the 1064 nm light has a shorter Rayleigh length compared to light in the visible range, making the beam expand after a relatively short propagation distance even if it is collimated. For example, a beam with a waist of $w_0 = 1\,\text{mm}$ expands by 20% after travelling for a distance 2 m. Therefore, one should always calculate the expected beam waist along the optical path and check by measuring it with a beam profiler.
Let me also point out that the optical setup is very compact since most of the optical components are mounted on the limited space of the $20 \times 60\,\text{cm}$ breadboard. This is absolutely necessary because the breadboard fits exactly into the space in the experiment dedicated to the new scanning ODT. However, this adds some difficulties, for example, the optical path length for beam-walking with the last two mirrors before the AOM to couple into the AOM is very short.
Now, we come to the main steps of the alignment procedure which consist of preparing the beam path, coupling into the AOM and placing the lenses:

1. Preparing the beam path: We collimate the beam to a diameter of 1.1 mm with the aspherical fiber outcoupling lens and place all the mirrors as well as the first telescope. The optical path is made straight with respect to the breadboard lines so that the beam is not displaced horizontally if the translation stages are moved. Furthermore, irises are aligned along the beam path as a reference.

2. Coupling into the AOM: The AOM has then to be positioned so that the first diffraction order follows the correct beam path, i.e. is aligned with the irises. After optimizing the AOM position, we obtain a coupling efficiency of about 75% into the +1st diffraction order.

3. Placing the lenses: All lenses have to be perfectly centered on the laser beam, so that it is not deflected. Each lens is aligned with one iris at short distance, one in far distance and the camera at the final position of the atoms. With this, we can find the right height of the lens and the right horizontal position in the direction perpendicular to the optical path. The tilt of the lens around the vertical axis is eliminated by overlapping the backreflection with the incoming beam. We find the right position of the lens in the direction along the optical path by checking the beam size after the lens. In principle, the lenses should be placed in ascending order, f_1 to f_5, but after the second telescope, the beam size

is too large to check it with a beam profiler. Therefore, the lenses are placed in the following order: f_1, f_2, f_5, f_4, f_3. Note that the final beam shape at the focus is very sensitive to correct alignment of the optical setup, especially on the tilt of the last lens.

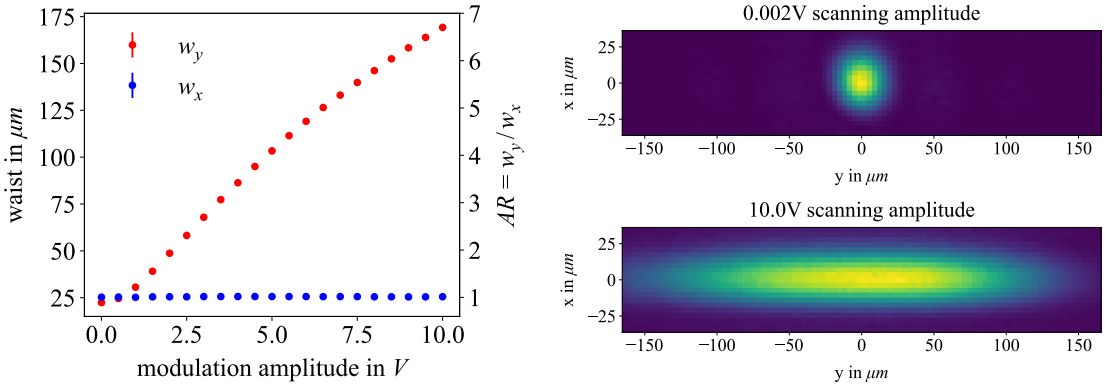

Figure 4.11.: The left plot shows the beam waist at the focus of the scanning ODT setup in the y-direction (red data points) and x-direction (blue data points) for different modulation amplitudes. The error bars obtained from a Gaussian fit to the beam profile are smaller than the data points. In the scanning direction, the waist can be tuned from $w_y = 22.38(2)\,\mu$m to $w_y = 169.3(2)\,\mu$m while the waist in the other direction stays approximately the same with $\overline{w}_x = 25.5(2)\,\mu$m. The figures on the right show the intensity profile of the beam at no scanning (0.002 V modulation amplitude) and at maximum scanning (10 V modulation amplitude).

After aligning the full setup, we use a CMOS camera[4] to measure the beam size at the focus for different modulation amplitudes A. Figure 4.11 shows the results of the waist measurement as well as the intensity profile for no scanning and maximum scanning. The waist without scanning is about $25(2)\,\mu$m, so it was not possible to reach the calculated waist of $18\,\mu$m. However, this was expected with such a tight setup and difficult alignment and nonetheless, the waist is still small enough for successful evaporative cooling to the BEC as we will see in the next section. With higher modulation amplitudes, the waist in the scanning direction increases up to $w_y = 169.3(2)\,\mu$m while the waist w_x in the perpendicular direction stays constant. At the maximum modulation amplitude, we achieve an aspect ratio of about 6.8, which is below the calculated $AR_{\max}$ of 9. Possible reasons for this are imperfections in the alignment of the setup, a smaller waist w_0 at the AOM input and the limited bandwidth of the VCO and the AOM.

[4] Blackfly-S by FLIR, pixel size $3.45\,\mu$m

4.6. Measurements with atoms

In this section, we describe the implementation of the scanning ODT into the experiment, go into the details of aligning the beam onto the atoms and characterize the scanning ODT by performing trap frequency measurements with the atomic cloud.

Implementation of the scanning ODT into the experiment

After the breadboard of the scanning ODT was placed at its intended position on the experimental table, we noticed that the beam was misaligned. The reason was that the end tip of the optical fiber is angled, so the angle of the beam leaving the fiber depends on the rotation of the fiber. Due to the delicate alignment of the setup, it was not possible to find the right rotation angle of the fiber again. Facing the fact that we had to realign the fiber outcoupling mount anyway, we used the opportunity to slightly modify the setup: We installed the fiber outcoupling mount on a breadboard below and guided the beam to the scanning ODT breadboard with a periscope. This modification has the advantages that the fiber does not have to bend so much anymore to reach the outcoupling mount and there is space in the optical path which gives the possibility to add polarization optics if needed.
To align the beam onto the atoms, we can adjust the tilt of the last three mirrors, the position of the last translation stage on the scanning ODT breadboard and the position and tilt of the last lens that is placed on a translation stage as well. Throughout the alignment procedure, we make sure that we maintain the correct beam size and shape at the position of the atoms for different scanning amplitudes. Since we cannot place a camera inside the experimental chamber, we place a flip mirror in front of the viewport, which allows us to check beam shape at the focus of the last lens with a beam profiler.
Because the one of the MOT beams and a green 532 nm beam pass through the same viewports, the scanning ODT beam has to enter at the edge of the viewport and the space before is very tight. Therefore, it is already quite challenging to let the beam pass through the experimental chamber and we have to carefully check at the viewport on the other side that the beam is not cut or deformed from reflections.
After this is achieved, we align the ODT beam onto the atoms. For this, we use standard absorption imaging at the strong blue 401 nm transition with our camera placed in the horizontal plane. The usual strategy to align an optical beam onto the atoms is to adjust the beam path until trapped atoms can be seen in the absorption image and then optimizing further to increase the atom number. If it is not possible to get any signal of the atoms to begin with, one can use a beam of resonant light as a "blow beam" by overlapping it with the actual beam and aligning to blow away atoms as efficiently as possible. We use some of the 401 nm light as a blow beam for rough alignment. Then, we optimize the atom number aligning the focus of the second ODT beam with the focus of the scanning ODT. For the second (static) ODT, we installed a new 1064 nm beam path that crosses the scanning ODT perpendicularly in the hor-

izontal plane, see figure 4.5.

Optimizing the atom number in the BEC

To increase the number of atoms in the BEC, we adjust the evaporation parameters, i.e. the power in both ODT beams and the modulation amplitude A of the scanning ODT, in each step of the evaporation sequence. To control the power, we use the leakage of one of the mirrors in each path and focus this light into a photo diode which creates the feedback signal for a PID controller. To change the modulation amplitude and therefore the aspect ratio of the scanning ODT, we adjust the amplitude of the RF-signal for the AOM. Section A.1 in the appendix explains how the electronics from the offline testing are modified to interface them with the control software of the experiment. After the optimization, we arrive at the sequence shown in figure 4.12. With 1.3×10^7 atoms in the MOT, we load 1.3×10^6 atoms into the crossed ODT and achieve 3.7×10^4 atoms in the BEC with a BEC fracion of 70%.

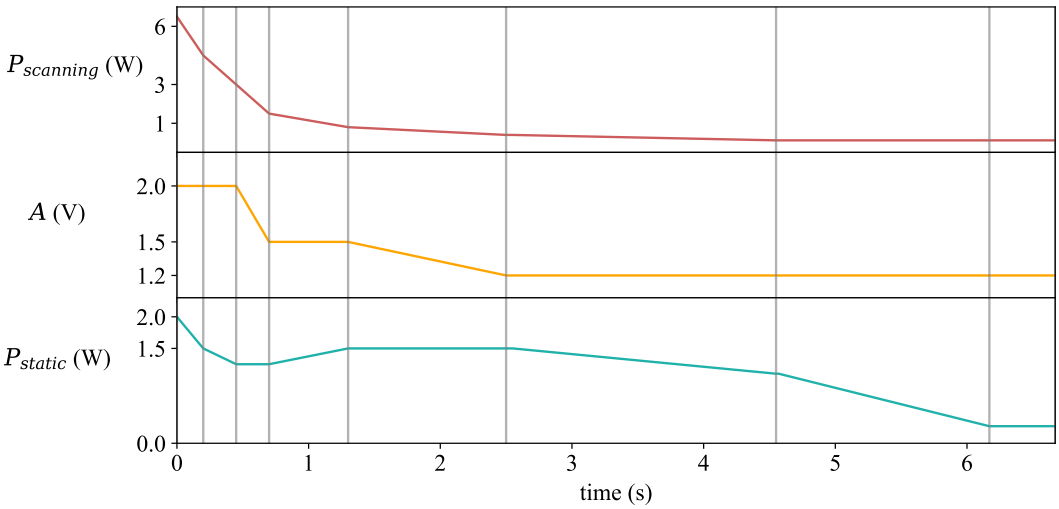

Figure 4.12.: ODT parameters during the evaporation sequence of the experiment: power $P_{scanning}$ and modulation amplitude A of the scanning ODT beam as well as power P_{static} of the static ODT beam. The evaporation sequence lasts about 6.7 s during which the modulation amplitude and the power in the ODT beams are reduced to evaporatively cool to the BEC.

Trap frequency measurements: Discussion of methods

After the scanning ODT is implemented, we want to characterize the trap by measuring the trap frequency in the direction of the scanning for different modulation amplitudes. The most common techniques to measure the trap frequencies along the different directions of the trap are parametric heating and excitation of collective oscillations of the BEC od thermal cloud.

Parametric heating technique: For this method, the trap is driven in a way to transfer kinetic energy to the atoms, typically by periodically modulating the power of the confining laser beam. For example, when the modulation frequency is twice the trap frequency, atoms are excited to higher vibrational states which causes heating and a subsequent loss of atoms [Wei98]. From the position of the loss feature in frequency space one can infer the trap frequency. In general, the parametric heating technique is typically used in situations where the trap frequencies are in the kHz regime and the limited resolution of the imaging system prevents direct observations, like in tweezers or optical lattices (in this context, the technique is rather called modulation spectroscopy).
Excitation of collective modes: Different collective modes can be excited in the atomic cloud by a sudden change of the trap parameters, such as position, width or depth of the confining potential. The change of trap parameters has to be fast enough so that the atoms can not follow adiabatically, a typical time would be one forth of the trap frequency. One can then deduce the trap frequencies by measuring the frequencies of the collective oscillation. The collective modes for a non-dipolar BEC in a spherically symmetric trap with trap frequency ω_{trap} are shown in figure 4.13(a). If the trap is suddenly displaced along one direction the dipole mode is excited, meaning that the position of the atomic cloud oscillates at the trap frequency. By temporarily changing the trap frequency along one or more directions, one can excite the so-called breathing modes where the width of the cloud oscillates. The monopole mode corresponds cycles of a ballistic expansion of the cloud due to the release from the trap, followed by a reduction in size because the atoms gain potential energy in the trap. For the quadrupole modes, the oscillation in one direction is shifted in phase by half an oscillation period. The breathing modes can be observed by switching off the trap for a short time; however, one has to consider that this can also excite the dipole mode since the cloud falls down due to gravity while the trap is off. In an anisotropic trap, an additional mode called the scissors modeshown in figure 4.13(b) can be excited by sudden rotation of the trap. Moreover, the monopole and quadrupole modes couple, see reference [Pit16] for details. It is also worth to note that sufficiently strong contact

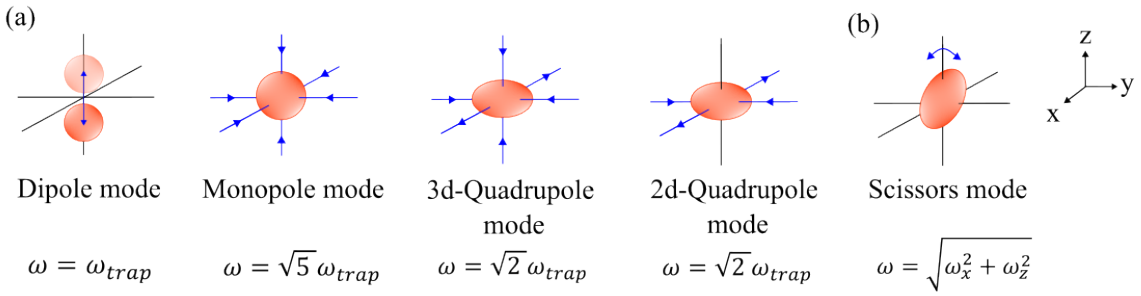

Figure 4.13.: Schematic illustration of collective modes of a non-dipolar BEC (a) in a spherically symmetric trap. (b) In an anisotropic trap, there are additional scissors modes and the other collective modes couple.

interactions as well as dipole-dipole interactions modify the oscillation frequencies of collective modes [Alt07, vB10]. However, in our measurements we only excite the dipole mode that always oscillates with the trap frequency independent of other parameters like temperature, density and interaction strength even for a dipolar BEC.
Thermal cloud vs. BEC: In principle, trap frequency measurements can be performed with the thermal cloud or with the BEC. The advantage of measuring with the thermal cloud is that the atomic density distribution follows a Gaussian profile that is more robust to fit than the BEC's density distribution which is described by a bimodal model (the sum of a Gaussian and a Thomas-Fermi profile). However, we want to characterize the final trap, so we decided to measure with the BEC. By exciting the dipole mode, a Gaussian fit is sufficient since we only need to know the position and not the width of the cloud to find the oscillation frequency.

Trap frequency measurements: Results

To excite the dipole mode, we add another step after the evaporation sequence where we displace the trap by shifting the center frequency of the RF-signal sent to the AOM[5]. After a hold time of 100 ms, the trap is displaced back to its original position and the oscillation can be observed. For this, the cloud is released from the trap and expands during 3 ms of time of flight before an absorption image is taken. We repeat this measurement for six different modulation amplitudes A. In order to keep enough atoms in the trap, we try to maintain a roughly constant trap depth by increasing the power in the scanning ODT beam for each measurement. According to equation 3.11, the trap depth is proportional to the peak intensity, $U_0 \propto I_0 \propto P/(w_{0,x}w_{0,y})$. We set for $P_{scanning}$ the value of the modulation amplitudes in Watts. Note that the value set in the control software can differ from the actual value since we can't measure the power at the position of the atoms. Figure 4.14 shows the images of the atomic cloud for $A = 1.2\,\mathrm{V}$ and $A = 10\,\mathrm{V}$ at selected times during the oscillation. The cloud is always slightly elongated vertically because of gravity. This deformation increases for higher aspect ratios because the trap gets wider in the horizontal direction. Consequently, the atoms expand more in the direction of tighter confinement during time of flight.
From the Gaussian fit, we obtain the position of the cloud. Figure 4.15 shows the positions in the horizontal (colored dots) and vertical direction (grey dots) as a function of time for the different modulation amplitudes A. From a sine fit to the position in the horizontal direction, we obtain the trap frequencies and summarize the results in table 4.2.

Table 4.2.: Measured trap frequencies ω_y for different modulation amplitudes of the scanning ODT beam.

A in V	1.2	2.4	4.8	6.0	8.0	10.0
$\omega_y/2\pi$ in Hz	207.8(6)	203.3(6)	105(1)	84(1)	68(2)	64(3)

[5] We change U_{offset} in equation A.1 from the initial 5 V to 4.7 V for 0.01 ms

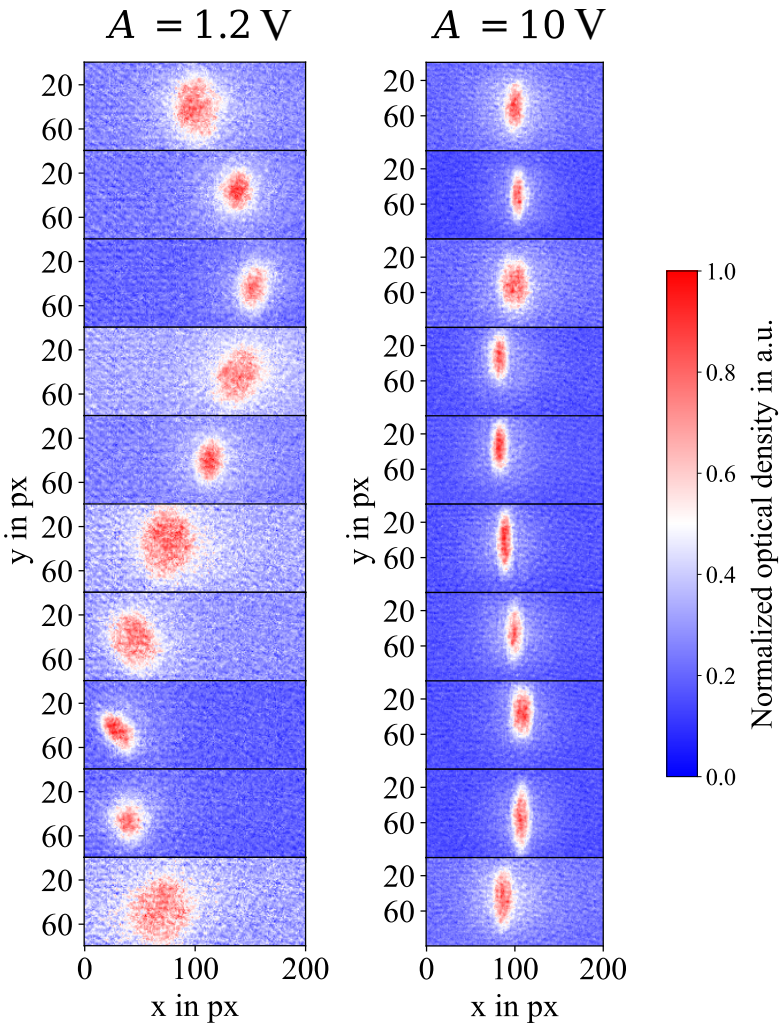

Figure 4.14.: The atomic cloud during dipole oscillation for modulation amplitudes of $A = 1.2\,\mathrm{V}$ and $A = 10\,\mathrm{V}$. The absorption images are shown for the time interval of 0 to 5 ms with a time step of 0.5 ms.

From the trap frequency measurement, we can conclude that that the trap frequency in the scanning direction can be tuned from $\omega_y = 2\pi \times 203.3(6)\,\mathrm{Hz}$ ($A = 1.2\,\mathrm{V}$, $P_{\mathrm{scanning}} = 1.2\,\mathrm{W}$) to $\omega_y = 2\pi \times 64(3)\,\mathrm{Hz}$ ($A = 10\,\mathrm{V}$, $P_{\mathrm{scanning}} = 10\,\mathrm{W}$). However, we think that the power can actually not be increased sufficiently to the set values in order to keep a constant trap depth, which affects the trap frequencies in both directions according to equation 3.12. Therefore, further measurements are needed to characterize the trap, specifically, determining the trap frequencies in both the scanning and non-scanning direction to measure the aspect ratio.

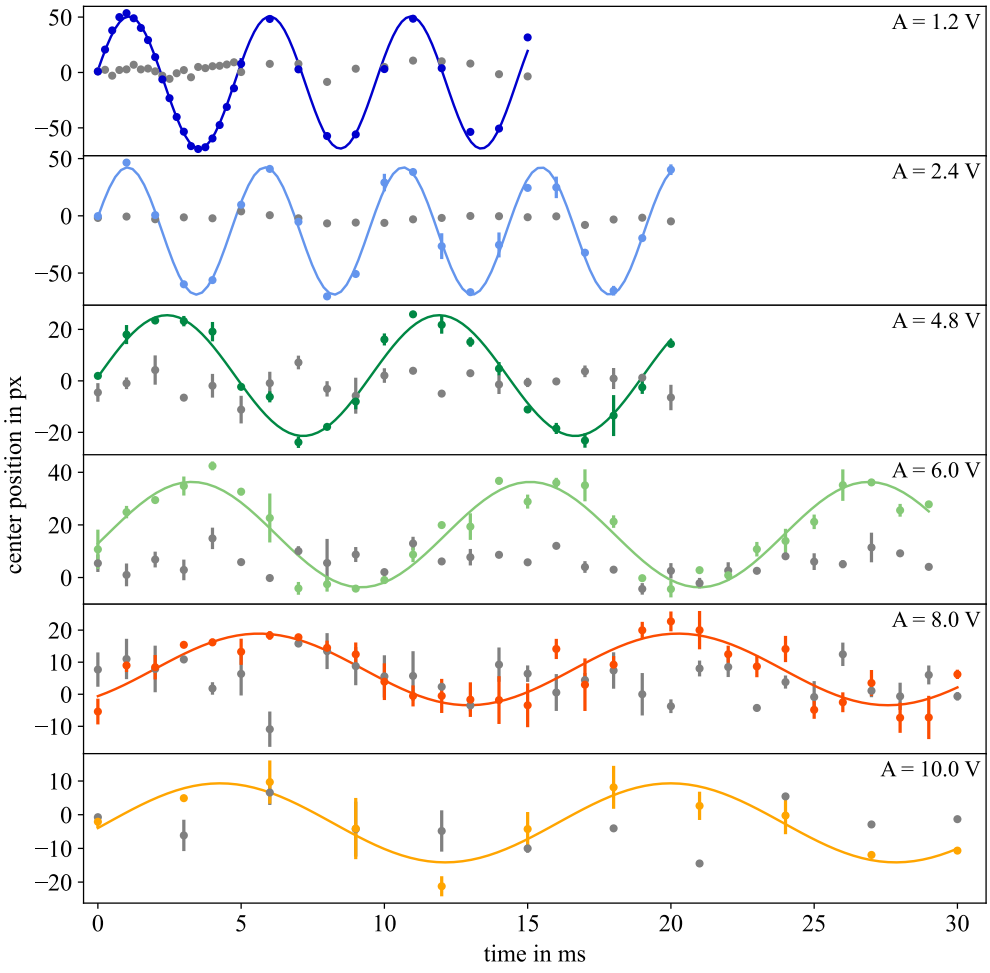

Figure 4.15.: Center position of the atomic cloud in the horizontal direction (colored data points) and in the vertical direction (grey data points) for different modulation amplitudes A as a function of time after a displacement of the scanning ODT beam in the horizontal direction. The position of the cloud is determined with a Gaussian fit to the absorption images that were taken after time of flight. The error bars denote the standard deviation obtained from the average over three measurements. The solid lines show a fit with a sine model $y = B\sin(\omega \cdot (t - t_0)) + y_0$.

Chapter 5

Optical potentials for ultracold erbium atoms using q-plates

In this chapter, we review the basics of representing polarization states of light, explain the composition and working principle of q-plates and demonstrate how the polarization profile of a q-plate beam can be measured with projections onto the polarization basis states. From the intensity and polarization profile of a q-plate beam, we calculate the optical dipole potential it creates for erbium atoms. Last, we discuss possible challenges for the implementation of q-plates alternative methods to create vector beams with spatial light modulators.

5.1. Q-plate basics

To understand the working principle of q-plates, we first need to describe the framework that we use to represent vector beams, i.e. light fields with non-uniform polarization. For this, we mainly rely on reference [Car15]. We begin by introducing the Jones formalism to describe the light's polarization. Next, we find the Jones matrix for a general waveplate and use this result to study the creation and propagation of vector beams: In the far-field, q-plate beams can be described with Laguerre-Gaussian modes, but to predict the propagation through optical systems more accurately, the circular beam model is needed. Next, we look at more technical aspects about the composition and manufacturing of q-plates. We also discuss the Stokes parameters and polarization ellipse as tools for measuring and visualizing polarization patterns of vector beams.

5.1.1. Jones formalism and polarization basis

Within the paraxial approximation that requires small angles between the light rays and the optical axis, the electric field $\vec{\mathcal{E}}$ of a plane wave traveling in the z-direction only oscillates in the transverse x-y-plane:

$$\vec{\mathcal{E}}(z,t) = \begin{pmatrix} E_x e^{i\phi_x} \\ E_y e^{i\phi_y} \end{pmatrix} e^{i(\omega t - kz)}. \tag{5.1}$$

Here, ω is the circular frequency and k is the wavenumber. The electric field strengths E_x, E_y and phases ϕ_x, ϕ_y in the x- and y-direction define the polarization of the light. We can write the polarization vector, which is also called the *Jones vector*, in terms of the complex-valued components $c_x = E_x e^{i\phi_x}$ and $c_y = E_y e^{i\phi_y}$:

$$\vec{E} = \begin{pmatrix} c_x \\ c_y \end{pmatrix}. \tag{5.2}$$

The intensity of the light is given by $|\vec{E}|^2 = |c_x|^2 + |c_y|^2$ and is typically normalized to 1. As for any vector, the Jones vector has to be given with respect to a certain basis. Let's choose the basis of horizontal and vertical linear polarization (labeled as $|H\rangle$ and $|V\rangle$ in the bra-ket notation) to be along the basis vectors of our coordinate system:

$$|H\rangle = \hat{\mathbf{e}}_x, \qquad |V\rangle = \hat{\mathbf{e}}_y. \tag{5.3}$$

Therefore, $c_{h(v)} = c_{x(y)}$ and the polarization vector $|E_{(h,v)}\rangle$ in the $|H\rangle, |V\rangle$ basis reads

$$|E_{(h,v)}\rangle = c_\mathrm{h} |H\rangle + c_\mathrm{v} |V\rangle. \tag{5.4}$$

Apart from horizontal and vertical polarization, other examples for a choice of basis are diagonal and anti-diagonal polarization ($|D\rangle$, $|A\rangle$) as well as left- and right handed circular polarization ($|L\rangle$, $|R\rangle$). The diagonal and anti-diagonal states arise when the $|H\rangle, |V\rangle$ basis is rotated by $\pi/4$; the left (right) circular states are given by the addition of the $|H\rangle, |V\rangle$ states with a $\pi/2$ ($-\pi/2$) phase difference (see first column in table 5.1).
While the $|H\rangle, |V\rangle$ basis is typically used for expressing Jones vectors, the action of a q-plate is described in the $|L\rangle$, $|R\rangle$ basis. Therefore, it will be necessary the switch between the two bases by multiplying with the unitary matrix $\hat{U}$

$$\vec{E}_{(l,r)} = \hat{U} \cdot \vec{E}_{(h,v)}, \qquad \hat{U} = \frac{1}{\sqrt{2}} \begin{pmatrix} 1 & -i \\ 1 & i \end{pmatrix}. \tag{5.5}$$

Note that the subscripts (h,v) and (l,r) refer to a representation in the corresponding $|H\rangle, |V\rangle$ and $|L\rangle$, $|R\rangle$ basis. The Jones representation of all important polarization states in both the $|H\rangle$, $|V\rangle$ basis and the $|L\rangle$, $|R\rangle$ basis is shown in Table 5.1.

Table 5.1.: Jones vectors of the horizontal, vertical, left circular, right circular, diagonal and anti-diagonal polarization states, expressed both in the horizontal/vertical and left/right circular basis.

Polarization State	Vector in $\|H\rangle$, $\|V\rangle$ basis	Vector in $\|L\rangle$, $\|R\rangle$ basis
$\|H\rangle$	$\begin{pmatrix}1\\0\end{pmatrix}$	$\frac{1}{\sqrt{2}}\begin{pmatrix}1\\1\end{pmatrix}$
$\|V\rangle$	$\begin{pmatrix}0\\1\end{pmatrix}$	$\frac{1}{\sqrt{2}}\begin{pmatrix}-i\\i\end{pmatrix}$
$\|L\rangle = \frac{1}{\sqrt{2}}(\|H\rangle + i\,\|V\rangle)$	$\frac{1}{\sqrt{2}}\begin{pmatrix}1\\i\end{pmatrix}$	$\begin{pmatrix}1\\0\end{pmatrix}$
$\|R\rangle = \frac{1}{\sqrt{2}}(\|H\rangle - i\,\|V\rangle)$	$\frac{1}{\sqrt{2}}\begin{pmatrix}1\\-i\end{pmatrix}$	$\begin{pmatrix}0\\1\end{pmatrix}$
$\|D\rangle = \frac{1}{\sqrt{2}}(\|H\rangle + \|V\rangle)$	$\frac{1}{\sqrt{2}}\begin{pmatrix}1\\1\end{pmatrix}$	$\frac{1}{2}\begin{pmatrix}1-i\\1+i\end{pmatrix}$
$\|A\rangle = \frac{1}{\sqrt{2}}(\|H\rangle - \|V\rangle)$	$\frac{1}{\sqrt{2}}\begin{pmatrix}1\\-1\end{pmatrix}$	$\frac{1}{2}\begin{pmatrix}1+i\\1-1\end{pmatrix}$

5.1.2. Optical elements and Jones matrices

In the Jones formalism, the action of optical elements on the polarization state is described by the multiplication with a 2×2 Jones matrix $\hat{M}$. For example, in the $|H\rangle$, $|V\rangle$ basis

$$\vec{E}_{out,(h,v)} = \hat{M}_{(h,v)} \cdot \vec{E}_{in,(h,v)} \tag{5.6}$$

and the Jones matrix transforms into the $|L\rangle$, $|R\rangle$ basis as

$$\hat{M}_{(l,r)} = \hat{U} \cdot \hat{M}_{(h,v)} \cdot \hat{U}^{\dagger} \tag{5.7}$$

with the unitary matrix defined in equation 5.5.
A common way to alter the polarization of light are waveplates, optical elements that consist of a birefringent medium. Birefringent media are characterized by two directions: A "slow" axis with index of refraction n_s and a "fast" axis with index of refraction n_f. The light polarized parallel to the slow axis experiences a higher refractive index $n_s > n_f$ and travels slower than the light polarized parallel to the fast axis. Consequently, a waveplate with thickness d introduces a phase delay δ between the light components traveling along the two axes:

$$\delta = 2\pi \frac{d(n_s - n_f)}{\lambda} \tag{5.8}$$

Note that for the well-known examples of half-waveplates (HWP) and quarter-waveplates (QWP), the material and thickness of the plates are chosen so that the phase shifts

are $\delta = \pi$ and $\delta = \pi/2$.
The Jones matrix for the action of a waveplate with arbitrary δ in the basis of the fast and slow axes $\{\hat{\mathbf{e}}_\mathbf{f},\ \hat{\mathbf{e}}_\mathbf{s}\}$ is

$$\widehat{WP}_{(f,s)} = \begin{pmatrix} e^{-i\delta/2} & 0 \\ 0 & e^{i\delta/2} \end{pmatrix}. \tag{5.9}$$

The $|H\rangle = \hat{\mathbf{e}}_x$, $|V\rangle = \hat{\mathbf{e}}_y$ basis can be rotated with respect to to the $\hat{\mathbf{e}}_f$, $\hat{\mathbf{e}}_s$ basis by an angle θ. For this, we need to define the rotation matrix $\hat{R}(\theta)$:

$$\hat{R}(\theta) = \begin{pmatrix} \cos(\theta) & -\sin(\theta) \\ \sin(\theta) & \cos(\theta) \end{pmatrix}. \tag{5.10}$$

To describe the action of the waveplate in the $|H\rangle$, $|V\rangle$ basis, we first have to rotate by $-\theta$, then we can apply the Jones matrix of the waveplate in the $\{\hat{\mathbf{e}}_\mathbf{f},\ \hat{\mathbf{e}}_\mathbf{s}\}$ basis and rotate back by θ:

$$\widehat{WP}_{(h,v)} = \hat{R}(\theta) \cdot \widehat{WP}_{(f,s)} \cdot \hat{R}(-\theta) \tag{5.11}$$

Finally, we transform the Jones matrix of a general waveplate into the $|L\rangle$, $|R\rangle$ basis with equation 5.7:

$$\widehat{WP}_{(l,r)} = \hat{U} \cdot \widehat{WP}_{(h,v)} \cdot \hat{U}^\dagger = \begin{pmatrix} \cos(\delta/2) & i\sin(\delta/2)e^{-2i\theta} \\ i\sin(\delta/2)e^{2i\theta} & \cos(\delta/2) \end{pmatrix} \tag{5.12}$$

Considering again the examples of a half-waveplate and a quarter-waveplate, the corresponding Jones matrices according to equations 5.11 and 5.12 are shown in Table 5.2. For incoming linear polarization, a half-waveplate only rotates the polarization vector while a quarter-waveplate converts it into elliptical polarization.

Table 5.2.: Jones matrices of a half-waveplate and a quarter-waveplate rotated by an angle θ, represented in the $|H\rangle$, $|V\rangle$ and the $|L\rangle$, $|R\rangle$ basis.

Optical element	Matrix in $\|H\rangle$, $\|V\rangle$ basis	Matrix in $\|L\rangle$, $\|R\rangle$ basis
HWP	$-i\begin{pmatrix} \cos 2\theta & \sin 2\theta \\ \sin 2\theta & -\cos 2\theta \end{pmatrix}$	$\begin{pmatrix} 0 & ie^{-2i\theta} \\ ie^{2i\theta} & 0 \end{pmatrix}$
QWP	$\frac{1}{\sqrt{2}}\begin{pmatrix} 1-i\cos 2\theta & -i\sin 2\theta \\ -i\sin 2\theta & 1+i\cos 2\theta \end{pmatrix}$	$\frac{1}{\sqrt{2}}\begin{pmatrix} 1 & ie^{-2i\theta} \\ ie^{2i\theta} & 1 \end{pmatrix}$

5.1.3. Generating Vector beams with Q-plates

So far, we have only considered examples of spatially uniform waveplates like half-waveplates and quarter-waveplates that cause a constant phase retardation across the

beam profile. For general waveplates, the imprinted phase does not have to be spatially uniform. This means that in any polarization basis (ν, μ) the electric field components of the outgoing electric field can vary spatially. Such beams are called *vector beams* [Car15]. They have the general form

$$\vec{E}_{(\nu,\mu)}(r,\phi,z) = \begin{pmatrix} c_\nu \cdot A_\nu(r,\phi) \\ c_\mu \cdot A_\mu(r,\phi) \end{pmatrix} \tag{5.13}$$

with different complex-valued electric field components $A_\nu(r,\phi) \neq A_\mu(r,\phi)$ and cylindrical coordinates (r,ϕ,z).
A spatially non-uniform phase delay can be achieved by using liquid crystal (LC) molecules as the birefringent medium in a waveplate: The local orientation of the molecules defines the direction of the fast and slow axis and therefore the local phase shift for the light. In principle, one can imprint arbitrary LC patterns where the only restriction is the resolution limit of the printing technique. We will now focus on a specific type of general waveplates, called *q-plates*, that were invented in Naples in 2006 [Rub19]. For q-plates, the imprinted phase only depends on the azimuthal angle ϕ that goes around the center of the plate. The orientation θ of the LC molecules follows

$$\theta(\phi) = q \cdot \phi + \theta_0. \tag{5.14}$$

The order q of the q-plate describes how many times the orientation of the LC molecules completes one full rotation of 2π around the center of the plate. The parameter θ_0 sets the initial orientation of the molecules at $\phi = 0$ and will be set to zero for simplicity from now on. Figure 5.1 illustrates the LC pattern for q-plates of different orders and $\theta_0 = 0$.

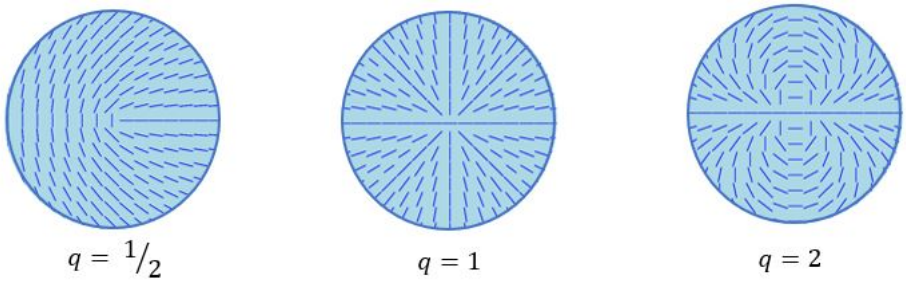

Figure 5.1.: Liquid crystal pattern for q-plates of order $q = 1/2$, $q = 1$ and $q = 2$ with $\theta_0 = 0$.

Let us now study the effect of a q-plate on light. For this, we take the Jones vector of the incoming light in the left/right circular polarization basis

$$\vec{E}_{in,(l,r)} = \begin{pmatrix} c_L \\ c_R \end{pmatrix}. \tag{5.15}$$

Then, we insert the angle dependence of the LC orientation, equation 5.14, into the Jones matrix of a general waveplate, equation 5.12, to find the outgoing electric field

$$\vec{E}_{out,(l,r)}(r,\phi) = \widehat{WP}_{(l,r)} \cdot \vec{E}_{in,(l,r)} = \cos(\delta/2) \begin{pmatrix} c_L \\ c_R \end{pmatrix} + i \sin(\delta/2) \begin{pmatrix} e^{-2iq\phi} & c_R \\ e^{2iq\phi} & c_L \end{pmatrix} \tag{5.16}$$

From the ϕ-dependence in each field component, we can already see that q-plates can create vector beams. Let us now take a closer look at the electric field created by a q-plate. We can see that for a phase delay of $\delta = \pi$, the q-plate completely converts right circular polarization to left circular polarization (and vice-versa) with an additional azimuthal phase winding $\exp(\pm 2iq\phi)$[1]:

$$\vec{E}_{in,(l,r)} = \begin{pmatrix} 0 \\ 1 \end{pmatrix} \quad \rightarrow \quad \vec{E}_{out,(l,r)} = \begin{pmatrix} ie^{-2iq\phi} \\ 0 \end{pmatrix} \tag{5.17}$$

$$\vec{E}_{in,(l,r)} = \begin{pmatrix} 1 \\ 0 \end{pmatrix} \quad \rightarrow \quad \vec{E}_{out,(l,r)} = \begin{pmatrix} 0 \\ ie^{2iq\phi} \end{pmatrix} \tag{5.18}$$

This effect is illustrated in figure 5.2 for a $q = 1$: The incoming beam is purely right (left) circularly polarized and has a Gaussian intensity profile. The outgoing beam is fully left (right) circular polarized and the phase winding causes a so-called helical phase front. Because the phase is undefined in the beam's center, the intensity has to be zero here. From a topological point of view, the phase winding creates a topological vortex with integer charge $l = 2q$ (see [Car15] for details).

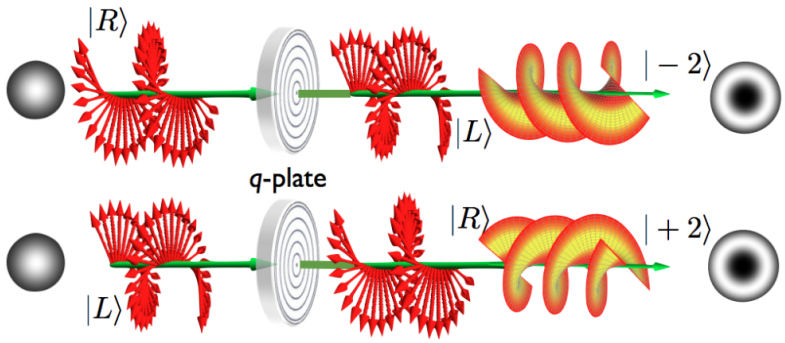

Figure 5.2.: Schematic illustration of the effect of a q-plate on light. An incoming beam with Gaussian intensity profile and right (left) circular polarization enters a q-plate with $q = 1$. For a phase delay of $\delta = \pi$, it is fully converted into left (right) polarized light with a helical phase front. The intensity profile is given by Laguerre-Gaussian modes with radial index $p = 0$ and azimuthal index $l = \pm 2q$. Figure taken from [Car15].

Next, we need to find a description for the intensity profile for beams created by q-plates. Because of their "doughnut-shape", it seems reasonable to use Laguerre-Gaussian (LG) modes which is in fact a good approximation in the far-field. Therefore, we introduce the LG model in the next section. The following section covers the more sophisticated description in terms of the so-called circular-beam model [Val16]. It relies on hypergeometric Gaussian modes and predicts the propagation though optical systems more accurately than the LG beam model.

[1] Note that for brevity, we omit writing the spatial dependence of $\vec{E}_{out,(l,r)}$ on (r, ϕ) from now on.

5.1.4. Description in the far-field: Laguerre-Gaussian model

Laguerre-Gaussian beams are well-known solutions of the paraxial Helmholtz equation. They are rotationally symmetric around the direction of propagation and are defined by two indices: p, the radial index, and l, the azimuthal index. Figure 5.3 illustrates the intensity and phase profile for the first few LG modes. The full mathematical

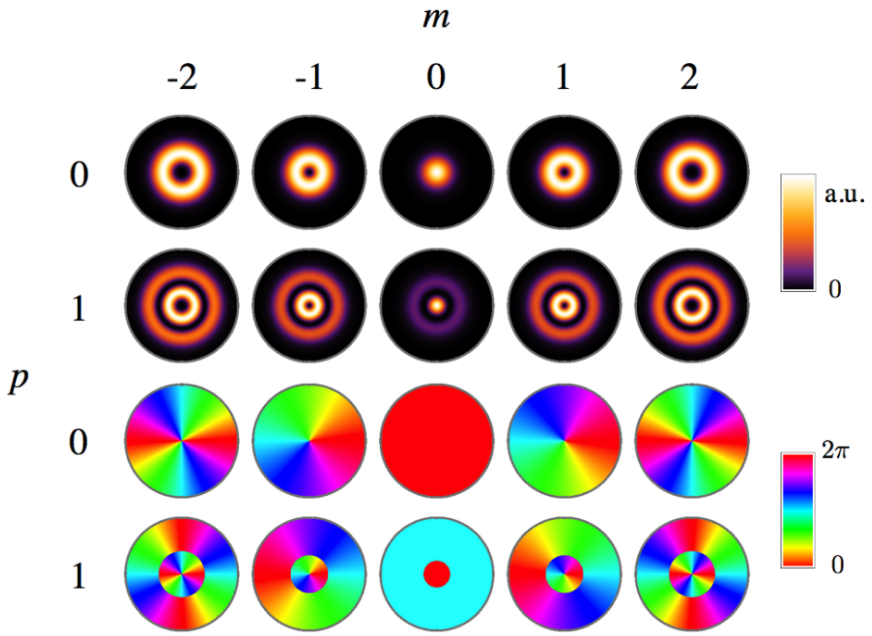

Figure 5.3.: Intensity (top) and phase (bottom) profile of the first few Laguerre-Gaussian modes that are defined by p, the radial index, and $l = m$, the azimuthal index. Taken from [Car15].

expression of LG modes can be found in equation 1.42 of [Car15]. Here we consider a collimated LG mode: $z \ll z_R$, where $z_R = \pi w_0^2/\lambda$ is the Rayleigh length. LG mode have a jump in their phase profile in the radial direction for $p > 0$. Since q-plates only impact the phase in the azimuthal direction, we can set $p = 0$ always. Therefore, the expression of LG modes created by q-plates becomes

$$LG_{p=0,l}(r,\phi) = \sqrt{\frac{2^{|l|+1}}{\pi\, w_0^2\, |l|!}} \left(\frac{r}{w_0}\right)^{|l|} e^{-\frac{r^2}{w_0^2}}\, L_0^{|l|}\left(\frac{2r^2}{w_0^2}\right)\, e^{il\phi} \tag{5.19}$$

where w_0 is the waist and $L_0^{|l|}(x)$ are the generalized Laguerre polynomials. We can now adjust equations 5.15 5.16 to include the LG modes into the description of the q-plate action. The incoming Gaussian beam can be expressed as a $LG_{0,0}$ mode:

$$\vec{E}_{in,(l,r)} = \begin{pmatrix} c_L\, LG_{0,0}(r,\phi) \\ c_R\, LG_{0,0}(r,\phi) \end{pmatrix} \tag{5.20}$$

and the outgoing beam becomes

$$\vec{E}_{out,(l,r)} = \cos(\delta/2)\begin{pmatrix} c_L\ LG_{0,0}(r,\phi) \\ c_R\ LG_{0,0}(r,\phi)\end{pmatrix} + i\sin(\delta/2)\begin{pmatrix} c_R\ LG_{0,-2q}(r,\phi) \\ c_L\ LG_{0,2q}(r,\phi)\end{pmatrix}. \tag{5.21}$$

5.1.5. Propagation through an optical system: Circular beam model

In the circular beam (CiB) model [Val16], the beam created by a q-plate is described by a function $CiB^{(q_0,\xi)}_{-|l|,l}$ that depends on the complex parameters q_0 and ξ. The parameter q_0 is defined as

$$q_0 = -d_0 + iz_0. \tag{5.22}$$

Here, z_0 is related to the size of the beam: $z_0 = kw_0^2/2$, with w_0 the analog of the Gaussian beam waist, and d_0 is the position of the waist. The second parameter ξ determines the "class" of the CiB. For example, cylindrical beams become LG modes in the limit of $\xi \to \pm\infty$ and for q-plate beams, $|\xi| = 1$ holds. With given beam parameters q_0 and ξ and a fixed transverse plane, a cylindrical beam has the form

$$CiB^{(q_0,\xi)}_{-|l|,l} = \frac{\Gamma(|l|/2+1)}{|l|!}\left(\frac{-r^2}{\xi\chi^2}\right)^{|l|/2} G(r)\ {}_1F_1\left(\frac{|l|}{2}, |l|+1, \frac{r^2}{\chi^2}\right) e^{il\phi} \quad \text{with} |\xi| = 1. \tag{5.23}$$

Here, we have defined the auxiliary function χ and the Gaussian mode $G(r)$

$$G(r) = \frac{i}{q_0}\sqrt{\frac{kz_0}{\pi}} e^{-\frac{ikr^2}{2q_0}}, \quad \frac{1}{\chi^2} = \frac{kz_0\xi}{q_0}\frac{1}{q_0+\xi q_0^*}, \quad z_0 = \mathfrak{Im}\left[q_0\right].$$

The Gamma function $\Gamma(x)$ and the confluent hypergeometric function ${}_1F_1(a,b,x)$ can be implemented easily e.g. in Python with *math.gamma()* and *scipy.special.hyp1f1*. Let us now describe the propagation of a circular beam through an optical system. For this, we start at the q-plate with

$$q_0 = iz_0 \quad \text{and} \quad \xi = 1. \tag{5.24}$$

As the beam propagates, the evolution can be described in terms of the $ABCD$ method in the paraxial regime. In the $ABCD$ model, each section of the optical system that the beam passes through corresponds to a matrix M_{ABCD} that transforms the beam parameters:

$$M_{ABCD} = \begin{pmatrix} A & B \\ C & D\end{pmatrix}, \qquad q_0 \to \frac{Aq_0+B}{Cq_0+D}, \quad \xi \to \frac{Cq_0^*+D}{Cq_0^*+D}\xi \tag{5.25}$$

The propagation of a CiB is simulated by consecutive transformation of the beam parameters according to the $ABCD$ matrices that describe the optical system. Note that the absolute value of ξ stays constant ($|\xi| = 1$) throughout propagation which

ensures that the beam stays in the same class of CiBs and can be described with equation 5.23. The $ABCD$ matrices for different parts in the optical path are well-known from geometric optics. For us, the cases of propagating through free space over a distance d and passing a lens with focal length f are important:

$$M_{freespace} = \begin{pmatrix} 1 & d \\ 0 & 1 \end{pmatrix}, \qquad M_{lens} = \begin{pmatrix} 0 & 1 \\ -1/f & 1 \end{pmatrix}. \tag{5.26}$$

The resulting beam from a q-plate in the CiB model for a given beam parameters (q_0, ξ) is then

$$\vec{E}_{out,(l,r)} = \cos(\delta/2) \begin{pmatrix} c_L \; CiB_{0,0}^{(q_0,\xi)}(r,\phi) \\ c_R \; CiB_{0,0}^{(q_0,\xi)}(r,\phi) \end{pmatrix} + i \sin(\delta/2) \begin{pmatrix} c_R \; CiB_{2q,-2q}^{(q_0,\xi)}(r,\phi) \\ c_L \; CiB_{2q,2q}^{(q_0,\xi)}(r,\phi) \end{pmatrix}. \tag{5.27}$$

Model comparison

Reference [Val16] compares the circular beam model with experimental observations. The authors use a circularly polarized Gaussian beam with a waist of 890 μm and a wavelength of 810 nm. They place a q-plate with $q = 1/2$ at the beam waist location at 0 mm and compare the experimentally observed free-space propagation with the CiB model and a Laguerre-Gauss model. Figure 5.4 shows the results for different propagation distances d after the q-plate. Clearly, the CiB model (second row) agrees much better with the experimental observation (first row) than the LG model (third row) in the near-field ($d \lesssim z_0/10$). In the far-field, the LG mode matches the observed vortex beam and the CiB model in good approximation.

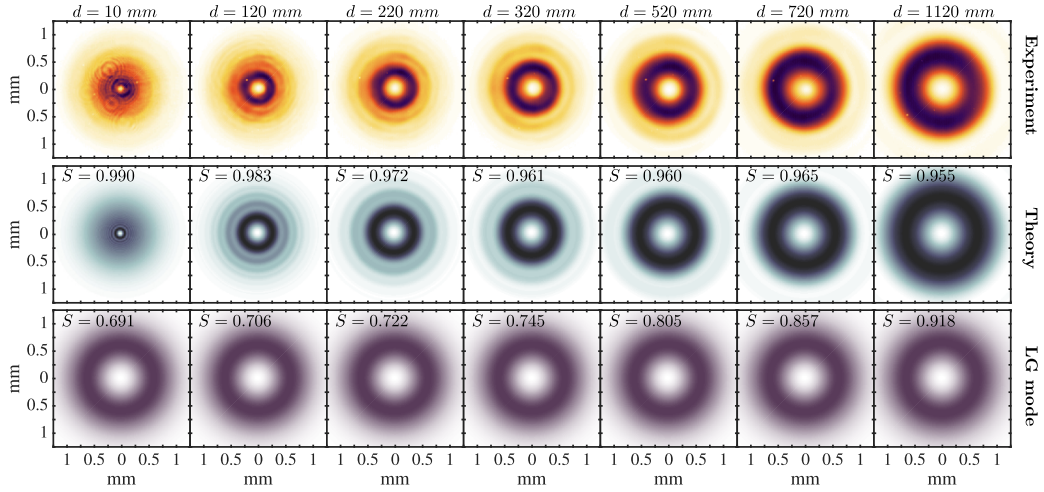

Figure 5.4.: Intensity distribution of a optical vortex beam created by a q-plate at $d = 0$ mm with an initial Gaussian beam waist of 810 nm. The three rows show the experimental observation and the prediction by the CiB and the LG model for different propagation distances d. The similarity parameter S indicates the agreement of each model with the experiment. Figure taken from [Val16].

5.1.6. Composition and fabrication of q-plates

Q-plates are about 2x2 cm in size and consist of two glass plates with an azo-dye and a liquid crystal (LC) layer in between, as one can see in figure 5.5(a). The azo-dye is

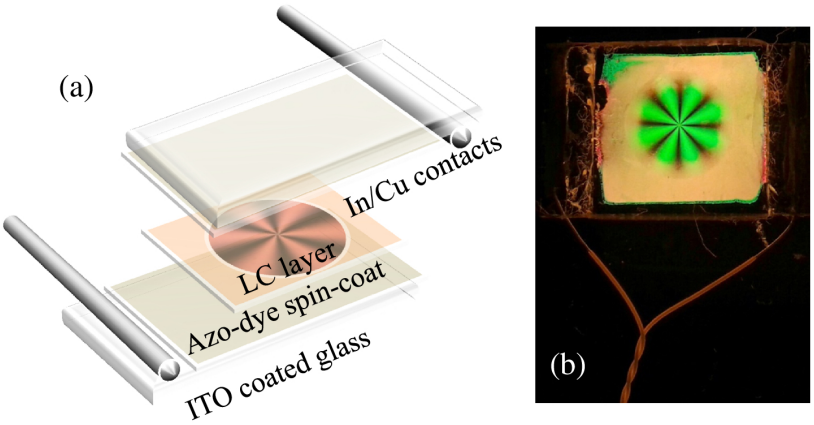

Figure 5.5.: (a) Schematic illustration of the composition of a q-plate. The glass plates are coated with the transparent conductor indium-tin oxide (ITO) and connected to electrical contacts. An azo-dye layer allows for printing patterns into the LC layer thanks to the photo-alignment technique. (b) Picture of a q-plate that is placed between to crossed polarizers. Figure taken from [Rub19].

used to imprint the desired q-plate pattern with a photo-alignment technique [Rub19]. For wavelengths in the blue or near-UV, the azo-dye molecules align perpendicular to the polarization of the light. The LC molecules then align with the dye molecules. For applications of q-plates, wavelengths of about 600 nm and below have to be carefully tested since they are likely to damage the q-plate pattern by reorienting the azo-dye molecules.
Furthermore, a wire is attached to each of the glass plates that are coated with the transparent conductor ITO so that an electrical voltage can be applied between them. This allows for controlling the angle of the LC molecules in the direction along the propagation of the light, changing the phase delay δ and therefore tuning the amount of conversion to light of opposite handedness in equation 5.21. To ensure that no static electric charges build up, the voltage signal ranging from 0 V to a few volts has to be alternating (AC) with a frequency of a few kHz.
The manufacturing of q-plates requires advanced fabrication techniques [Rub19]. Microspacers in between the glass plates create uniform thickness of the LC layer to ensure a uniform phase delay δ, see equation 5.8. All materials and devices are carefully cleaned before the manufacturing process. Nevertheless, there can be imperfections in the fabrication materials or in the imprinting process that can cause imperfections in the LC pattern. Unavoidably, q-plates have a defect in the center where the orientation of the LC molecules is undefined. The defect becomes larger for higher orders of the q-plate. After manufacturing, q-plates can be quality-controlled by placing it

between two crossed polarizers and observing the LC pattern, as it can be seen in figure 5.5(b).

5.2. Measuring polarization patterns

While the intensity profile of a light beam can be easily measured with a camera, reconstructing the polarization pattern is more complicated. One possibility is to measure the Stokes parameters which are given by the components of the Jones vectors represented in different bases:

$$\begin{aligned} S_1 &= |c_h|^2 - |c_v|^2 \\ S_2 &= |c_d|^2 - |c_a|^2 \\ S_3 &= |c_l|^2 - |c_r|^2 \end{aligned} \tag{5.28}$$

Here, $(h,\, v)$, $(d,\, a)$ and $(l,\, r)$ correspond to the different polarization bases shown in table 5.1. Experimentally, this means that the Stokes parameters at each point of a beam can be found by projecting into the different polarization states n and measuring the corresponding intensities I_n:

$$\begin{aligned} S_1 &= I_h - I_v \\ S_2 &= I_d - I_a \\ S_3 &= I_l - I_r \end{aligned} \tag{5.29}$$

A given set of Stokes parameters corresponds to a point on the Poincaré sphere, similar to a qubit state on the Bloch sphere [Car15]. Figure 5.6(a) shows the principle of representing a polarization state as a point $(S_1,\, S_2,\, S_3)$ on the Poincaré sphere. Here, we always assume fully polarized light so that $\sqrt{S_1^2 + S_2^2 + S_3^2} = 1$. In polar coordinates, the point on the sphere is defined by two angles Φ and χ:

$$\begin{aligned} S_1 &= \cos(2\chi)\cos(2\psi) \\ S_2 &= \cos(2\chi)\sin(2\psi) \\ S_3 &= \sin(2\chi). \end{aligned} \tag{5.30}$$

Sometimes it is more useful to use these angles to visualize the polarization as a polarization ellipse. As illustrated in figure 5.6(b), Φ gives the orientation of the ellipse and χ defines its ellipticity. From equations 5.30 it follows that the angles Φ ans χ are related to the Stokes parameters S_1, S_2, S_3 via

$$\begin{aligned} \tan(2\psi) &= \frac{S_2}{S_1} \\ \tan(2\chi) &= \frac{S_3}{\sqrt{S_1^2 + S_2^2}}. \end{aligned} \tag{5.31}$$

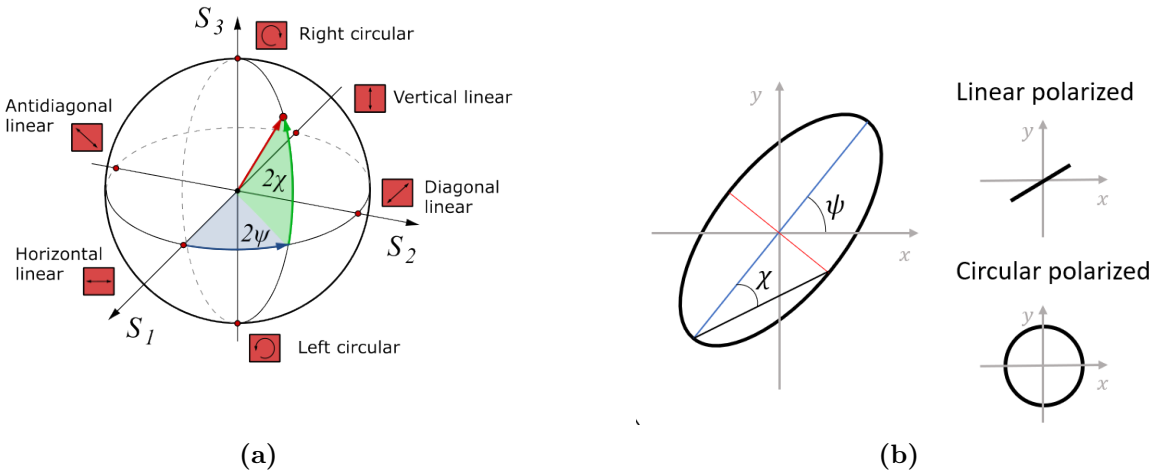

Figure 5.6.: Representations of polarization states. (a) On the Poincaré sphere, each polarization state can be mapped to a point on the sphere which is defined by the Stokes parameters (S_1, S_2, S_3) in cartesian coordinates or by the angles Φ and χ in polar coordinates. Along the equator of the sphere the polarization is linear, the south and north pole correspond to left and right circular polarization and at all other points the polarization is elliptical. (b) The polarization ellipse is defined by the angles Φ and χ. For linear polarization, the polarization ellipse becomes a line, for circular polarization, it becomes a circle.

Note that when solving these equations for Φ and χ, one has to be careful to choose the the right solution of $\arctan(x/y)$ depending on the sign of x and y. For this, one can use e.g. the *numpy.arctan2(y,x)* function in Python or *atan2(y,x)* in Matlab.
Figure 5.7 shows the experimental setup for measuring polarization profiles. First, the incoming light is made purely linearly polarized with a polarizing beam splitter. Next, it passes a half-wave plate and a quarter-wave plate that can be set to prepare any initial polarization state. Now, the q-plate can turn the uniform polarization into a vector beam. To measure the polarization at each point of the beam profile, the light is projected onto the different polarization states with a quarter-waveplate and linear polarizer (a linear polarizer can be replaced by a polarizing beam splitter plus a half-wave plate). A camera captures the intensity distribution for each projection.
Figure 5.8 illustrates the calculation of the Stokes parameters from the different polarization projections according to equation 5.29 and the resulting polarization profile represented by polarization ellipses.
Figure 5.9 shows the measured and calculated polarization and intensity profiles for different q-plate beams. Let's first look at the cases of linear incoming polarization and full conversion (figure 5.9(a) and (c)): The incoming light consists of equal amounts of left- and right circular polarized light with a relative phase delay. The q-plate converts the left into right circular polarized light and vice-versa, so the light after the q-plate is again linearly polarized. In addition, the helical phase is imprinted, which leads to a doughnut-shaped intensity profile and the rotation of the linear polarization's orientation around the center of the beam, completing one full rotation for $q = 1/2$

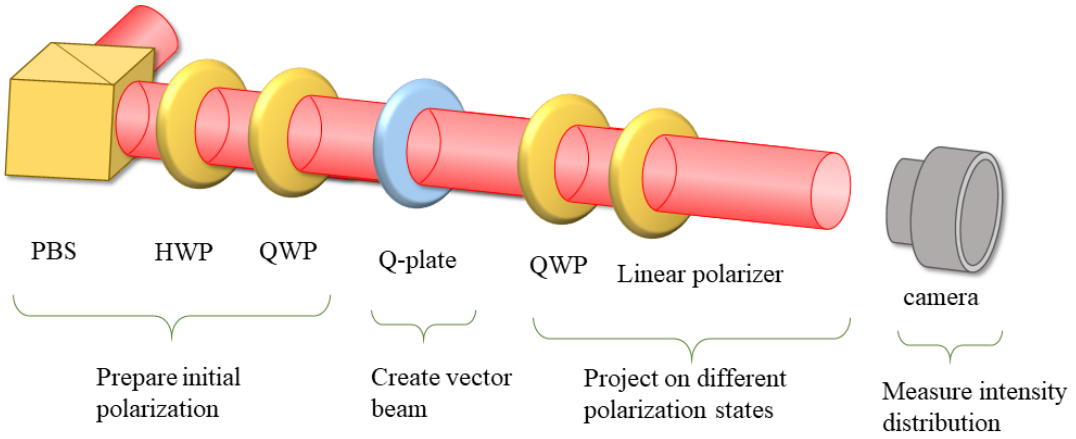

Figure 5.7.: Experimental setup to create vector beams with a q-plate and measure their polarization profiles. The polarization optics used here are a polarizing beam splitter (PBS), a half-wave plate (HWP), a quarter-wave plate (QWP) and a linear polarizer.

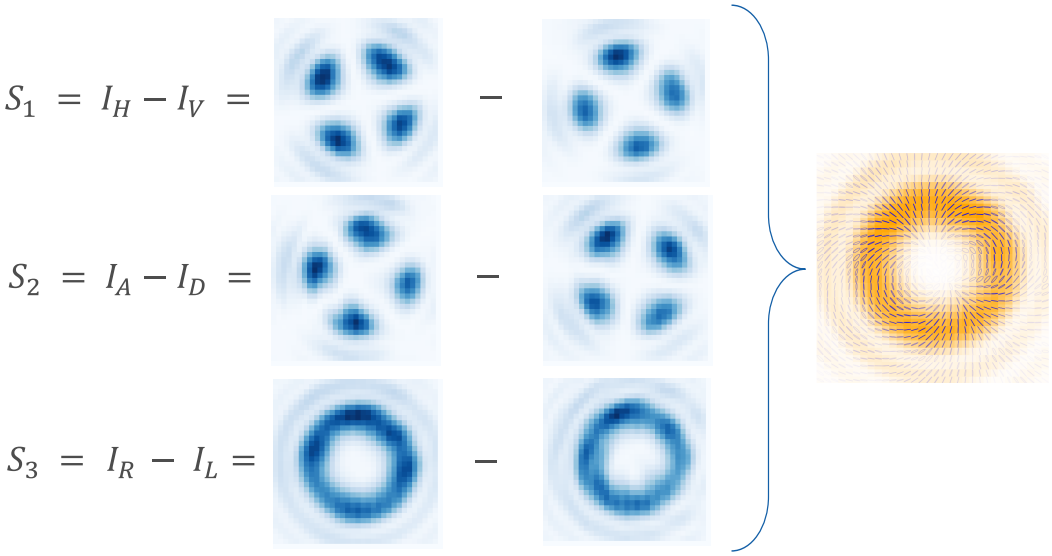

Figure 5.8.: Measuring the polarization profile of a vector beam produced by a $q = 1$ plate with the voltage set to full conversion ($I_{conv}/I_{tot} = 1$) and an incoming horizontal polarization ($|\psi_{in} = |H\rangle\rangle$). From the projections on different polarization states, the Stokes parameters are calculated at each point, which allows to plot the corresponding polarization ellipses (blue lines in the right figure) on top of the intensity profile (orange area).

(figure 5.9(a)) and two full rotations for $q = 1$ (figure 5.9(c)). For incoming circular polarization and half conversion (figure 5.9(b) and (d)), half of the beam keeps its initial polarization and Gaussian intensity profile while the other half is converted into a doughnut-shaped beam with opposite handedness of the circular polarization. As a result, the q-plate beam is in its initial polarization state in the middle, and linearly polarized on the outside, where converted and unconverted beam overlap. Even further

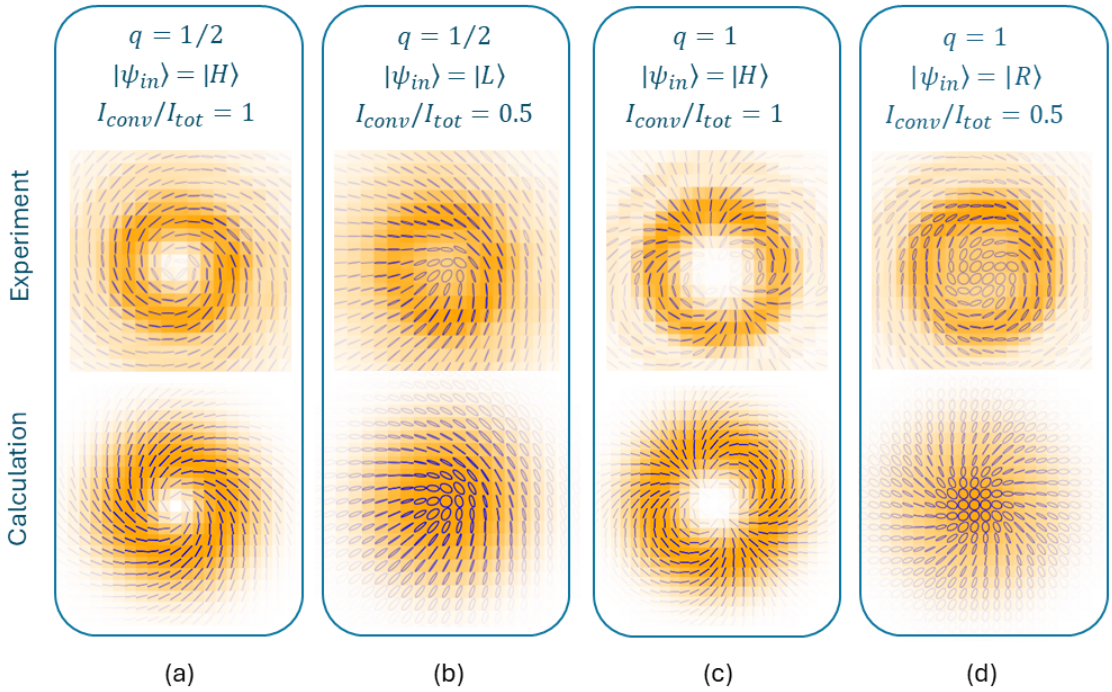

Figure 5.9.: Measured and calculated polarization and intensity profiles for different q-plate beams. (a) and (b) are for $q = 1/2$, (c) and (d) are for $q = 1$. (a) and (c) correspond to incoming horizontal polarization and full conversion ($I_{conv}/I_{tot} = 1$), (b) and (d) correspond to incoming left and right handed circular polarization and half conversion ($I_{conv}/I_{tot} = 0.5$).

from the center, the Gaussian intensity profile should decay faster, so the converted circular polarization should be visible. However, the total intensity decreases too fast on the outside to see this effect.

5.3. Calculation of optical potentials for ultracold erbium using q-plates

As we discussed in chapter 3.3, the light's polarization is important in calculating the optical potential that lanthanides experience. We are now interested in determining realistic numbers of possible potential landscapes for erbium that can be produced in our experiment using q-plates. We will take light close to the narrow transition at 841 nm such that the vectorial and tensorial components of the polarizibility play a significant role for the total trapping potential[2]. For the calculation, we assume a

[2] Note that in the Ketterle group, the equivalent transition in dysprosium at 741 nm has been used successfully to generate spin-dependent potentials by relying on the vectorial and tensorial polarizabilities [Du24].

beam with 1 mm diameter passing through a q-plate. The optical system between the q-plate and the atoms consists of a telescope with a 50 mm lens and a 300 mm lens before our objective that has a focal length of 60 mm to create a beam with a size of about 20 µm. This roughly matches the size of our optical dipole traps and would therefore ensure a large spatial overlap for loading into the 841 nm trap. The initial beam parameters $q_0 = 0$ and $\xi = 1$ evolve according the ABCD matrices of the optical system, see equation 5.25. We insert the resulting beam parameters q_0 and ξ into the circular beam model in equation 5.27 to obtain the intensity and polarization pattern in the focal plane of the objective. Then, we can calculate the optical potential for the atoms with equation 3.13 for a certain orientation of the magnetic field $\mathbf{B}$, spin state m_J and detuning δ from the transition which determines the values of the scalar, vectorial and tensorial polarizabilities.
Let's use a $q = 3$ q-plate, consider atoms in the ground state $J = 6$, $m_J = -6$, set the power of the light to 100 mW and the detuning to $5 \cdot 10^4\,\Gamma_{841} = 2.5$ GHz (which corresponds to $\alpha_s = 75.5$ a.u., $\alpha_v = -270.5$ a.u., $\alpha_t = 61.2$ a.u.). For incoming linear polarization, the q-plate creates the polarization profile shown in figure 5.10(a). Since it only contains linear polarization, the vectorial part of the potential will always be zero ($\mathcal{A} = 0$). Therefore, we can set the orientation of the magnetic field to be in the xy-plane to maximize the tensorial part of the potential ($\cos\theta_p = 1$). Figure 5.10(b) shows the resulting optical potential for this configuration. We can see that the tensorial part of the polarizability creates a modulation along the ring and the scalar part causes a constant offset. If we add a quarter-waveplate after the q-plate, linear

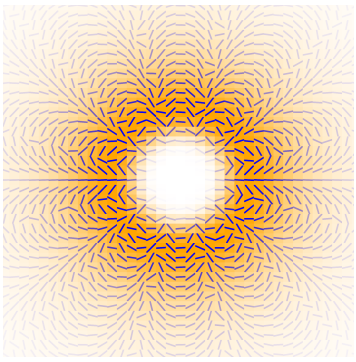

(a)

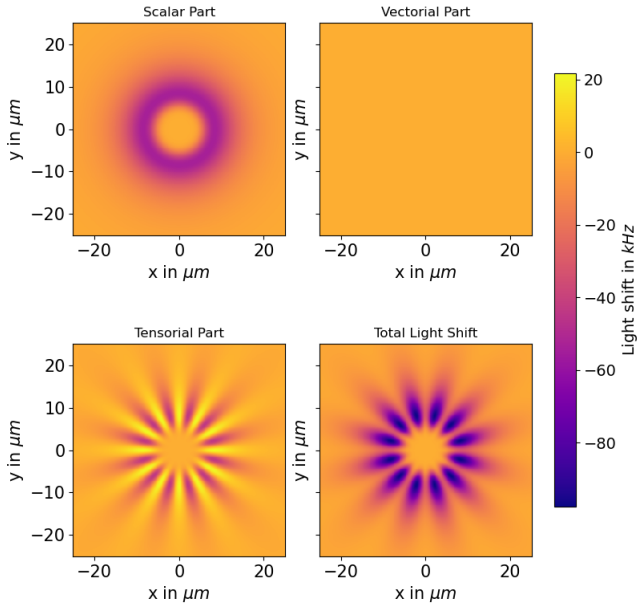

(b)

Figure 5.10.: (a) Polarization and intensity profile for $q = 3$ and incoming horizontal polarization. (b) Corresponding calculated optical dipole potential in units of the light shift for $q = 3$, $\delta = 2.5$ GHz, the magnetic field oriented in the xy-plane.

and circular polarization alternates in the polarization profile, see figure 5.11(a). By setting the magnetic field in the z-direction, this allows us to have a modulation of the optical potential along the ring because of the vectorial part which is shown in figure 5.11(b). We can also choose a higher order q of the q-plate: Figure 5.12 depicts the

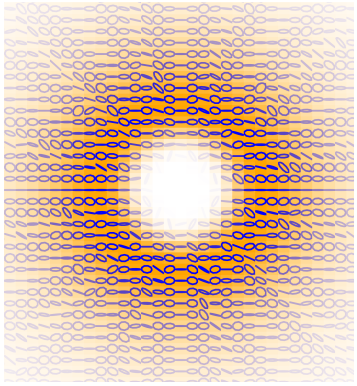

(a)

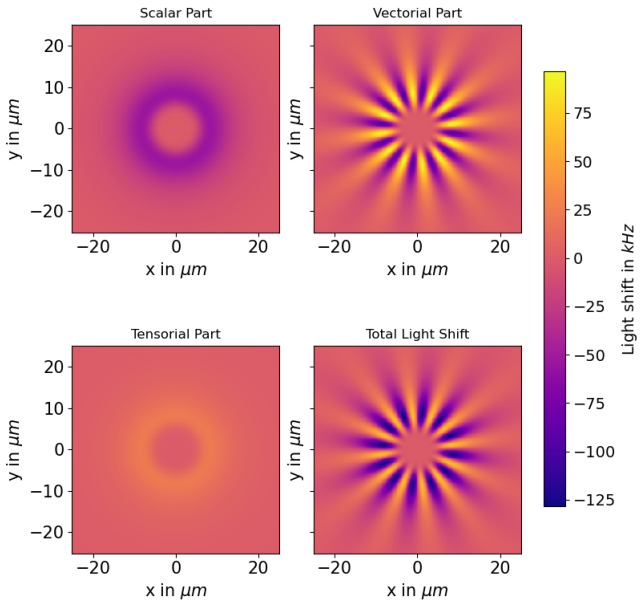

(b)

Figure 5.11.: (a) Polarization and intensity profile for $q = 3$ and incoming horizontal polarization with an additional quarter wave plate after the q-plate. (b) Corresponding calculated optical dipole potential in units of the light shift for $q = 3$, $\delta = 2.5\,\mathrm{GHz}$, the magnetic field oriented in the z-plane.

optical potential for $q = 10$. Here, we can see that the number of modulations along the ring increases accordingly. However, the order of the q-plate changes the beam size which more than doubles in this case.
Note that this calculation model doesn't include diffraction, meaning that the smallest modulation that can be created by our optical is given by the diffraction limit. In the erbium experiment, the objective has a numerical aperture of $NA = 0.46$ [Laf22], so the diffraction limit is $1.22\lambda/(2NA) = 1.1\,\mu\mathrm{m}$.
The discussed examples above are for fixed parameters of the detuning, input polarization, atomic state and magnetic field angles. We can also change the detuning of the light to control the absolute and relative strength of the scalar, vectorial and tensorial polarizabilties. Reducing the detuning from the transition increases the strength of the vectorial and tensorial parts compared to the scalar part, but this also increases the phonon scattering the causes heating and atoms loss. At fixed detuning, the relative strength of vectorial and tensorial part can be tuned by tilting the magnetic field.

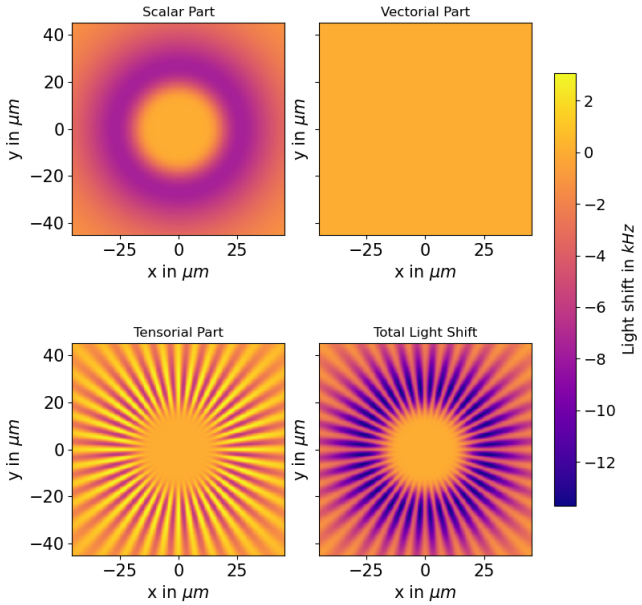

Figure 5.12.: Calculated optical dipole potential in units of the light shift for $q = 10$, $\delta = 2.5\,\mathrm{GHz}$, the magnetic field oriented in the xy-plane and incoming horizontal polarization.

5.4. Possible challenges for implementing q-plates

Up to now, I have shown that q-plates are a promising tool to create spatial polarization patterns that can be used to realize potential patterns for our ultracold erbium atoms. However, there are some challenges one can foresee when implementing q-plates in the experimental setup:

- Changing the order of the q-plate: The LC pattern on each q-plate is fixed, so the q-plate has to be exchanged and realigned. Moreover, the optical setup has to be adjusted if one wants to keep the same beam size at the position of the atoms, since the beam size depends on the order of the q-plate.

- Photon scattering and heating: In the previous calculations, the scattering rate is kept below $0.1\,\mathrm{s}^{-1}$, but in the experiment the actual scattering rate can be much larger. Furthermore, the voltage applied to drive the q-plate has to alternate at a few kHz which could introduce additional heating.

- Transmission and damage threshold at 841 nm: At the q-plate, some of the light is lost due to reflection or absorption which reduces the light's power on the atoms. We quantify the losses at 841 nm in the following section 5.4.1.

- Longitudinal polarization effects: This can arise due to tight focusing of light with radial polarization components and are discussed in the following section

5.4.2.

- Aberrations and imperfections in the optical system: This can give rise to a spatial non-uniformity of the intensity profile and therefore unwanted effects on trapping potential for the atoms. To mitigate this issue, one could use an alternative method to create vector beams which allows for error correction with active feedback. In the following section 5.4.3, we explain the advantages and disadvantages of alternative methods to q-plates, which rely on liquid-crystal spatial light modulators.

5.4.1. Transmission and damage threshold at 841 nm

As with all optical components, some of the light is lost as it passes through the q-plate because of absorption or back-reflection. The loss fraction can depend on the wavelength and intensity of the light. Therefore, we tested the loss through a q-plate with 841 nm light and a waist of 385 μm. For the loss fraction

$$\eta = 1 - \frac{P_{out}}{P_{in}} \tag{5.32}$$

we measure $\eta = 20(1)\,\%$ for $P_{in} = 5.1(1)\,\mathrm{mW}$ and $\eta = 15(1)\,\%$ for $P_{in} = 16.8(1)\,\mathrm{mW}$. Unfortunately, we could not test the loss at higher power but from this measurement we can conclude that we expect a power loss of $15 - 20\%$ for 841 nm light.
Laser light can also damage the q-plate by reorienting the liquid crystals. This is expected to happen only at wavelengths below 600 nm, but should be tested nevertheless for each wavelength. Therefore, we focus the 841 nm light with 15.5(1) mW down to a waist of 22 μm and shine it on different spots of the plate. By inspecting the q-plate between two crossed polarizers, no damage to the liquid crystal pattern was found, so we conclude that the 841 nm light does not affect the q-plate pattern.

5.4.2. Longitudinal polarization effects

For tight focusing of light, the paraxial approximation breaks down and the light can have a longitudinal polarization component [Ric59, You00, Zha02]. This means that the polarization vector is no longer restricted to the plane perpendicular to the propagation direction, but can rather have a non-negligible and even dominant component along the propagation direction.
This effect can be undesired, as described in an optical tweezer experiment for single rubidium atoms in the Lukin group [Tho13]: Here, tight focusing of 815 nm light down to a waist of only 900 nm creates longitudinal polarization effects that cause a polarization gradient illustrated in figure 5.13. Rubidium is an alkali atom, so it

experiences a vectorial light shift that depends on the hyperfine state of the atom and the polarization of the light. In the Lukin experiment, the vectorial light shift due to the polarization gradient causes unwanted dephasing of the internal hyperfine states which they successfully mitigate by applying a magnetic bias field.

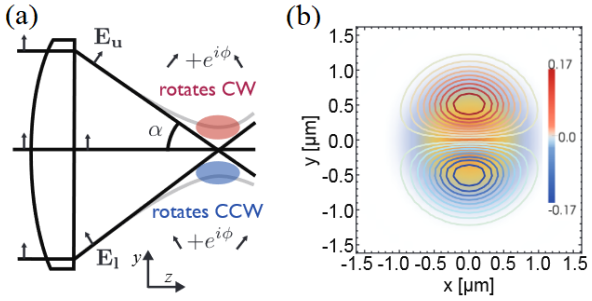

Figure 5.13.: Longitudinal polarization effects in an optical tweezer. (a) Due to tight focusing (NA = 0.43) of initially linearly polarized light, the light gets effectively elliptically polarized in the yz-plane with opposite rotation directions of the polarization vector above and below the optical axis. (b) The contour lines indicate the degree of ellipticity of the polarization in the xy-plane at the focus. Adapted from [Tho13].

In contrast, longitudinal polarization effects can also be desired and used a tool in the wider context of "structured light", a notion which describes the idea of using all degrees of freedom to control a light beam for different applications [For21]. For example, it was first demonstrated experimentally in 2003 that light with strong longitudinal polarization can be focused down to a significantly smaller spot size than light with transverse polarization [Dor03]. The tight focusing of light with a spatially non-uniform polarization pattern allows to create three-dimensional polarization objects such as a Moebius strip shown in figure 5.14 [Bau15]. In super-resolution optical microscopy, structured light created by cylindrical vector beams can improve resolution both in the near-field (e.g. scanning microscopy with a metal or fiber tip) and far-field (e.g. stimulated emission depletion (STED) microscopy). A nice summary of recent advances in this field of research can be found in reference [Liu22a]. Furthermore, longitudinal polarization effects are well-known for light-matter interfaces in nanophotonics where atoms are placed at subwavelength distances from dielectric boundaries [Lac12]. For example, by exploiting longitudinal polarization effects, the spontaneous emission of atoms into a nanophotonic waveguide can be forced to go only into only one direction with an efficiency of 90% [Mit14].
To estimate the amount of longitudinal polarization we can have for tight focusing with our numerical aperture of NA = 0.46, we use the Richards-and-Wolf method [Ric59] that is explained now using references [Nov12, Zha09, Bau17]. We start with a incident electric field that is paraxial in the sense that it is only polarized in the plane transverse to the propagation direction z:

$$\vec{E}_{\text{in}}(\rho,\phi) = \mathcal{E}(\rho)(\cos\varphi_0\,\vec{e}_\rho + \sin\varphi_0\,\vec{e}_\phi). \tag{5.33}$$

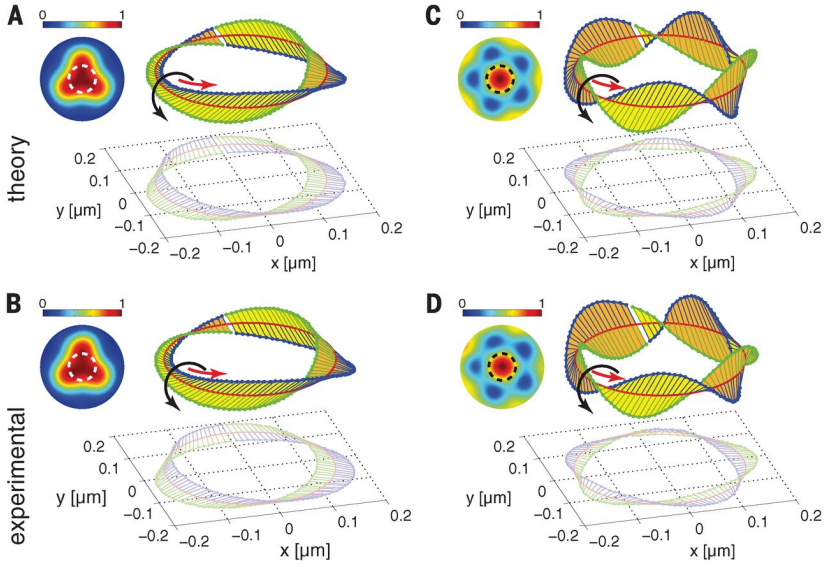

Figure 5.14.: Polarization topology achieved by tight focusing (NA = 0.9) of light emerging from a q-plate. The plots show the main axis of the 3d-polarization ellipse that exhibits a Moebius-strip topology. For $q = -1/2$ (A-B), the strip has three half-twists and for $q = -3/2$ (C-D) the strip has five half-twists. The upper row corresponds to theoretical calculations, the bottom row shows experimental results obtained from reconstructing the electric field distribution by collecting light scattered from a gold nanoparticle. Taken from [Bau15].

Here, we use cylindrical coordinates (ρ, ϕ, z) with the corresponding unit vectors $(\vec{e}_\rho, \vec{e}_\phi, \vec{e}_z)$. The amplitude of the initial electric field is given by $\mathcal{E}(\rho)$ and its polarization by φ_0 where $\varphi_0 = 0$ for azimuthal polarization $\varphi_0 = \pi/2$ for radial polarization as illustrated in figure 5.15.
The key part of the Richards-and-Wolf method is now to transform the plane that the incident field occupies into a so-called reference sphere with radius f as shown in figure 5.16. This means that we have to transform the cylindrical coordinates to spherical coordinates so that the electric field on the sphere becomes

$$\vec{E}_\infty(\theta, \phi) = \mathcal{E}'(\theta)(\cos\phi_0\, \vec{e}_\theta + \sin\varphi_0\, \vec{e}_\phi) \tag{5.34}$$

where the subscript of $\vec{E}_\infty$ indicates that the reference sphere is in the far field of the focal plane ($z \ll f$). Looking at the corresponding unit vectors in cartesian coordinates

$$\begin{aligned} \vec{e}_\rho &= \cos\phi\, \vec{e}_x + \sin\phi\, \vec{e}_y \\ \vec{e}_\phi &= -\sin\phi\, \vec{e}_x + \cos\phi\, \vec{e}_y \\ \vec{e}_\theta &= \cos\theta\, \vec{e}_\rho - \sin\theta\, \vec{e}_z \end{aligned} \tag{5.35}$$

it becomes clear this transformation introduces a longitudinal component of the electric field since $\vec{e}_\theta$ is the only unit vector with a z-dependence ($\vec{e}_\rho$ and $\vec{e}_\phi$ are the same in both coordinate systems). The electric field strength transforms as

$$\mathcal{E}'(\theta) = \mathcal{E}(f \sin\theta)\sqrt{\cos\theta} \tag{5.36}$$

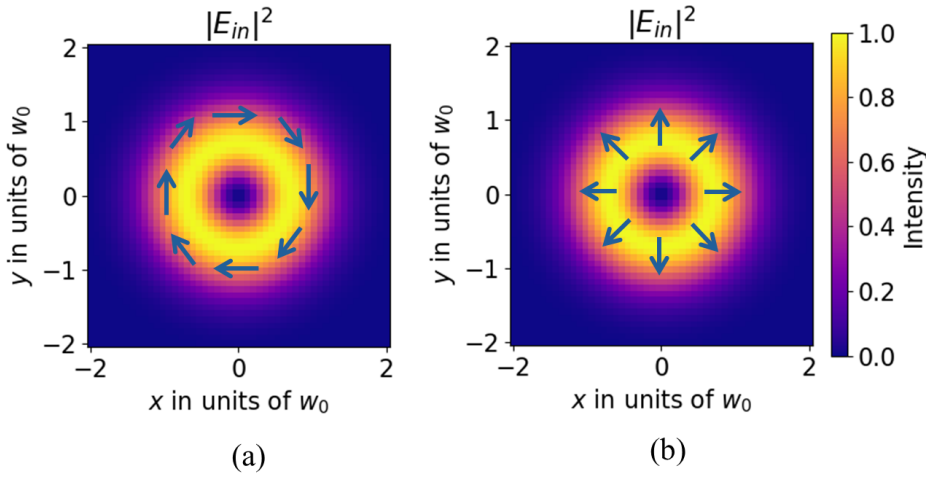

Figure 5.15.: (a) Azimuthal and (b) radial polarization of the incoming electric field with the intensity profile of the Laguerre-Gauss mode $LG_{0,1}$.

where the factor of $\sqrt{\cos\theta}$ is required for power conservation and the ρ-dependence of the field strength $\mathcal{E}(\rho)$ is eliminated by using the Abbe sine condition $\rho = f \sin\theta$ that most objective lenses fulfil.
The last step of the Richards-and-Wolff method is to calculate the resulting electric field $\vec{E}(r, \varphi, z)$ close to to the focus. According to the far-field approximation of Fourier optics,

$$\vec{E}(r, \varphi, z) = \frac{-ik}{2\pi} \iint_{\Omega} d\,\Omega\; \vec{E}_{\infty}(\theta, \phi) e^{ik\vec{s}\cdot\vec{r}} \tag{5.37}$$

where $\vec{s} = (k_x, k_y, k_z)/k$ is a unit vector on the reference sphere and $k = 2\pi/\lambda$ is the wave number. Basically, the idea here is to calculate the electric field $\vec{E}(\vec{r})$ at each point $\vec{r} = (r, \varphi, z)$ close to the focus by integrating over the electric field $\vec{E}_{\infty}$ and all vectors $\vec{s}$ on the reference sphere in the solid angle Ω (a more rigorous proof of equation 5.37 can be found in [Nov12]). Close to the focus

$$\vec{s}\cdot\vec{r} = z\cos\theta + r\sin\theta\cos(\phi - \varphi) \tag{5.38}$$

holds, so we get

$$\vec{E}(r, \varphi, z) = \frac{-ik}{2\pi} \int_0^{\theta_{\max}} d\theta \int_0^{2\pi} d\phi \vec{E}_{\infty}(\theta, \phi) e^{ikz\cos\theta} e^{ikr\sin\theta\cos(\phi-\varphi)} \tag{5.39}$$

which can be simplified with the help of the Bessel functions $J_i(x)$ of the first kind since

$$\begin{aligned} \int_0^{2\pi} d\phi \cos(n\phi) e^{ix\cos(\phi-\varphi)} &= 2\pi i^n J_n(x)\cos(n\varphi)) \\ \int_0^{2\pi} d\phi \sin(n\phi) e^{ix\cos(\phi-\varphi)} &= 2\pi i^n J_n(x)\sin(n\varphi)) \end{aligned} \tag{5.40}$$

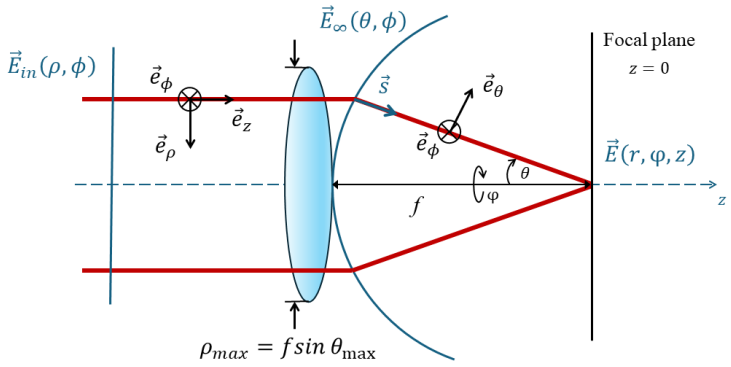

Figure 5.16.: Illustration of the Richards and Wolf method. The incoming electric field $\vec{E}_{\text{in}}$ is restricted to the plane transversal to the propagation direction. Tight focusing with a lens with focal length f and numerical aperture $NA = \sin\theta_{\max}$ can give rise to a longitudinal polarization effects. The field $\vec{E}$ in the focal plane is calculated by transforming the transversal plane into a sphere and calculating the far-field Fourier integral of the field $\vec{E}_\infty$ on the sphere.

With this, we arrive at the final expression for the electric field close to the focus

$$\vec{E}(r,\varphi,z) = k\int_0^{\theta_{\max}} d\theta\ \mathcal{E}(f\sin\theta)\sin\theta\sqrt{\cos\theta}\ e^{ikz\cos\theta}\times \tag{5.41}$$
$$\left(\cos\varphi_0\begin{pmatrix}\cos\theta\cos\varphi J_1(kr\sin\theta)\\ \cos\theta\sin\varphi J_1(kr\sin\theta)\\ i\sin\theta J_0(kr\sin\theta)\end{pmatrix} + \sin\varphi_0\begin{pmatrix}-\sin\varphi J_1(kr\sin\theta)\\ \cos\varphi J_1(kr\sin\theta)\\ 0\end{pmatrix}\right).$$

Now, we calculate the electric field for specific configurations of interest. We use the incident field strength of the Laguerre-Gauss mode $LG_{0,1}$

$$\mathcal{E}(\rho) = E_0\frac{\rho}{w_0}e^{-\rho^2/w_0^2} \tag{5.42}$$

with intensity profile shown in figure 5.15. First, we use the same parameters $w_0/f = 0.95$, $NA = 0.9$ and $\lambda = 530\,\text{nm}$ as in reference [Bau17] to compare their results for a consistency check. Indeed, the results shown in figure 5.17 agree with figures 2.4 and 2.5 in [Bau17]. For azimuthal polarization of the incoming field, there is no longitudinal component of the electric field while for radial polarization, 44.7 % of the total power go into the longitudinal component.
For our case, we have $\lambda = 841\,\text{nm}$ and $NA = 0.46$. For choosing the parameter w_0/f, we see from figure 5.15 that we can cut the intensity profile of the Laguerre Gauss beam at $3/2w_0$. Therefore, the maximum w_0 for our objective with diameter d is $w_0 = 2/3 \cdot d/2$. Since $f = d$ for our objective, we get $w_0/f = 1/3$. The results of

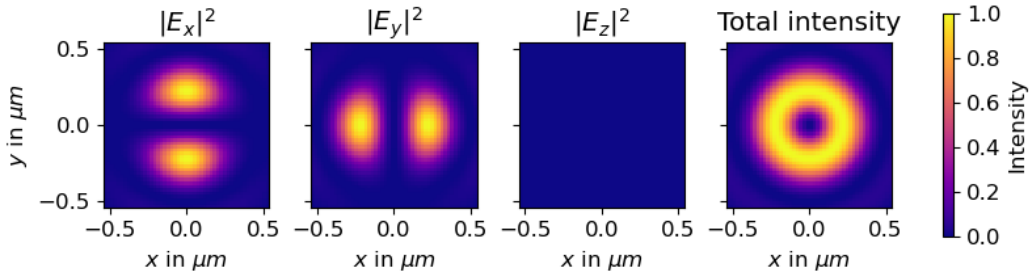

(a) For $\vec{E}_{in}$ azimuthally polarized

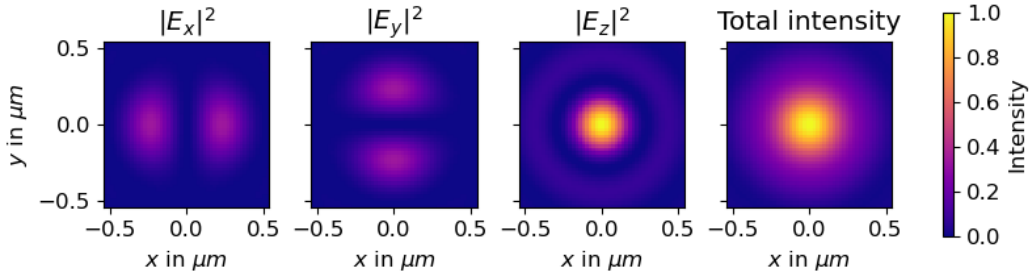

(b) For $\vec{E}_{in}$ radially polarized

Figure 5.17.: Results of the Richards and Wolf method in the focal plane for (a) azimuthal and (b) radial polarization of the incoming electric field: Intensity in the transversal x- and y-component and in the longitudinal z-component of the electric field as well as the total intensity for the parameters $\lambda = 530\,\text{nm}$, $w_0/f = 0.95$ and $NA = 0.9$ used in [Bau17]. All intensities are normalized to the maximum of the total intensity.

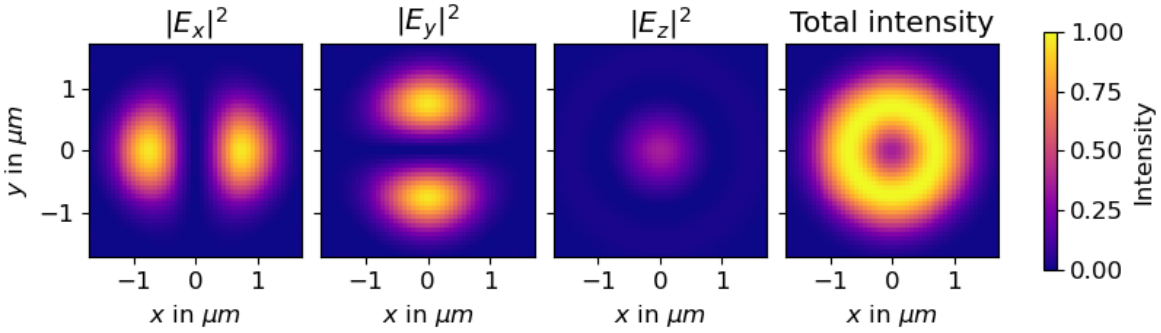

Figure 5.18.: Results of the Richards and Wolf method in the focal plane for radial polarization of the incoming electric field with our parameters $\lambda = 841\,\text{nm}$, $w_0/f = 1/3$ and $NA = 0.46$. All intensities are normalized to the maximum of the total intensity.

the Richards and Wolf method are shown in figure 5.18. For the worst-case scenario of radial polarization of the incoming beam and maximum waist w_0, only 8.7 % of the total power goes into the longitudinal polarization component. This means that we can expect that effects coming from longitudinal polarization components will be

rather minor. Since the light with the longitudinal component is distributed at the center of the beam, it does not affect the potential formed by the intensity ring of the Laguerre-Gauss mode.

5.4.3. Alternative methods to implement vector beams

Liquid-crystal spatial light modulators (LC SLMs) allow to create optical fields with tailored phase and intensity profiles [Yan23]. This is achieved by controlling the LC orientation at each pixel of the SLM, which imprints a phase pattern on the incoming beam. To obtain a spatial modulation of the intensity, one observes the beam profile in the Fourier plane of the SLM.
The control over each pixel of the SLM allows to create arbitrary intensity and phase profiles and to correct for optical aberrations relying on an active feedback mechanism. The most widely used technique for this is the Gerchberg-Saxton algorithm that is based on iterative Fast Fourier Transforms (FFT) of the electric field in the SLM plane to the far-field Fourier plane and vice-versa via inverse FFT. An advanced version of this algorithm for better uniformity of the reconstructed image is the weighted Gerchberg-Saxton algorithm that has been realized for an SLM in our group [Hen23].
One disadvantage of SLMs is that the voltage applied to the SLM pixels has to be alternating, which leads to the same temporal fluctuations as for the q-plate. In the context of SLMs, this cycling rate is called phase flicker and lies in the range of a few Hz to kHz depending on the device. A review about the phase flicker as well as efforts to reduce it can be found in reference [Yan20].
The main drawback of SLMs is that they require incident light with a specific orientation of linear polarization. This means that one can not choose arbitrary polarizations of the incoming light to obtain the desired polarization pattern at the output. However, by letting two Laguerre-Gauss or Hermite-Gauss modes of orthogonal linear polarization interfere one can create arbitrary vector beams [Mau07, Liu18, RG17]. Figure 5.19 shows that for this, the light is split into two beams that each illuminate one half of the SLM. In one path, there is a $\lambda/2$ waveplate to rotate the linear polarization to the right orientation before and after the reflection at the SLM. There exist also different methods to create arbitrary vector beams with SLMs, such as cascading two SLMs [GM20] or spatial multiplexing (superimposing two holograms) on a single SLM [Ott18, RG20].

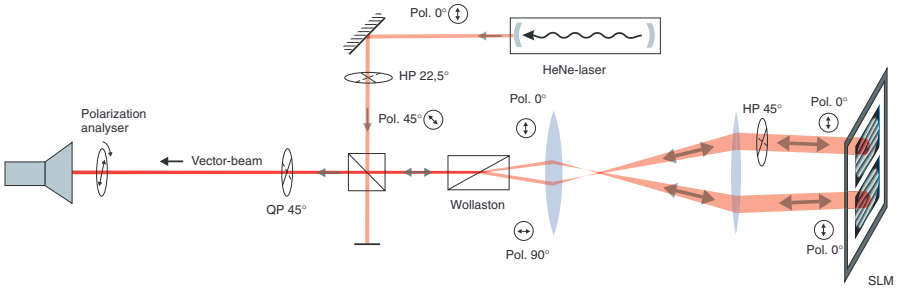

Figure 5.19.: Interferometric method for generating arbitrary vector beams with an SLM. Linearly polarized light is deflected by a non-polarizing beam splitter, then a Wollaston prism splits the light into two beams with orthogonal polarization and equal intensity. To match the polarization orientation required by the SLM, a $\lambda/2$ wave plate rotates the polarization in one of the beams. The SLM displays two adjacent holograms that transform the beams into Laguerre-Gauss or Hermite-Gauss modes that are diffracted back and interfere at the Wollaston prism. The $\lambda/4$ wave plate turns the orthogonal linear polarizations into left- and right-circular polarizations. Figure taken from [Mau07].

Chapter 6

Conclusion and Outlook

Summary

The first goal of this thesis was to install a new scanning optical dipole trap with far-detuned 1064 nm light in the experiment. For this, we periodically displace the 1st diffraction order of an acousto-optical modulator. Because this "scanning" of the beam takes place at a frequency faster than the harmonic trap frequency, the atoms effectively see an time-averaged potential given by the elliptical beam shape. To achieve the scanning, we have to change the bandwidth of the radio-frequency signal that is generated with a voltage-controlled oscillator and controls to the AOM. To test this offline, the optical setup is installed on a small breadboard. Because of the limited space on the experimental table, the setup is very compact and therefore challenging to align. However, we managed to get a symmetric beam profile, where the waist in the scanning direction is tunable from 22.38(2) μm to 169.3(2) μm and the waist in the other direction stays constant with a waist of 25.5(2) μm. This means that the maximum aspect ratio is 6.8 which is below the theoretically achievable aspect ratio of about 9. Possible reasons for this are imperfections in the alignment and the limited bandwidth of the VCO. After implementing the setup into the experiment, we perform trap frequency measurements by exciting the dipole mode and measuring the oscillation frequency of the atomic cloud. We conclude that the trap frequency in the scanning direction can be tuned from $2\pi \times 203.3(6)$ Hz without scanning to $2\pi \times 64(3)$ Hz at the maximum scanning amplitude. To fully characterize the trap in the future, we will have to determine the aspect ratio for different scanning amplitudes by additionally measuring the trap frequency in the direction without scanning.
The second goal of this master thesis was to investigate possible applications of q-plates for our experiment. Q-plates consist of a liquid crystal material where a specific liquid crystal pattern is imprinted. This introduces a helical phase on light passing the plate, thus generating an optical vortex. The intensity profile of the beam can be described by a circular beam model and approximated by Laguerre-Gauss modes in the far-field. Q-plates can generate vector beams with a polarization profile that varies in the radial direction. Because the atom-light interaction of erbium atoms is polarization-dependent, q-plate beams could be used to generate optical potentials for

erbium with a ring lattice geometry. To calculate the potential landscape, we first use the ABCD matrix formalism together with a circular beam model to get the polarization and intensity profile of the beam in the focal plane of the objective. We find that the potential landscape can be tuned by inserting a quarter wave plate after the q-plate, or changing the order of the q-plate. Even though the calculations are promising, the implementation of q-plates into the experiment could pose several challenges, especially regarding atom loss due to photon scattering and aberrations and imperfections in the optical system that could introduce unwanted effects on the trapping potential.

Next steps regarding optical lattices

The first step towards loading atoms into a optical lattice was setting up the new scanning optical dipole trap, as the old one blocked the space needed for the lattice beam paths. The next steps are to install the two crossed lattice beams at 532 nm in the horizontal plane and the vertical lattice beam at 1064 nm. Once these beams are well-aligned, the atoms can be loaded into the lattice and the lattice depth can be calibrated. This can be done by measuring the number of atoms in the diffraction peaks of the matter-wave interference pattern that can be observed with absorption imaging after time of flight [Gad09].
One motivation for setting up the optical lattice is to facilitate collisional studies of spin-polarized erbium atoms. With our spin preparation scheme that relies on the narrow inner-shell 1299 nm transition, we can prepare bosonic erbium in its ground state ($J = 6$) in any spin state (Zeeman sublevels $m_J = -6...6$) [Cla24]. Collisional losses occur mainly due to two processes: two-body spin exchange (where one atom changes its spin state as $\Delta m_J = +1$ and the other as $\Delta m_J = -1$) and two-body spin relaxation (where one or both atoms lower their spin $\Delta m_J = -1$). By driving the 1299 nm transition, we induce a light shifts on a selected Zeeman sublevel and therefore close the spin relaxation loss channel. This allows us to deterministically prepare dual-spin mixtures, opening up the exciting possibility to systematically study the intra- and interspin Feshbach resonances of erbium. However, the remaining magnetic-field dependent spin relaxation process modifies the atomic loss spectrum when investigating Feshbach resonances. By confining the atomic sample in an optical lattice, spin relaxation can be diminished [Pas10].
Furthermore, dipolar atoms in optical lattices are promising platforms to realize Bose- and Fermi-Hubbard models for quantum simulation. More specifically, we could load to the fermionic isotope into the optical lattice which has already been achieved before [Pat20], and aim for realizing the anisotropic t-J model investigated theoretically for polar molecules in reference [Faz19]. The long-range interaction gives rise to a rich phase diagram, including topological superconducting phases. However, investigating these predictions experimentally poses several challenges, for example controlling the anisotropy of the nearest-neighbor couplings and the filling fraction. Moreover, to prove topological order and superconductivity, one has to determine specific non-local order parameters and the decay of certain correlation functions, which requires spin-

resolved single-site resolution. So far, only one quantum gas microscope with dipolar atoms has been achieved in the Greiner group [Su23]. It relies an accordion lattice that expands the lattice for imaging. Due to technical limitations, this deterministic super-resolution technique is not feasible for us. However, stochastic super-resolution imaging that is inspired from biology [Liu22b, Jac20] and has already been applied in ultracold atom experiments [Sub19, McD19] could solve this issue.

Outlook on using 841nm light for a second stage MOT and generating optical potentials with q-plates

We have recently bought a Toptica 841 nm laser that has an output power of 2 W and will be used for two purposes: a second stage of the MOT and generating optical potentials with q-plates or a DMD. The reason why we want to add a second stage to the MOT is to decrease the duration of the experimental sequence. Compared to the 583 nm transition ($\Gamma_{583} \approx 2\pi \times 190\,\mathrm{kHz}$), the Doppler temperature $\hbar\Gamma/(2k_B)$ of the 841 nm transition ($\Gamma_{841} \approx 2\pi \times 8\,\mathrm{kHz}$) is much lower, so a MOT operating on this transition can achieve the temperature and phase-space density for loading into the optical dipole traps faster (with the drawback of a lower radiation pressure force to hold the atomic cloud against gravity). A MOT with blue-detuned 841 nm light has been demonstrated by Berglund et al. in 2008 [Ber08] and a MOT with red-detuned 841 nm light as a second stage to a 583 nm MOT has been realized in the Greiner group in 2020 [Phe20, Phe19]. In the latter case (with an additional stroboscopic technique for loading into the ODTs), it was possible obtain a BEC of 8×10^4 erbium atoms with a condensate fraction of 85% in 800 ms and a degenerate Fermi gas in 4 s, a drastic speedup compared to typical cycle times in ultracold experiments of 10 s to a minute. In order to use the 841 nm light for the MOT and optical trapping potentials, we need to lock the laser to an ULE cavity that has been built by our group [Rie12]. Currently, the plan is to lock the laser at GHz detuning from the transition and to use this light for the optical trapping potentials generated by q-plates. For the MOT, the light needs to be detuned only by few MHz at most, so we intend to shift the frequency closer to the transition with a fiber-coupled electro-optical modulator (fEOM). In this way, we aim to use the 841 nm light for a second stage MOT to significantly reduce the 12 s cycle time of our experiment.
Regarding the implementation of q-plates, the atoms could be loaded from the optical dipole trap into the ring lattice in three steps: First, as the 841 nm light is turned on, the voltage at the q-plate is set to zero conversion to obtain a Gaussian beam and hence a harmonic trap at 841 nm. Then, the voltage can be changed adiabatically to achieve full conversion of the light to a circular beam, but the incoming polarization is circular to create a uniform ring trap. Last, the incoming polarization changes to linear to create the modulations on the ring. The first step could improve the loading efficiency compared to loading directly into the ring trap by ensuring a larger spatial overlap with the ODT beams, depending on their relative size. In the ring lattice, the transition from the Mott insulator state to superfluid and density-wave states could be investigated [Mai11].

Appendix

A

Appendix

A.1. Electronic circuit for the scanning ODT

For the implementation of the scanning ODT, the electronics that generate the RF-signal for the AOM have to be interfaced with the control software of the experiment. Therefore, the electronics of the offline testing described in section 4.3 have to be modified. We implement the electronic circuit shown schematically in figure A.1. The

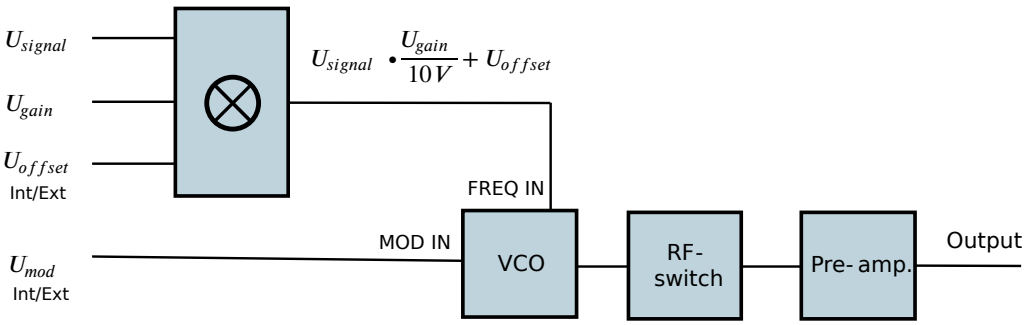

Figure A.1.: Schematic drawing of the electronics implemented on the experiment. The output signal only has to pass one more amplifier before it reaches the AOM.

input channels U_{offset}, U_{gain} and U_{mod} can be connected to voltage outputs that are controlled by software of the experiment. The shape of the modulation signal U_{signal} is generated by a function generator as for the offline testing. The voltages U_{offset}, U_{gain} and U_{signal} are combined with a mixer to create the signal

$$U_{\text{FREQIN}} = U_{\text{gain}} \frac{U_{\text{signal}}}{10V} + U_{\text{offset}} \qquad \text{A.1}$$

that goes to the VCO's FREQ IN channel. In this way, we can control the amplitude of the modulation signal independently of the offset: We can change U_{gain} and don't rely on changing U_{mod} which would multiply the full VCO output signal by some factor.

The VCO's output signal can be switched on and off with an RF-switch that is also controlled by the experiment's software. Finally, the modulation signal is sent to the pre-amplifier and another amplifier before it reaches the AOM.
To realize the electronic scheme in figure A.1, we implement the circuit in figure A.2. It powers the RF-switch (5 V), the pre-amplifier (15 V) and the VCO (24 V) and controls the VCO's input signals. The electronics are now more compact compared to the old scanning ODT: The circuit in figure A.2, the RF-switch and the pre-amplifier fit conveniently in one rack-mounted electronics box. Furthermore, the VCO is attached directly to this box and only one additional amplifier is needed after the VCO because of the pre-amplifier. Figure A.3 shows a photo of the inside of the electronics box.

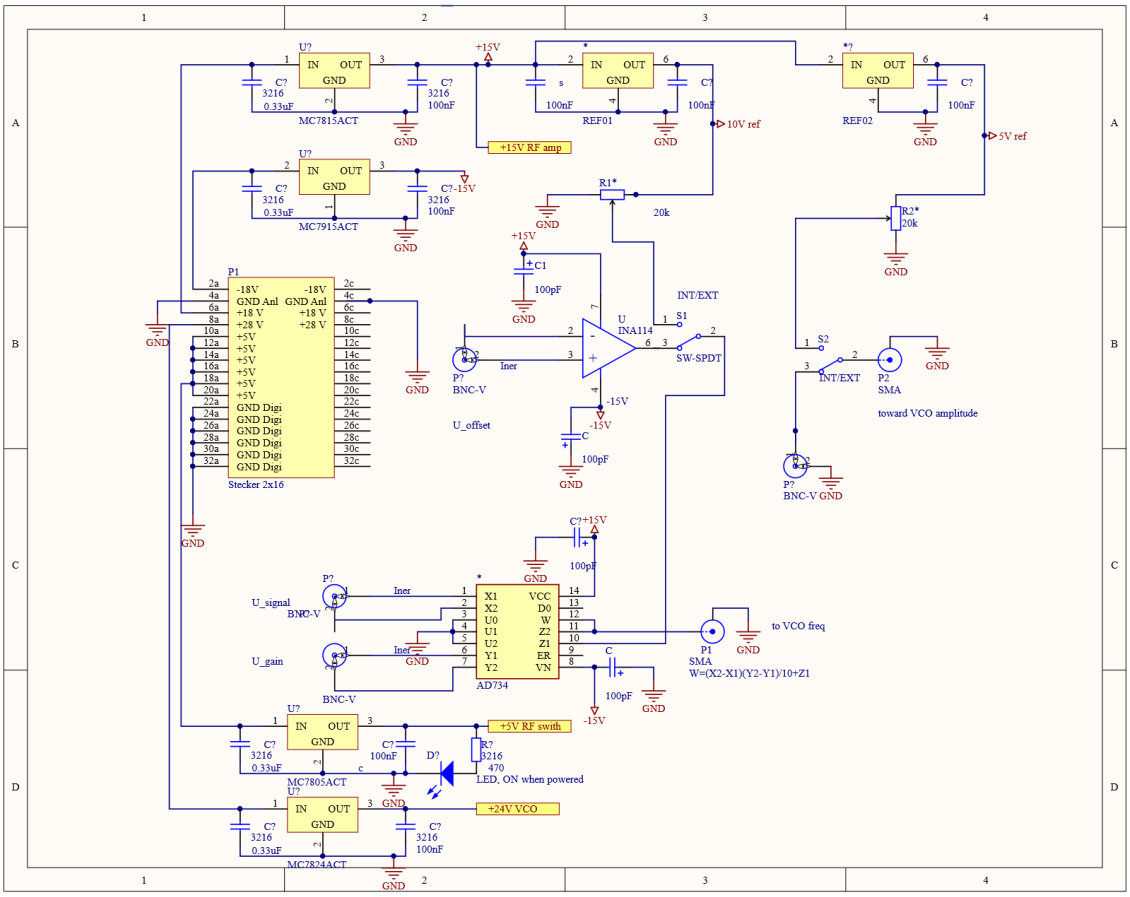

Figure A.2.: Electronic circuit for controlling the scanning ODT.

For setting up the electronics, we set the voltages as follows: The voltage U_{mod} is set to constant 5 V internally, U_{offset} is set internally such that we are at the center frequency of the AOM. For U_{signal}, we use the same arc-cos signal as for the offline testing. The gain of the last amplifier is optimized to achieve the right power of the RF-signal. Then, we can change U_{gain} during the MOT loading and evaporation sequence.

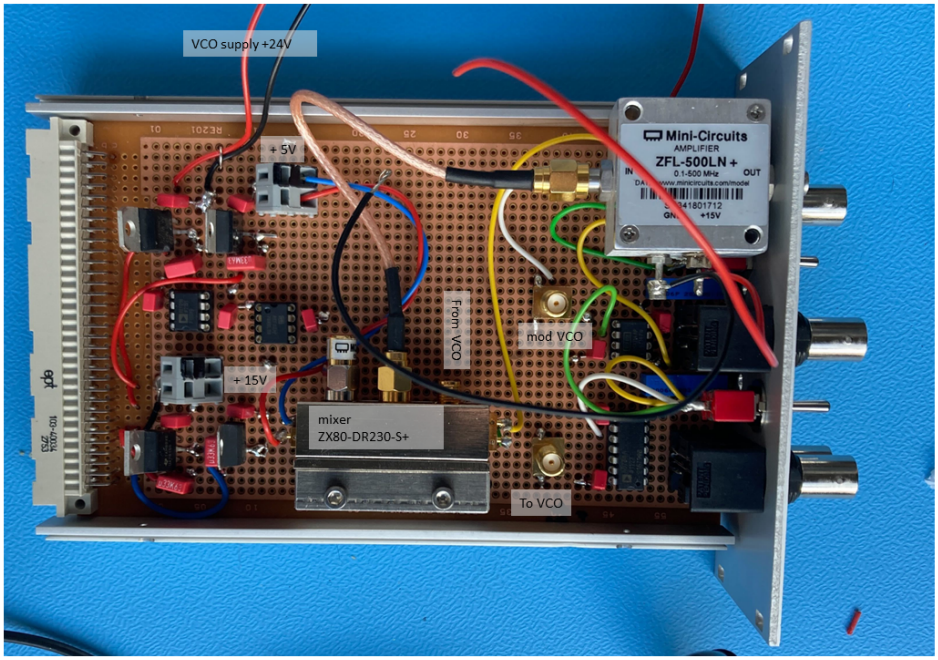

Figure A.3.: Photo of the electronics box.

Bibliography

[AAo13] AAoptoelectronic, Acousto-optic Theory Application Notes. [Online]. Available: https://aaoptoelectronic.com/wp-content/uploads/2024/04/AAOPTO-Theory2013-4-1.pdf [2024, November 15].

[Aik12] K. Aikawa, A. Frisch, M. Mark, S. Baier, A. Rietzler, et al., *Bose-Einstein Condensation of Erbium*, Phys. Rev. Lett. **108**, 210401 (2012).

[Aik14] K. Aikawa, A. Frisch, M. Mark, S. Baier, R. Grimm, et al., *Reaching Fermi Degeneracy via Universal Dipolar Scattering*, Phys. Rev. Lett. **112**, 010404 (2014).

[Alt07] A. Altmeyer, S. Riedl, C. Kohstall, M. J. Wright, R. Geursen, et al., *Precision Measurements of Collective Oscillations in the BEC-BCS Crossover*, Phys. Rev. Lett. **98**, 040401 (2007).

[Alt21] E. Altman, K. R. Brown, G. Carleo, L. D. Carr, E. Demler, et al., *Quantum Simulators: Architectures and Opportunities*, PRX Quantum **2**, 017003 (2021).

[And95] M. H. Anderson, J. R. Ensher, M. R. Matthews, C. E. Wieman, and E. A. Cornell, *Observation of Bose-Einstein Condensation in a Dilute Atomic Vapor*, Science **269** https://www.science.org/doi/pdf/10.1126/science.269.5221.198 (1995).

[Ash86] A. Ashkin, J. M. Dziedzic, J. E. Bjorkholm, and S. Chu, *Observation of a single-beam gradient force optical trap for dielectric particles*, Opt. Lett. **11**, 288–290 (1986).

[Bai12] S. Baier, *An optical dipole trap for Erbium with tunable geometry*, Master Thesis (2012).

[Bai16] S. Baier, M. J. Mark, D. Petter, K. Aikawa, L. Chomaz, et al., *Extended Bose-Hubbard models with ultracold magnetic atoms*, Science **352** https://www.science.org/doi/pdf/10.1126/science.aac9812 (2016).

[Ban05] H. Y. Ban, M. Jacka, J. L. Hanssen, J. Reader, and J. J. McClelland, *Laser cooling transitions in atomic erbium*, Opt. Express **13**, 3185–3195 (2005).

[Bar16] D. Barredo, S. de Léséleuc, V. Lienhard, T. Lahaye, and A. Browaeys, *An atom-by-atom assembler of defect-free arbitrary two-dimensional atomic arrays*, Science **354** https://www.science.org/doi/pdf/10.1126/science.aah3778 (2016).

[Bau15] T. Bauer, P. Banzer, E. Karimi, S. Orlov, A. Rubano, et al., *Observation of optical polarization Möbius strips*, Science **347** https://www.science.org/doi/pdf/10.1126/science.1260635 (2015).

[Bau17] T. Bauer, *Probe-based nano-interferometric reconstruction of tightly focused vectorial light fields*, PhD Thesis (2017).

[Bec18] J. H. Becher, S. Baier, K. Aikawa, M. Lepers, J.-F. Wyart, et al., *Anisotropic polarizability of erbium atoms*, Phys. Rev. A **97**, 012509 (2018).

[Bel09] K. Beloy, *Theory of the ac Stark Effect on the Atomic Hyperfine Structure and Applications to Microwave Atomic Clocks*, PhD Thesis (2009).

[Ber08] A. J. Berglund, J. L. Hanssen, and J. J. McClelland, *Narrow-Line Magneto-Optical Cooling and Trapping of Strongly Magnetic Atoms*, Phys. Rev. Lett. **100**, 113002 (2008).

[Bos24] S. N. Bose, *Plancks Gesetz und Lichtquantenhypothese*, Zeitschrift für Physik **26**, 178–181 (1924).

[Bur16] N. Q. Burdick, Y. Tang, and B. L. Lev, *Long-Lived Spin-Orbit-Coupled Degenerate Dipolar Fermi Gas*, Phys. Rev. X **6**, 031022 (2016).

[Car15] F. Cardano, *Engineering spin and orbital angular momentum interactions in a light beam: quantum and classical applications*, PhD Thesis (2015).

[Chi10] C. Chin, R. Grimm, P. Julienne, and E. Tiesinga, *Feshbach resonances in ultracold gases*, Rev. Mod. Phys. **82**, 1225–1286 (2010).

[Cho16] L. Chomaz, S. Baier, D. Petter, M. J. Mark, F. Wächtler, et al., *Quantum-Fluctuation-Driven Crossover from a Dilute Bose-Einstein Condensate to a Macrodroplet in a Dipolar Quantum Fluid*, Phys. Rev. X **6**, 041039 (2016).

[Cho22] L. Chomaz, I. Ferrier-Barbut, F. Ferlaino, B. Laburthe-Tolra, B. L. Lev, et al., *Dipolar physics: a review of experiments with magnetic quantum gases*, Reports on Progress in Physics **86**, 026401 (2022).

[Cla24] F. Claude, L. Lafforgue, J. J. A. Houwman, M. J. Mark, and F. Ferlaino, *Optical Manipulation of Spin States in Ultracold Magnetic Atoms via an Inner-Shell Hz Transition*.

[Coo18] A. Cooper, J. P. Covey, I. S. Madjarov, S. G. Porsev, M. S. Safronova, et al., *Alkaline-Earth Atoms in Optical Tweezers*, Phys. Rev. X **8**, 041055 (2018).

[Dal22] A. J. Daley, I. Bloch, C. Kokail, S. Flannigan, N. Pearson, et al., *Practical quantum advantage in quantum simulation*, Nature **607**, 667–676 (2022).

[Dav95] K. B. Davis, M. O. Mewes, M. R. Andrews, N. J. van Druten, D. S. Durfee, et al., *Bose-Einstein Condensation in a Gas of Sodium Atoms*, Phys. Rev. Lett. **75**, 3969–3973 (1995).

[DB24] L. De Broglie, *Recherches sur la théorie des quanta*, PhD thesis (1924).

[DeM99] B. DeMarco and D. S. Jin, *Onset of Fermi Degeneracy in a Trapped Atomic Gas*, Science **285** https://www.science.org/doi/pdf/10.1126/science.285.5434.1703 (1999).

[Dor03] R. Dorn, S. Quabis, and G. Leuchs, *Sharper Focus for a Radially Polarized Light Beam*, Phys. Rev. Lett. **91**, 233901 (2003).

[Du24] L. Du, P. Barral, M. Cantara, J. de Hond, Y.-K. Lu, et al., *Atomic physics on a 50-nm scale: Realization of a bilayer system of dipolar atoms*, Science **384** https://www.science.org/doi/pdf/10.1126/science.adh3023 (2024).

[Ein05] A. Einstein, *Quantentheorie des einatomigen idealen Gases*, pp. 237–244, John Wiley Sons, Ltd, 2005.

[Faz19] S. Fazzini, L. Barbiero, and A. Montorsi, *Interaction-Induced Fractionalization and Topological Superconductivity in the Polar Molecules Anisotropic $t - J$ Model*, Phys. Rev. Lett. **122**, 106402 (2019).

[Fey82] R. P. Feynman, *Simulating physics with computers*, International Journal of Theoretical Physics **21**, 467–488 (1982).

[For21] A. Forbes, M. de Oliveira, and M. R. Dennis, *Structured light*, Nature Photonics **15**, 253–262 (2021).

[Fri14] A. Frisch, *Dipolar Quantum Gases of Erbium*, PhD Thesis (2014).

[Gad09] B. Gadway, D. Pertot, R. Reimann, M. G. Cohen, and D. Schneble, *Analysis of Kapitza-Dirac diffraction patterns beyond the Raman-Nath regime*, Opt. Express **17**, 19173–19180 (2009).

[Gau16] G. Gauthier, I. Lenton, N. M. Parry, M. Baker, M. J. Davis, et al., *Direct imaging of a digital-micromirror device for configurable microscopic optical potentials*, Optica **3**, 1136–1143 (2016).

[GM20] P. García-Martínez, D. Marco, J. L. Martínez-Fuentes, M. del Mar Sánchez-López, and I. Moreno, *Efficient on-axis SLM engineering of optical vector modes*, Optics and Lasers in Engineering **125**, 105859 (2020).

[Gre02] M. Greiner, O. Mandel, T. Esslinger, T. W. Hänsch, and I. Bloch, *Quantum phase transition from a superfluid to a Mott insulator in a gas of ultracold atoms*, Nature **415**, 39–44 (2002).

[Gri00] R. Grimm, M. Weidemüller, and Y. B. Ovchinnikov, *Optical Dipole Traps for Neutral Atoms*, Advances In Atomic, Molecular, and Optical Physics, vol. 42, Academic Press, 2000, pp. 95–170.

[Hen23] J. Hennebichler, *Towards the creation of a two-dimensional optical tweezer array using a liquid crystal spatial light modulator*, Master Thesis (2023).

[Jac20] G. Jacquemet, A. F. Carisey, H. Hamidi, R. Henriques, and C. Leterrier, *The cell biologist's guide to super-resolution microscopy*, Journal of Cell Science **133** https://journals.biologists.com/jcs/article-pdf/133/11/jcs240713/3509892/jcs240713.pdf (2020).

[Jak98] D. Jaksch, C. Bruder, J. I. Cirac, C. W. Gardiner, and P. Zoller, *Cold Bosonic Atoms in Optical Lattices*, Phys. Rev. Lett. **81**, 3108–3111 (1998).

[Jak05] D. Jaksch and P. Zoller, *The cold atom Hubbard toolbox*, Annals of Physics **315**, 52–79 (2005), Special Issue.

[Kie12] F. L. Kien, P. Schneeweiss, and A. Rauschenbeutel, *Dynamical polarizability of atoms in arbitrary light fields: general theory and application to cesium*, The European Physical Journal D **67**, 1–16 (2012).

[Koh07] C. Kohstall, *A New Toolbox for Experiments with ultracold Li-6*, Diploma Thesis (2007).

[Kra23] A. Kramida, Yu. Ralchenko, J. Reader, and and NIST ASD Team, NIST Atomic Spectra Database (ver. 5.11), [Online]. Available: `https://physics.nist.gov/asd` [2024, October 14]. National Institute of

Standards and Technology, Gaithersburg, MD.,
Note: To get the energy levels of erbum, select "Levels", then enter "Er I".

[Lac12] C. Lacroute, K. S. Choi, A. Goban, D. J. Alton, D. Ding, et al., *A state-insensitive, compensated nanofiber trap*, New Journal of Physics **14**, 023056 (2012).

[Laf22] L. Lafforgue, *Study of a dipolar gas confined in a one-dimensional lattice and construction of a new imaging setup for the ERBIUM experiment*, Master's Thesis (2022).

[Lep14] M. Lepers, J.-F. Wyart, and O. Dulieu, *Anisotropic optical trapping of ultracold erbium atoms*, Phys. Rev. A **89**, 022505 (2014).

[Li17] H. Li, J.-F. Wyart, O. Dulieu, and M. Lepers, *Anisotropic optical trapping as a manifestation of the complex electronic structure of ultracold lanthanide atoms: The example of holmium*, Phys. Rev. A **95**, 062508 (2017).

[Liu18] S. Liu, Q. Shuxia, Y. Zhang, L. Peng, D. Wu, et al., *Highly efficient generation of arbitrary vector beams with tunable polarization, phase, and amplitude*, Photonics Research **6**, 228 (2018).

[Liu22a] M. Liu, Y. Lei, L. Yu, X. Fang, Y. Ma, et al., *Super-resolution optical microscopy using cylindrical vector beams*, Nanophotonics **11**, 3395–3420 (2022).

[Liu22b] S. Liu, P. Hoess, and J. Ries, *Super-Resolution Microscopy for Structural Cell Biology*, Annual Review of Biophysics **51**, 301–326 (2022).

[Lu11] M. Lu, N. Q. Burdick, S. H. Youn, and B. L. Lev, *Strongly Dipolar Bose-Einstein Condensate of Dysprosium*, Phys. Rev. Lett. **107**, 190401 (2011).

[Mai11] M. Maik, P. Buonsante, A. Vezzani, and J. Zakrzewski, *Dipolar bosons on an optical lattice ring*, Phys. Rev. A **84**, 053615 (2011).

[Mau07] C. Maurer, A. Jesacher, S. Fürhapter, S. Bernet, and M. Ritsch-Marte, *Tailoring of arbitrary optical vector beams*, New Journal of Physics **9**, 78 (2007).

[Max65] J. C. Maxwell, *A Dynamical Theory of the Electromagnetic Field*, Philosophical Transactions of the Royal Society of London **155**, 459–512 (1865).

[McD19] M. McDonald, J. Trisnadi, K.-X. Yao, and C. Chin, *Superresolution Microscopy of Cold Atoms in an Optical Lattice*, Phys. Rev. X **9**, 021001 (2019).

[Mit14] R. Mitsch, C. Sayrin, B. Albrecht, P. Schneeweiss, and A. Rauschenbeutel, *Quantum state-controlled directional spontaneous emission of photons into a nanophotonic waveguide*, Nature Communications **5**, 5713 (2014).

[Nat19] G. Natale, R. M. W. van Bijnen, A. Patscheider, D. Petter, M. J. Mark, et al., *Excitation Spectrum of a Trapped Dipolar Supersolid and Its Experimental Evidence*, Phys. Rev. Lett. **123**, 050402 (2019).

[Nor18] M. A. Norcia, A. W. Young, and A. M. Kaufman, *Microscopic Control and Detection of Ultracold Strontium in Optical-Tweezer Arrays*, Phys. Rev. X **8**, 041054 (2018).

[Nor21] M. A. Norcia and F. Ferlaino, *Developments in atomic control using ultracold magnetic lanthanides*, Nature Physics **17**, 1349 – 1357 (2021).

[Nov12] L. Novotny and B. Hecht, *Propagation and focusing of optical fields*, Principles of Nano-Optics, Cambridge University Press, Cambridge, 2012, pp. 45–85.

[Ols13] A. J. Olson, R. J. Niffenegger, and Y. P. Chen, *Optimizing the efficiency of evaporative cooling in optical dipole traps*, Phys. Rev. A **87**, 053613 (2013).

[Ott18] E. Otte, K. Tekce, and C. Denz, *Spatial multiplexing for tailored fully-structured light*, Journal of Optics **20**, 105606 (2018).

[Pas10] B. Pasquiou, G. Bismut, Q. Beaufils, A. Crubellier, E. Maréchal, et al., *Control of dipolar relaxation in external fields*, Phys. Rev. A **81**, 042716 (2010).

[Pat20] A. Patscheider, B. Zhu, L. Chomaz, D. Petter, S. Baier, et al., *Controlling dipolar exchange interactions in a dense three-dimensional array of large-spin fermions*, Phys. Rev. Res. **2**, 023050 (2020).

[Phe19] G. A. Phelps, *A dipolar quantum gas microscope*, PhD Thesis (2019).

[Phe20] G. A. Phelps, A. Hébert, A. Krahn, S. Dickerson, F. Öztürk, et al., *Sub-second production of a quantum degenerate gas*.

[Pit16] L. Pitaevskii and S. Stringari, *Bose-Einstein Condensation and Superfluidity*, Oxford University Press, 01 2016.

[Pla01] M. Planck, *Ueber das Gesetz der Energieverteilung im Normalspectrum*, Annalen der Physik **309**, 553–563 (1901).

[Pol17] C. Politi, *Optical dipole trap for an erbium and dysprosium mixture*, Master Thesis (2017).

[RG17] C. Rosales-Guzmán, N. Bhebhe, and A. Forbes, *Simultaneous generation of multiple vector beams on a single SLM*, Opt. Express **25**, 25697–25706 (2017).

[RG20] C. Rosales-Guzmán, X.-B. Hu, A. Selyem, P. Moreno-Acosta, S. Franke-Arnold, et al., *Polarisation-insensitive generation of complex vector modes from a digital micromirror device*, Scientific Reports **10**, 10434 (2020).

[Ric59] B. Richards and E. Wolf, *Electromagnetic Diffraction in Optical Systems. II. Structure of the Image Field in an Aplanatic System*, Proceedings of the Royal Society of London Series A **253**, 358–379 (1959).

[Rie12] A. Rietzler, *Narrow-Line Cooling Light for a Magneto-Optical Trap of Erbium Atoms*, Master Thesis (2012).

[Rub19] A. Rubano, F. Cardano, B. Piccirillo, and L. Marrucci, *Q-plate technology: a progress review (Invited)*, J. Opt. Soc. Am. B **36**, D70–D87 (2019).

[Sal91] B. Saleh and M. Teich, *Fundamentals of Photonics*, John Wiley Sons, Ltd, 1991.

[Su23] L. Su, A. Douglas, M. Szurek, R. Groth, S. F. Ozturk, et al., *Dipolar quantum solids emerging in a Hubbard quantum simulator*, Nature **622**, 724–729 (2023).

[Sub19] S. Subhankar, Y. Wang, T.-C. Tsui, S. L. Rolston, and J. V. Porto, *Nanoscale Atomic Density Microscopy*, Phys. Rev. X **9**, 021002 (2019).

[Tho13] J. D. Thompson, T. G. Tiecke, A. S. Zibrov, V. Vuletic, and M. D. Lukin, *Coherence and Raman Sideband Cooling of a Single Atom in an Optical Tweezer*, Phys. Rev. Lett. **110**, 133001 (2013).

[Val16] G. Vallone, A. Sponselli, V. D'Ambrosio, L. Marrucci, F. Sciarrino, et al., *Birth and evolution of an optical vortex*, Opt. Express **24**, 16390–16395 (2016).

[vB10] R. M. W. van Bijnen, N. G. Parker, S. J. J. M. F. Kokkelmans, A. M. Martin, and D. H. J. O'Dell, *Collective excitation frequencies and stationary states of trapped dipolar Bose-Einstein condensates in the Thomas-Fermi regime*, Phys. Rev. A **82**, 033612 (2010).

[Wei98] M. Weitz, S. Friebel, R. Scheunemann, J. Walz, and T. W. Hänsch, *A CO2 laser optical lattice with cold rubidium atoms*, International Quantum Electronics Conference, Optica Publishing Group, 1998, p. QFA6.

[Yan20] H. Yang and D. P. Chu, *Phase flicker in liquid crystal on silicon devices*, Journal of Physics: Photonics **2**, 032001 (2020).

[Yan23] Y. Yang, A. Forbes, and L. Cao, *A review of liquid crystal spatial light modulators: devices and applications*, Opto-Electronic Science **2**, 230026 (2023).

[You00] K. S. Youngworth and T. G. Brown, *Focusing of high numerical aperture cylindrical-vector beams*, Opt. Express **7**, 77–87 (2000).

[Zha02] Q. Zhan and J. R. Leger, *Focus shaping using cylindrical vector beams*, Opt. Express **10**, 324–331 (2002).

[Zha09] Q. Zhan, *Cylindrical vector beams: from mathematical concepts to applications*, Adv. Opt. Photon. **1**, 1–57 (2009).

[Zub16] M. S. Zubairy, *A Very Brief History of Light*, pp. 3–24, Springer International Publishing, Cham, 2016.

Acknowledgements

First, I would like to thank my supervisor Francesca Ferlaino, for giving me the opportunity to work in the ERBIUM lab. I am grateful for her support throughout my master's project and her advice during the writing of this thesis. I would also like to thank Manfred J. Mark, for valuable discussions and support when writing this thesis.

A big thank you goes to our administrative team, Silvia Bonazza and Hai-My Gian, who dealt with all my orders and were always providing me answers to administrative questions.

I also want to thank Filippo Cardano, Professor at the University of Naples, for welcoming me and Johanna in his lab via the Aurora program. During those two weeks, Filippo and his PhD student, Maria Gorizia Ammendola, generously dedicated a lot of time to explaining and demonstrating the fabrication and working principle of q-plates.

I would also like to express my gratitude to all the members of the ERBIUM team who were present during my time as a master's student: Ferdinand, Louis, and Arfor. In particular, I want to thank Ferdinand for encouraging discussions about the q-plates. Thanks to Ferdinand and Arfor for working together with me to align the scanning ODT and to Louis for helping me with the electronics. I am grateful to all the members of the ERBIUM team for always taking the time to explain the ongoing projects in the lab. I also want to thank the entire group for insightful discussions on physics and other topics, especially making lunch time a great time.

I also want to thank my friends: My friend and study group during the Bachelor - Lea, Berni, Jakob and Leon - I don't think I would have managed the Bachelor without you. I want to thank Johanna, Beat, Linus, Berni and Lea for completing some of the Master courses together. I am truly grateful to have Maxi, Luise, Ramona, Jana, Lea, Berni, Alina and Lea from Aibling as my friends. I want to thank you all for the many experiences we share, whether it's road bike adventures, hikes around Innsbruck or cooking evenings with long conversations on the menu.

Most importantly, I want to thank my family for making my studies possible and always being there for me. My mum has shown me the importance of living an active and independent life, and is always available for a phone call - unless, of course, she is busy climbing. My dad, a physics teacher and always eager to discuss math and physics questions, was a great inspiration for me to study physics.

universität
innsbruck

Eidesstattliche Erklärung

Ich erkläre hiermit an Eides statt durch meine eigenhändige Unterschrift, dass ich die vorliegende Arbeit selbständig verfasst und keine anderen als die angegebenen Quellen und Hilfsmittel verwendet habe. Alle Stellen, die wörtlich oder inhaltlich den angegebenen Quellen entnommen wurden, sind als solche kenntlich gemacht.

Die vorliegende Arbeit wurde bisher in gleicher oder ähnlicher Form noch nicht als Magister-/Master-/Diplomarbeit/Dissertation eingereicht.

Datum	Unterschrift